VERIFICATION OF UNIVERSAL SURFACE SCALING BEHAVIOR IN CRITICAL BINARY LIQUID MIXTURES WITH NEUTRON AND X-RAY REFLECTOMETRY

by

MATTHEW D BROWN

B.S., Brigham Young University, 1994

AN ABSTRACT OF A DISSERTATION

submitted in partial fulfillment of the
requirements for the degree

DOCTOR OF PHILOSOPHY

Department of Physics
College of Arts and Sciences

KANSAS STATE UNIVERSITY
Manhattan, Kansas
2007

Abstract

We have studied two critical binary liquid mixtures in the mixed phase regime with x-ray and neutron reflectometry to verify universal critical scaling at a non-critical interface. We compared our results with previous results obtained with ellipsometry.

At a solid-liquid or liquid-vapor interface of an AB binary liquid mixture the component with the lower surface tension will dominate that interface. If the surface tension differential $\Delta\sigma \equiv \sigma_b - \sigma_a$ between the components of the mixture is large enough the composition of the surface layer will loose its dependence on $\Delta\sigma$. This case is referred to as strong adsorption.

We study the case of strong adsorption for a binary liquid mixture at the critical composition with respect to the demixing phase transition. Sufficiently close to the critical temperature T_c the influence of bulk critical behavior is expected to dominate the way the surface adsorption layer decays with depth z from the surface composition to the bulk composition. The length scale of the decay profile is expected to be proportional to the composition correlation length ξ, and is expected to scale with a universal composition scaling function $P_{\pm}(z/\xi)$.

In a neutron reflectometry study of a critical mixture of D_2O and 3-methylpyridine against a quartz substrate we verify universal critical scaling using a scaling function previously used to describe ellipsometry data. In an x-ray reflectometry study of the liquid-vapor interface of a critical mixture of n-dodecane and 1,1,2,2 tetrabromoethane, which had previously been studied with ellipsometry, we find that we are able to describe all data by using the same scaling function provided that we account for non-critical, system dependent surface structure as well. We are also able to simulate ellipsometry with our mathematical profile model and compare the simulation to the previous ellipsometry data.

VERIFICATION OF UNIVERSAL SURFACE SCALING BEHAVIOR IN CRITICAL BINARY LIQUID MIXTURES WITH NEUTRON AND X-RAY REFLECTOMETRY

by

MATTHEW D BROWN

B.S., Brigham Young University, 1994

A DISSERTATION

submitted in partial fulfillment of the
requirements for the degree

DOCTOR OF PHILOSOPHY

Department of Physics
College of Arts and Sciences

KANSAS STATE UNIVERSITY
Manhattan, Kansas
2007

Approved by:

Major Professor
Bruce M. Law

Copyright

Matthew D Brown

2007

Abstract

We have studied two critical binary liquid mixtures in the mixed phase regime with x-ray and neutron reflectometry to verify universal critical scaling at a non-critical interface. We compared our results with previous results obtained with ellipsometry.

At a solid-liquid or liquid-vapor interface of an AB binary liquid mixture the component with the lower surface tension will dominate that interface. If the surface tension differential $\Delta\sigma \equiv \sigma_b - \sigma_a$ between the components of the mixture is large enough the composition of the surface layer will loose its dependence on $\Delta\sigma$. This case is referred to as strong adsorption.

We study the case of strong adsorption for a binary liquid mixture at the critical composition with respect to the demixing phase transition. Sufficiently close to the critical temperature T_c the influence of bulk critical behavior is expected to dominate the way the surface adsorption layer decays with depth z from the surface composition to the bulk composition. The length scale of the decay profile is expected to be proportional to the composition correlation length ξ, and is expected to scale with a universal composition scaling function $P_{\pm}(z/\xi)$.

In a neutron reflectometry study of a critical mixture of D_2O and 3-methylpyridine against a quartz substrate we verify universal critical scaling using a scaling function previously used to describe ellipsometry data. In an x-ray reflectometry study of the liquid-vapor interface of a critical mixture of n-dodecane and 1,1,2,2 tetrabromoethane, which had previously been studied with ellipsometry, we find that we are able to describe all data by using the same scaling function provided that we account for non-critical, system dependent surface structure as well. We are also able to simulate ellipsometry with our mathematical profile model and compare the simulation to the previous ellipsometry data.

Table of Contents

Table of Contents viii

List of Figures x

List of Tables xi

Acknowledgements xii

Dedication xiii

Preface xiv

1 Introduction 1
- 1.1 Phase transitions and preferential adsorption near a critical point 2
- 1.2 Overview of Chapters 9

2 Experimental Techniques 12
- 2.1 X-ray and Neutron Reflectometry 12
  - 2.1.1 Reflectometry basics 13
  - 2.1.2 Solving Maxwell's equations 17
  - 2.1.3 Software model of reflectometry 24
  - 2.1.4 Including surface roughness 30
  - 2.1.5 Resolution 33
- 2.2 Ellipsometry 39

3 Ultra-stable oven designed for x-ray reflectometry and ellipsometry studies of liquid surfaces 47
- 3.1 Introduction 47
- 3.2 Construction Details. 50
- 3.3 Results and discussion 54

4 X-ray Specular Reflectivity Study of a Critical Binary Fluid Mixture 63
- 4.1 Reflectivity Experiment 66
- 4.2 Summary of Results 69

5 Comparison of critical adsorption scaling functions obtained from neutron reflectometry and ellipsometry 79
- 5.1 Introduction 79

5.2 Survey of prior work 82
5.3 Experimental Methods 87
5.4 Analysis 92
5.5 Summary 96
5.6 Acknowledgements 98

6 X-ray and ellipsometric study of strong critical adsorption 104
6.1 Introduction 104
6.2 Theory 105
6.3 P1 Model 107
6.4 Experimental Methods 109
6.5 Analysis 110
6.5.1 Ellipsometry 111
6.5.2 X-ray Reflectometry 112
6.5.3 Determination of $\phi(z)$ 113
6.6 Conclusion 119
6.7 Acknowledgements 120

7 Conclusion 123

List of Figures

1.1 Phase diagram for the demixing phase transition. 3
1.2 Liquid mixture in mixed and demixed states 4
1.3 Order parameter as a function of free energy. 6
1.4 Depiction of preferential adsorption. 8

2.1 Reflection and refraction from a simple interface. 14
2.2 Reflection from a multilayered interface. 19
2.3 Continuous medium 20
2.4 Rough interface between two media. 31

3.1 X-ray environment disassembled 51
3.2 X-ray environment assembled 52
3.3 Sample cell disassembled 55
3.4 Thermister circuit 56
3.5 Thermal stability data 59
3.6 Experimental data from ultra-stable oven 60

4.1 X-ray reflectivity curves at various temperatures 72
4.2 Ellipsometry simulation on inverted profile. 73
4.3 Inverted volume fraction profiles 74
4.4 Comparison of scaled inverted profiles with various models. 75
4.5 Comparison of scaled inverted profiles with mean field theory. 76

5.1 Comparison of contrast in reflectivity curves 99
5.2 Neutron reflectivity fits for D_2O + beta picoline at various temperatures . . 100

6.1 Model profiles for x-ray data 117
6.2 Fits to x-ray reflectometry data 118
6.3 Comparison of simulated and actual ellipsometry data 120

List of Tables

5.1 Critical adsorption parameters 86
5.2 Critical adsorption scaling function models 86
5.3 Scattering length densities at 25 ^0C 94
5.4 Fitting parameters 97

6.1 Critical adsorption P1 scaling function 108
6.2 X-ray and optical parameters for the DT critical mixture 109
6.3 Fitting parameters for x-ray data 114

Acknowledgments

I would like to thank all who have helped me both in conducting this research, as well as those without whose support the work would not have been completed. Firstly, I thank Professor Bruce M. Law for his ideas, advice, and support in this work, as well as the time he has spent traveling and working with me in locations all over the United States. Likewise, I thank Dr. Serif Uran who also traveled with us. I thank our collaborators, Dr. Laurence Lurio, Dr. Bill Hamilton, and Lyle Marschand, without whose help this work would not have succeeded. In our travels we have also had the opportunity to work with beam line scientists too numerous to mention, but a special thanks is due to Dr. Sushil Satija, Dr. Ivan Kuzmenko, Dr. Thomas Gog, Dr. Jarek Majewski, and Eric Watkins. My colleague Dr. Jae Hie Cho, while not directly involved in this work, has helped in many ways. I also thank Dr. Ashis Mukhopadhyay for his help. In addition to Dr. Law, I also thank my other committee members, Dr. Shie-Shien Yang, Dr. Chris Sorensen, Dr. Amit Chakrabarti, Dr. Daniel Higgins, and Dr. Mick O'shea for their time and effort. I am grateful for the Kansas State Physics Department for allowing me an opportunity to do this research, and am particularly appreciative of the machinists without whose help this work could not have been done, with special thanks to Bob Geering, Dave Hill, and Ron Jackson. Jim Hodgson, the glass blower for the Chemistry department, was also instrumental in our success. I thank my parents for their financial support, and most importantly my wife Linda, who has born many burdens to make this work doable.

Dedication

I dedicate this work to my wife Linda, and children Matthew Paul, Kaylana Cassidie, and Anastasia Noel. Proving to my children that dreams should be pursued has made this work worth doing.

Preface

This work is a compilation of the results of my research on critical adsorption in binary liquid mixtures. The bulk of the dissertation includes papers that have been published, accepted for publication, or submitted for publication. these include chapters 3 through 6. The chapter titles are the same as the titles under which the papers were published. Some changes have been made to these papers to fit the format appropriate for a dissertation. Bibliographies have been done on a chapter by chapter basis in order to keep chapters that have been published elsewhere in as close a form as possible to the published form, and because in the author's experience a chapter by chapter bibliography is easier to use.

Chapter 3 was published in M. Brown, S. Uran, B. Law, L. Marschand, L. Lurio, I. Kuzmenko and T. Gog, Review of Scientific Instruments **75**, 2536 (2004). Chapter 4 was published in L. W. Marschand, M. Brown, L. B. Lurio, B. M. Law, S. Uran, I. Kuzmenko and T. Gog, Physical Review E **72**, 011509 (2005). Chapter 5 has been accepted for publication by Journal of Chemichal Physics. Chapter 6 has been submitted for publication to Physical Review E.

Chapter 1

Introduction

This dissertation is a study of the impact of bulk critical phenomena on adsorption at a critical liquid-vapor or solid-liquid interface of a critical binary liquid mixture. The focus is on the special case of strong adsorption, wherein the difference in surface tension between the two components of the mixture, $\Delta\sigma \equiv \sigma_b - \sigma_a$, is sufficiently large that the adsorption profile of the surface layer looses dependence on the magnitude of $\Delta\sigma$. We build upon previous research discussed in Carpenter et al.[1] and references therein in which ellipsometry was used to study interfaces of various critical binary liquid mixtures. We do this by studying similar systems with neutron and x-ray reflectometry, and seeking agreement or compatibility between our results and those obtained with ellipsometry.

In 1978 Fisher and de Gennes[2] proposed a theory for adsorption at a non-critical interface of a critical system sufficiently close to the critical temperature T_c. They predicted that the adsorption profile should scale with reduced temperature, defined as $t \equiv |T - T_c|/T_c$, in a way independent of the specific system. They also discussed limiting behavior both near to and far from the interface. Prior to the research presented herein much progress had been made in both verifying these predictions, and in finding a scaling model that consistently described behavior of such systems when studied with ellipsometry. Chapter 5 contains an extensive overview of this previous work, and references to that previous work. However, this work could not be considered conclusive in the absence of verification with other techniques, and there are limits to the temperature range over which ellipsometry is sufficiently effective

in studying these systems.

In this chapter we first overview strong adsorption near a critical point for the demixing phase transition. We do so beginning from a somewhat general description of critical phenomena in the presence of an ordering field, then focus on the special case of strong critical adsorption for binary liquid mixtures. We then overview the contents of the following chapters.

1.1 Phase transitions and preferential adsorption near a critical point

Preferential adsorption of a component of lower surface tension is a general phenomenon, of which critical adsorption is a very special case. However, in this introduction we shall develop our discussion in terms of critical phenomena to better elucidate the theoretical principles we are investigating.

Consider the phase diagram for a binary liquid mixture of components A and B in figure 1.1. The plot represents the temperature at which a binary liquid mixture of a given relative composition will undergo a demixing phase transition. Above the curve the mixture will exist in a single, mixed phase of uniform composition, other than local fluctuations. Below the curve two phases of different composition will coexist, the function for the coexistence curve allowing for two relative compositions at a given temperature. The mixed and demixed states are depicted in figure 1.2. As we first cross the curve decreasing in temperature from above at constant bulk composition v_1 one region of the mixture will follow the phase diagram continuously from v_1, at point of contact, while a region of a coexisting phase will arise with a composition of v_2 and follow the curve down from there. The volumes of the two phases must be such that the average composition remains at v_1. The jump from composition v_1 to composition v_2 for the second region is in general discontinuous, and this is therefore generally a discontinuous (first order) phase transition. However, if instead the bulk volume fraction is at v_c the bifurcation will occur at the critical temperature T_c, with

the composition of both regions transitioning continuously from v_c. Thus at (v_c , T_c) we have a continuous (second order) phase transition.

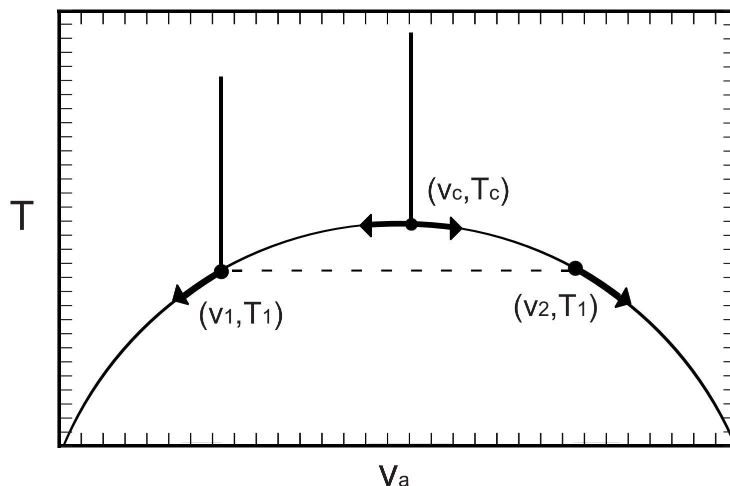

Figure 1.1: *Depiction of the demixing phase transition as a plot of phase separation temperature as a function of relative volume fraction of component a. Above the curve the mixture will remain in the mixed state. As one descends in temperature at a relative composition of v_1, upon crossing the phase separation curve at T_1, a second phase will appear at a relative volume fraction of v_2. Both phases will follow the phase diagram with decreasing T. Note however that as a mixture at composition v_c crosses the phase separation curve at T_c both phases will diverge continuously from v_c with decreasing temperature.*

The critical phase transition can be considered in terms of free energy. We will briefly describe this approach using Landau's phenomenological theory, loosely following the development by Pathria[3] . Though precise results prove incorrect for our system, this will give us a starting point which is qualitatively accurate. We describe a system near a critical phase transition in terms of free energy ψ as a function of reduced temperature and some long range order parameter m. The chosen order parameter must describe the coexisting phases of a system where relevant, and must be zero in a one phase state in the absence of some ordering field. In the case of a binary liquid mixture the difference between the relative volume fraction of one coexisting phase and the average composition is a suitable parameter, which must by definition be zero in the mixed state in the absence of an ordering field.

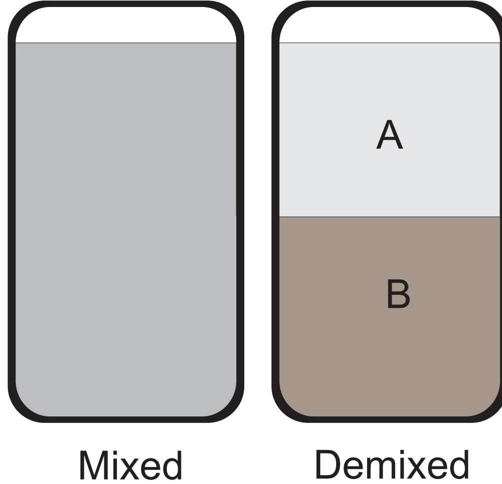

Figure 1.2: *Depiction of a binary liquid mixture in the mixed state (right), and the demixed state, where two phases coexist: one rich in component A, and the other rich in component B.*

Note that the phase diagram in figure 1.1 is symmetric. While this does not always hold far from criticality, empirically we do expect symmetry near the critical point. We thus describe our free energy as an even polynomial expansion in m, which we expect to be small near the critical point.

$$\psi(t, m) = q(t) + r(t)m^2 + s(t)m^4 + ... \tag{1.1}$$

The coefficients $q(t)$, $r(t)$, and $s(t)$ can likewise be expanded in powers of t. For reasons we will not discuss, the only non-zero terms we keep for these coefficients are q_0, r_1, and s_0. Figure 1.3 shows a schematic plot of the resulting free energy for a critical system as a function of m at various temperatures. For $T \geq T_c$ there is a single minimum at $m = 0$, which becomes very broad at T_c. Below T_c we have two local minima at

$$m \approx \pm[(r_1/2s_0)\,|t|]^{1/2}. \tag{1.2}$$

Therefore, at least near the critical point, we would expect then to be able to describe the phase diagram in figure 1.1 as a simple power law relation

$$m = v - v_c \approx \pm M_{-}t^{\beta}, \quad M_{-} \equiv \sqrt{r_1/\left(2s_0\right)}, \tag{1.3}$$

where β=1/2. We would also expect analogous relations for other critical phase transitions. Another example would be an Ising magnetic system modeled as a lattice of magnetic particles with allowed spin (magnetic) orientations of only two opposing directions, defined as up or down. In this case the order parameter is defined as the system wide average spin orientation, $m_N \equiv (N_+ - N_-)/N$. The phase transition in this case is between a regime in which $m_N = 0$ in the absence of an external magnetic field, and the regime below the phase transition curve wherein $m_N \neq 0$. The second case is referred to as spontaneous magnetization. These regions are analogous to the mixed and demixed regions of figure 1.1 respectively.

Equation 1.3 turns out to be correct, except that β is not in general, and not in either system described here, given by β=1/2. However, β does turn out to be very close for both critical systems described here; $\beta \cong 0.328$[4] for binary mixtures, and $0.305 \leq \beta \leq 0.36$[5] for magnetic systems. Other thermodynamic properties can be described by similar power laws for both systems, again with analogous properties describable with exponents that are very close. Critical phase transitions can be grouped by the values of exponentials appropriate to describe analogous thermodynamic relationships near the critical point. Such groups of related phase transitions are called universality classes. A universality class may contain phase transitions for systems that seem completely unrelated in any other way. We shall make use of this by exploring scaling theory as it relates to an Ising magnetic system, and extrapolating this to scaling phenomena of a somewhat more complicated variety relevant to our system.

Rather than an order parameter which is uniform throughout a system, in real physical systems the value will fluctuate about the equilibrium value. From figure 1.3 we see that near T_c even a small energy fluctuation $K_B \Delta T$ will result in large fluctuations in the order parameter. Rather than considering the magnitude of an order parameter fluctuation, such as composition fluctuations in a binary mixture or density fluctuations in a pure fluid, a more measurable value is the average length scale over which such fluctuations occur, referred to

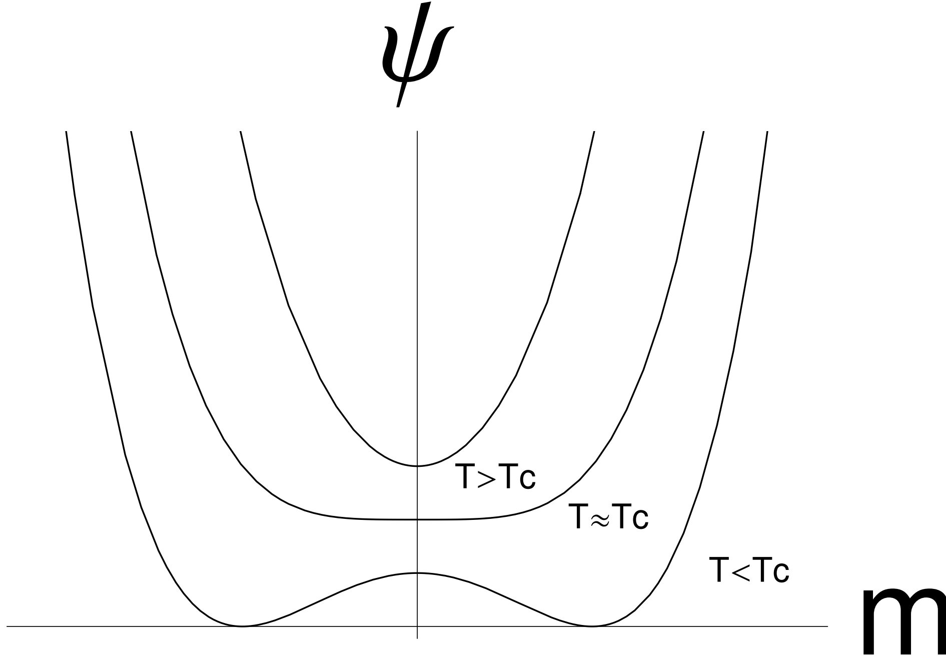

Figure 1.3: *Order parameter as a function of free energy for a critical system for various temperatures. Above the critical temperature there is a single minimum. Near the critical temperature the minimum becomes very broad, and small energy fluctuations result in large fluctuations in the order parameter. Below T_c there will be two minima, with the physical meaning that two phases can coexist.*

as the correlation length ξ. Sufficiently close to T_c one can derive from mean field theory the relation

$$\xi \sim t^{-\nu}, \tag{1.4}$$

where $\nu = 1/2$. Again power law behavior near T_c turns out to be valid, with the value of ν dependent on the universality class.

For an Ising magnetic system an external uniform magnetic field parallel (antiparallel) to the up spin direction will increase the proportion of up (down) spin particles. This can be represented in terms of the Landau phenomenological theory by including a term representing the external magnetic field as an ordering field:

$$\psi_h(t,m) \approx -\mathrm{hm} + q_0 + r_1 t m^2 + s_0 m^4 + ..., \tag{1.5}$$

where in this case h is due to the external magnetic field. By differentiating and setting the differential to zero we can find the equilibrium value of m in the presence of the ordering field h:

$$h(t,m) \approx 2r_1\mathrm{tm} + 4s_0m^3. \tag{1.6}$$

This can be rewritten grouping with m all terms from Equation 1.3 in anticipation of finding a result related to that equation.

$$h(t,m) \approx \frac{{r_1}^{3/2}}{{s_0}^{1/2}}|t|^{3/2}\left[2\,\mathrm{sign}(t)\left(\frac{{s_0}^{1/2}}{{r_1}^{1/2}}\frac{m}{|t|^{1/2}}\right) + 4\left(\frac{{s_0}^{1/2}}{{r_1}^{1/2}}\frac{m}{|t|^{1/2}}\right)^3\right]. \tag{1.7}$$

We are interested in our order parameter m as a function of h. While the precise solution is nasty, it suffices for our purposes to write

$$m(t,h) \approx \frac{{r_1}^{1/2}}{{s_0}^{1/2}}|t|^{1/2}F\left(\frac{{s_0}^{1/2}}{{r_1}^{3/2}}\frac{h}{|t|^{3/2}}\right). \tag{1.8}$$

The effect of the imposition of a uniform ordering field h, such as a magnetic field for an Ising magnetic system, is that we must multiply our zero field order parameter m(t,0) by a unitless function, which rather than being a function of h and t individually, scales with the ratio $h/|t|^{\Delta}$. $\Delta = 3/2$ here. The coefficient ${s_0}^{1/2}/{r_1}^{1/2}$ makes the argument a unitless parameter. Again the form of Equation 1.8 is born out in reality, except that in general $\Delta \neq 3/2$. It is another universal exponent with similar values for members of a given universality class.

The system which interests us is more complicated. Rather than a uniform ordering field, we are interested in the case where the ordering field is confined to a surface; in particular resulting from the differential in surface energies between the two components of our mixture. We call this a surface ordering field $h_1(\Delta\sigma)$. h_1 does have an implicit spatial dependence on distance from the surface z, being uniform over the entire surface, and zero everywhere else. Any scaling theory describing such a system must reflect this spatial dependence. The correlation length is the only available temperature dependent length scale which might scale with z. Fisher and de Gennes[2] suggest the relation

$$m_\pm(t,z,h_1) = m_\pm(t,z) \approx M_- t^\beta G(z/\xi_\pm, h_1/t^{\Delta_1}). \tag{1.9}$$

The subscript + (-) refers to the mixed (demixed) state.

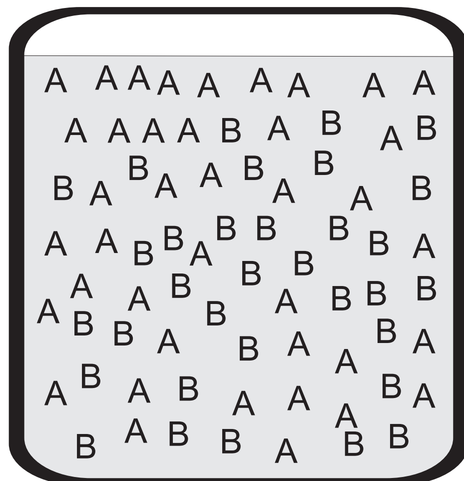

Figure 1.4: *Depiction of preferential adsorption in a binary liquid mixture. The component of a binary mixture of components A and B with the lower surface tension* σ *at an interface will dominate the adsorption layer. For a sufficiently large surface tension differential* $\Delta\sigma = \sigma_b - \sigma_a$ *one component may saturate the adsorption layer. Over a length scale governed by the composition correlation length* ξ *the composition will decay to the bulk composition.*

The effect of this ordering field is to increase the proportion of the component with the lower surface tension at or near the interface, as depicted in figure 1.4. Over some length scale from the surface governed by the correlation length ξ the composition will decay to the bulk composition.

Note that as the surface field in our case is confined to the surface, there is a limit to which strengthening h_1 can influence our system. Once h_1 is sufficiently large that the surface is saturated by the component of lower surface energy, increasing the magnitude of the surface ordering field can do no more. G looses its dependence on h_1, and we have a new scaling relation

$$m_{\pm}(t, z) \approx M_{-} t^{\beta} P_{\pm}(z/\xi_{\pm}). \tag{1.10}$$

Verifying the form of the universal composition scaling function $P_{\pm}(z/\xi_{\pm})$ is the focus of this work.

1.2 Overview of Chapters

The primary experimental techniques used in this study are x-ray and neutron reflectometry. This work builds on previous work involving ellipsometry, and we have collected data with ellipsometry primarily as a test of our sample environment, and have also analyzed ellipsometry results in light of a model developed in this work. Chapter 2 overviews the physics behind these experimental techniques and how software simulations of reflectometry can be used to test mathematical models with experimental data. Parts of the software algorithms used in simulating reflectometry are discussed in detail.

Chapters 3 and 4 have been published as papers, and are presented here with formats appropriate for this work. Chapters 5 and 6 are also pending publications as papers.

All data discussed in this work had to be collected under exacting thermal conditions. Very small thermal gradients, high thermal stability and precise temperature measurements were required. Additionally, we desired to verify the viability of our sample environment for x-ray reflectometry by comparing results for ellipsometry measurements taken in the environment with those taken by Cho et al. on the same type of mixture[6]. Chapter 3[7] discusses the sample environment and temperature control system designed for this purpose. The temperature control system used for the neutron reflectometry study was similar to that discussed in chapter 3.

Chapter 4[8] presents results from our x-ray reflectometry study of a critical mixture of dodecane + tetrabromoethane, as well as our first attempt to analyze the data. Initial attempts to model the data using the P1 model used successfully by Carpenter et al.[1] and Cho et al.[6] to describe ellipsometry results failed. Instead the reflectometry data was inverted directly to find profiles that were compatible with the data collected. These profiles failed to display universality, were incompatible with the P1 model, and did not provide a mathematical model that could be easily used to analyze ellipsometry data. However, the form of these profiles provided the inspiration for a modified P1 model that would later accomplish all three tasks. This analysis was an essential step in developing the model

presented later.

Chapter 5[9] presents results from a neutron reflectometry study of a critical mixture of deuterated water + beta picoline against a quartz substrate. The mixture was intentionally chosen to provide a low contrast between the bulk mixture and the substrate, while providing excellent contrast between the two components. This gave sufficient resolution of large length scales to enable us to probe critical adsorption nearer the critical temperature than has been done before with either neutron or x-ray reflectometry. Our results were highly consistent with the Carptenter P1 model. The only necessary modification to the P1 model was that we did not require complete saturation of the surface layer by one component. We discuss in the paper why we believe this may still be consistent with strong critical adsorption rather than with weak critical adsorption.

Chapter 6[10] revisits the x-ray data presented in chapter 4. The work discussed in chapter 5 convinced us of the need to allow for system dependent, non critical features at the interface. The profiles found in chapter 4 suggested layering against the interface. We tried a model wherein layering in a temperature independent way transitioned at a point at or very near a relative volume fraction of 0.7 dodecane to the Carpenter P1 model. Reflectometry simulations based on this model successfully described the neutron reflectometry data out to 5 degrees from T_c, and was reasonably compatible with ellipsometry data.

The conclusion outlines some reasonable deductions from this work, and suggests avenues of research opened by our results. The code used to simulate ellipsometry and both neutron and x-ray reflectometry are available on a CD, or can be downloaded from

http://www.mattbrownswebsite.com/professional/SimulationCode/EllipsometryCode.aspx

or

http://www.mattbrownswebsite.com/professional/SimulationCode/ReflectometryCode.aspx

.

Bibliography

[1] J. H. Carpenter, J. H. J. Cho & B. M. Law, Phys. Rev. E, **61**(1), 532 (2000).

[2] M. E. Fisher & P.-G. de Gennes, . C.R. Acad. Sci. Paris B, **287**, 207 (1978).

[3] R. K. Pathria, *Statistical Mechanics, pp. 305–358,* (Butterworth-Heinenmann, Woburn M.A., 1996).

[4] M. E. Fisher& J.-H. Chen, J. Phys. (Paris), **46** 1645(1985).

[5] K. E. Stierstadt, *Physics Data: Experimental Values of Critical Exponents and Amplitude Ratios of Magnetic Phase Transitions* (FachinformationZentrum, Karlsruhe, 1990)

[6] J. J. Cho, B. M. Law, & K. Grey, J. Chem. Phys., **116**, 3058 (2002).

[7] M. Brown, S. Uran, B. Law, L. Marschand, L. Lurio, I. Kuzmenko and T. Gog, Rev. Sci. Instr., **75**, 2536 (2004).

[8] L. W. Marschand et al., Phys. Rev. E, **72**, 011509. (2005)

[9] M. D Brown, B. M. Law, S. Satija, W. A. Hamilton, E. Watkins, J.-H. J. Cho and J. Majewski, *Comparison of critical adsorption scaling functions obtained from neutron reflectometry and ellipsometry.* J. Chem. Phys, accepted for publication.

[10] M. D. Brown, B. M. Law, L. Marschand, L. B. Lurio, I. Kuzmenko, T. Gog, and W. A. Hamilton, *Verification of Universality in critical adsorption with x-ray reflectometry and ellipsometry.* Phys. Rev. E., submitted for publication.

Chapter 2

Experimental Techniques

This chapter is a discussion of the experimental techniques used to collect data used in this work, and how such data can be analyzed by simulating measurements using these techniques on models of a system under study. The measurement techniques used are neutron and x-ray reflectometry, and birefringence modulated ellipsometry. The physics of the reflectometry techniques are similar enough that they are discussed in the same section. As the author was involved in all measurements using reflectometry techniques, and primarily analyzed ellipsometry data from an experiment done by others, we discuss the reflectometry in much greater detail, giving only an overview of ellipsometry. Portions of this chapter cover some very basic principles in order to broaden usefulness to those who may not have an expertise in physics or optics.

2.1 X-ray and Neutron Reflectometry

X-ray and neutron reflectometry are the primary techniques used in this work. Most of the following chapters will describe the results of experiments making use of these techniques, generally without discussing in depth either the physics behind reflectometry or how these techniques are simulated to compare reflectometry from a model profile to actual experimental data. A background is given here. We begin by defining a few optical terms with which some readers may not be familiar. We then discuss the refractive index for x-rays and neutrons in typical materials, and relate the refractive index of a material to its composition.

We use this to discuss the range over which reflectometry measurements are typically made. The bulk of this section then discusses how Maxwell's equations can be solved numerically to simulate a reflectometry measurement for a model interface, and how this is done computationally. We do this without much of a discussion of Maxwell's equations themselves. Finally we discuss how both surface roughness and the effects of finite resolution can be taken into account.

2.1.1 Reflectometry basics

In x-ray and neutron reflectometry the structure of surfaces can be probed by measuring the reflected intensity of impinging radiation as a function of angle θ or wavelength λ. As the physics of reflected radiation is well understood, one can use data from a reflectometry experiment to either test a possible model of the structure of a surface, or often to infer the structure of the surface directly. These experiments typically involve radiation with $\lambda \sim 0.1$nm, and are capable of resolutions normal to the surface under study ranging from an atomic length scale (~ 0.5nm) to 100 nm, making these techniques excellent surface probes. The area of the beam on the sample is macroscopic, however, and a measurement can be seen as indicating the average composition in an x-y plane as a function of depth.

In the following we will treat an x-ray beam as electromagnetic plane wave radiation. A neutron beam can be treated in much the same way. As not all readers will be familiar with electrodynamics or optics a brief review of relevant items will be given. For a wave propagating in some medium the group velocity c of that wave is given by

$$c = \lambda\nu, \tag{2.1}$$

where ν is the wave frequency, and λ is the wavelength of the wave. Defining angular frequency $\omega \equiv 2\pi\nu$, and wave number $k \equiv 2\pi/\lambda$, this can be rewritten as

$$c = \omega/k. \tag{2.2}$$

When the wave traveling in one medium impinges on another medium, as in figure 2.1, in general part of the wave will be transmitted, and part reflected. Clearly the frequency of

the wave can not change going from one medium to the other. Wavelength, however, can. This will result in a different phase velocity for the transmitted wave, and we get

$$\frac{c_i}{c_t} = \frac{\lambda_i}{\lambda_t} = \frac{k_t}{k_i}. \tag{2.3}$$

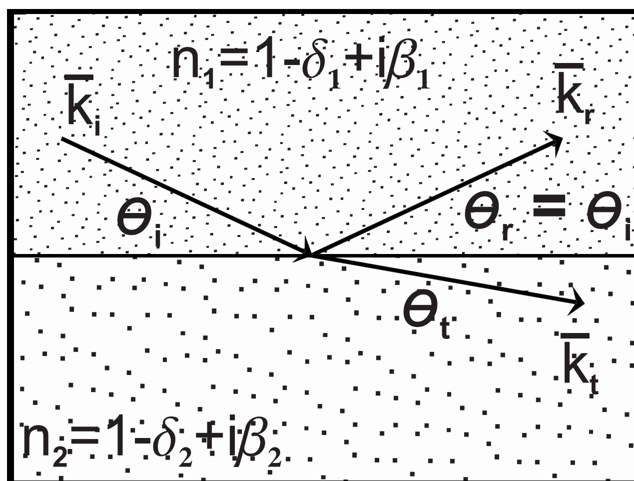

Figure 2.1: *Depiction of reflection and refraction of an electromagnetic plane wave at a simple, flat interface. The reflected angle, θ_r is equal to the incident angle, θ_i for specular reflection. The relationship between θ_i and the transmission angle θ_t is governed by Snell's law. In the case of small wavelengths for the incident radiation (such as x-rays), index of refraction is typically considered in the form shown in the diagram because it is generally very close to 1. Also, angles are measured from the interface. At visible wavelengths, such as those used for ellipsometry, angle is measured from the normal of the surface.*

We can express the direction in which a wave travels in terms of the wave number by making it a vector: $\vec{k} \equiv \frac{2\pi}{\lambda}\hat{k} = k\hat{k}$, where $\hat{k}$ is a unit vector in the direction of propagation.

For electromagnetic radiation we define k_0, λ, c as the wave number, wavelength, and speed of light in a vacuum. So for electromagnetic radiation propagating in some medium we can define an index of refraction as

$$k = \frac{2\pi n}{\lambda} = k_0 n, n \equiv \frac{v}{c}, \tag{2.4}$$

where v is the speed of light in the medium of propagation.

In order to understand reflectometry data we must understand the relationship between reflection and the compositions of both the medium in which the incident beam travels,

as well as the material from which the beam is reflected. Reflection occurs because of the difference of refractive indices of the two media. Because of the very short wavelength of the radiation used in these techniques materials have an index of refraction very close to 1. Therefore we generally write an index of refraction as:

$$n = 1 - \delta + \mathrm{i}\beta, \tag{2.5}$$

where $\delta \sim 10^{-5}$ to 10^{-6} for either x-rays or neutrons, and generally $\beta \sim 10^{-7}$ or smaller.

To begin with, consider a medium of a pure atomic element. An atom may absorb x-ray radiation at or near a given wavelength very strongly. This will occur for x-ray radiation with a photon energy very near the binding energy of an electron of that element. Away from any such values for λ, the index of refraction can be calculated by using:

$$\delta_x = \frac{\lambda^2}{2\pi} r_e \rho_e, \beta_x = \frac{\lambda}{4\pi} \mu_x, \tag{2.6}$$

where $r_e = e^2/(4\pi\epsilon_0 \mathrm{mc}^2) = 2.814 \times 10^{-6}$nm is the classical electron radius, ρ_e is the electron density of the element, which is simply the atomic number of the element multiplied by its numerical density (atoms per unit volume), and μ_x is the linear absorption coefficient of the material. The term $r_e \rho_e$ is the scattering length density of the element for x-rays. For neutrons these terms are calculated similarly:

$$\delta_n = \frac{\lambda^2}{2\pi} \mathrm{b} \rho_n, \beta_n = \frac{\lambda}{4\pi} \mu_n. \tag{2.7}$$

The term $\mathrm{b}\rho_n$ is the scattering length density for neutrons of a given element, ρ_n is the density of nuclei, and b is the scattering length of a nucleus of the material.

From Equation 2.6 we see that δ_x will increase monotonically across the periodic table. This is not the case for δ_n, as b does not vary monotonically, and will even differ between isotopes of the same element. This difference in behavior in neutron and x-ray scattering densities has useful implications. For some systems, where one technique is of little use because of the contrast (or lack thereof) between components of a system, the other technique may be useful. Also, the two techniques can often be used to study the same system

in complementary ways. It should also be noted that whereas b, and therefore δ_n can be negative, $\delta_e \geq 0$ always, meaning that $\mathrm{Re}(n_{\mathrm{xray}}) \leq 1$ always.

For a composite material of constant composition one can calculate the refractive index by summing over all elements:

$$n = 1 + \sum_{j=1}^{N} \phi_j(-\delta_j + \mathrm{i}\beta_j), \tag{2.8}$$

where ϕ_j is the relative volume fraction of element j in the medium.

Ignoring absorption for a moment, in general when radiation incident from a material of higher bulk index of refraction impinges on a material of lower bulk index of refraction at or below a sufficiently small angle, referred to as the critical angle θ_c, all the incident radiation is reflected. This can be seen from Snell's law of refraction, which given the incident angle of the incident beam θ_i, gives the angle θ_t of the transmitted beam:

$$\frac{\mathrm{Cos}(\theta_i)}{\mathrm{Cos}(\theta_t)} = \frac{n_t}{n_i}. \tag{2.9}$$

Given that $\mathrm{Cos}(\theta_t) \leq \mathrm{Cos}(0) = 1$ for any real θ_t, for $n_t < n_i$, there will be no transmitted radiation for $\mathrm{Cos}(\theta_i) < n_t/n_i$, and we define

$$\theta_c \equiv \mathrm{ArcCos}(n_t/n_i). \tag{2.10}$$

Here we can approximate θ_c:

$$\mathrm{Cos}(\theta_c) \approx 1 - {\theta_c}^2/2 \approx \frac{1-\delta_t}{1-\delta_i} \Rightarrow \theta_c \approx \sqrt{2\,(\delta_t - \delta_i)}. \tag{2.11}$$

The smaller the difference in refractive index between the two materials the smaller θ_c, and the faster the drop off in reflected intensity above θ_c. Because δ is generally very small, θ_c is typically between 0.001 and 0.01 rad, and $R(10\theta_c) \lesssim 10^{-6}R(\theta_c)$. Reflectometry measurements are thus in general performed with the beam incident from a material of higher refractive index, at angles near grazing incidence. The measurements will include angles below θ_c in order to aid normalizing the data. Measurements above $10\theta_c$ generally become impractical because of the small amplitude of reflection.

2.1.2 Solving Maxwell's equations

There are in general two approaches to finding a surface profile consistent with reflectometry data. One can take a model for the composition and structure of the sample of interest, infer from that model a refractive index as a function of depth $n(z)$, and simulate the reflectometry experiment computationally. Parameters of the model can be varied to attempt to fit the simulation to experimental data. A very simple example of this might be a study of a film of known constant composition, but unknown roughness σ_1 and thickness l_1 on a substrate of known roughness. One can easily vary σ_1 and l_1 in a fit routine until the simulation agrees well with actual measurement. Alternatively, one can attempt to infer a profile directly from the data. Such techniques make use of the physics of scattering from a single particle (i.e., electrons in the case of x-rays, atomic nuclei in the case of neutrons), and integrate this over the depth of the sample under study. An approximation made in this technique is that of weak scattering, which is inaccurate very near the critical angle. This method is used in chapter 4, and is discussed more there.

In the first approach, given a model for the surface profile under study, one solves Maxwell's equations numerically to simulate the reflectometry measurement. For radiation polarized perpendicular to the plane of incidence, incident on a perfectly smooth interface between two media of constant composition, as in figure 2.1, the Fresnel formulas for the coefficients of reflection and transmission of radiation are:

$$r_s = \frac{k_{i,z} - k_{t,z}}{k_{i,z} + k_{t,z}}. \tag{2.12}$$

and

$$t_s = \frac{2k_{i,z}}{k_{i,z} + k_{t,z}}. \tag{2.13}$$

Here $k_{i,z}$ and $k_{t,z}$ refer to the magnitude of the z components of the wave numbers of the incident and transmitted beams respectively. For radiation polarized parallel to the incident

plane we have:

$$r_p = \frac{\left(\frac{n_t}{n_i}\right)^2 k_{i,z} - k_{t,z}}{\left(\frac{n_t}{n_i}\right)^2 k_{i,z} + k_{t,z}} \tag{2.14}$$

and

$$t_p = \frac{2k_{i,z}}{\left(\frac{n_t}{n_i}\right)^2 k_{i,z} + k_{t,z}}. \tag{2.15}$$

As the index of refraction will be very close to 1 for x-ray and neutron reflectometry, there is usually no practical difference between radiation of different polarizations in these techniques. Whereas there are variants of both x-ray and neutron reflectometry where polarization is very important, these variants are outside of the scope of this work, and all polarization herein will be treated as being perpendicular to the incident plane. A derivation of Equation 2.14 and Equation 2.15 will be given later.

Examples of the simple case above, such as radiation incident from air on a smooth silicon substrate, are not particularly interesting. One typically will deal with systems of either layered films, as in figure 2.2, of finite roughness on some substrate, more complicated systems wherein composition varies continuously as a function of depth, as in figure 2.3, or systems wherein there is substantial variation of composition within a plane parallel with the interface. In the first case Maxwell's equations can in principle be solved directly. This can be done through an iterative technique that will be discussed presently. In the more complicated cases one will typically simplify the problem by approximating the system under study as a series of layered films of constant composition, and treat the problem like that depicted in figure 2.2.

In figure 2.1 radiation (either a neutron or an x-ray beam) is propagating through medium 1 with a constant index of refraction n_1. The magnitude of the z component of the wave number of the incident beam is given by $k_{i,z} = |\vec{k_i}| \operatorname{Sin}(\theta_i)$. (It should be noted that when discussing x-ray and neutron reflectometry, angles are generally measured from a plane parallel to the incident surface, rather than from the normal.) As we are dealing with specular reflection, i.e. $\theta_i = \theta_r$, we have $\vec{k}_{i,z} = -\vec{k}_{r,z}$. In the calculations that follow

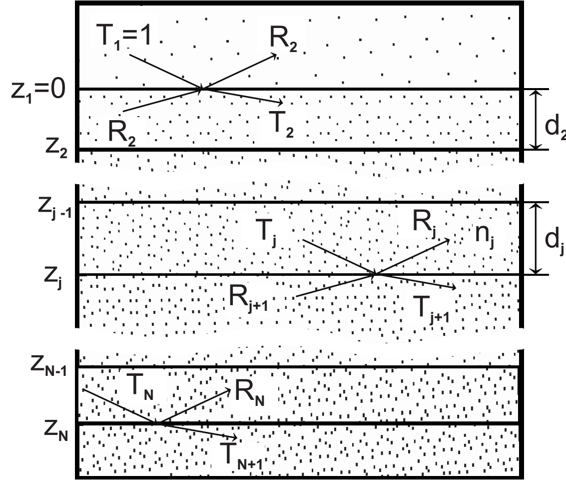

Figure 2.2: *Depiction of reflection from a multilayered surface. At each interface boundary conditions must be satisfied. Note that for the bottom layer the boundary conditions are the same as for figure 2.1, with an incident wave and a reflected wave above the interface, and a transmitted wave below. All other interfaces also have a wave reflected from the interface below.*

it will be the magnitude of k_z for the incident beam that will be relevant to us.

The propagation of electromagnetic radiation, such as x-rays, is described by Maxwell's equations, which we will not describe here. We will instead begin with some results of Maxwell's equations, which we will then use to derive an iterative method for finding the reflectivity from the system depicted in figure 2.2. This iterative technique was first suggested by Parratt[1]. Our derivation loosely follows that of Tolan[2], though we do fill in some details he does not discuss. Recall that we are considering an electromagnetic plane wave, polarized perpendicular to the incident plane, traveling through some medium j and impinging on a flat interface with medium j + 1. We will consider the geometry in figure 2.2. Above an interface the electric field will be composed of both that of the incident wave of amplitude T_j and that of the reflected wave, of amplitude R_j. Below the interface there will be the transmitted wave T_{j+1}, but additionally there will in general be the wave R_{j+1} reflected from the interface at Z_{j+1}. All waves must satisfy the Helmholtz equation,

$$\left(\nabla^2 - k^2\right)\overrightarrow{E} = \left(\nabla^2 - k_0^2 n^2\right)\overrightarrow{E} = 0, \tag{2.16}$$

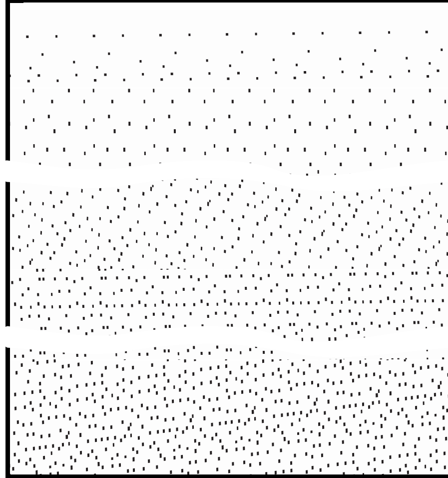

Figure 2.3: *An interface transitioning continuously from the surface composition to the bulk composition. To calculate reflection of incident radiation from such an interface it will typically be approximated as a series of layers of constant composition, as in figure 2.2. For ellipsometry calculations it is generally more efficient to approximate layers of composition which varies linearly with depth.*

where in Cartesian coordinates the operator $\nabla^2 \equiv \frac{\partial^2}{\partial x^2} + \frac{\partial^2}{\partial y^2} + \frac{\partial^2}{\partial z^2}$. There are six terms in the general solution to this equation, but we can limit this by the knowledge that we are confined to the incident plane, and always moving in the positive x direction. We thus have for the amplitude of the electric field in layer j a superposition of two solutions:

$$E_j = \left(A_j^+ e^{-ik_{z,j}z} + A_j^- e^{ik_{z,j}z}\right) e^{i(\omega t - k_{x,j}x)}. \tag{2.17}$$

Clearly the coefficients A_j^+ and A_j^- correspond to T_j, which is moving toward the interface, and R_j, which is moving away, respectively. The mere existence of a boundary condition implies that the spatial and time variation of all fields must be the same on both sides of the boundary. Therefore $k_{x,j} = k_{x,j+1}$ at every interface, and in fact, $k_x = k_{x,1}$ everywhere in figure 2.2 (this is just another expression of Snell's law). The term $e^{i(\omega t - k_{x,j}x)}$ thus becomes irrelevant to our purposes here, as it will be the same on both sides of an interface at all points. For convenience we will use the notation:

$$U_{t,j}(z) \equiv T_j e^{-ik_{z,j}z}, U_{r,j}(z) \equiv R_j e^{ik_{z,j}z}. \tag{2.18}$$

For perpendicularly polarized radiation there are two relevant boundary conditions. First, given that the component of an electric field tangential to an interface must be continuous across that interface (and in our case the whole field is tangential to the interface), we have the condition:

$$U_{t,j}(z_j) + U_{r,j}(z_j) = U_{t,j+1}(z_j) + U_{r,j+1}(z_j). \tag{2.19}$$

Also, for non magnetic media the tangential component of the magnetic field must be continuous across the interface, which leads to the boundary condition:

$$[U_{t,j}(z_j) - U_{r,j}(z_j)] = \frac{k_{z,j+1}}{k_{z,j}}[U_{t,j+1}(z_j) - U_{r,j+1}(z_j)]. \tag{2.20}$$

We divide the difference of the two above equations by their sum, and we get:

$$\frac{U_{r,j}(z_j)}{U_{t,j}(z_j)} = \frac{\left(1 - \frac{k_{z,j+1}}{k_{z,j}}\right) U_{t,j+1}(z_j) + \left(1 + \frac{k_{z,j+1}}{k_{z,j}}\right) U_{r,j+1}(z_j)}{\left(1 + \frac{k_{z,j+1}}{k_{z,j}}\right) U_{t,j+1}(z_j) + \left(1 - \frac{k_{z,j+1}}{k_{z,j}}\right) U_{r,j+1}(z_j)} = \frac{\frac{k_{z,j} - k_{z,j+1}}{k_{z,j} - k_{z,j+1}} + \frac{U_{r,j+1}(z_j)}{U_{t,j+1}(z_j)}}{1 + \frac{k_{z,j} - k_{z,j+1}}{k_{z,j} - k_{z,j+1}} \frac{U_{r,j+1}(z_j)}{U_{t,j+1}(z_j)}} \tag{2.21}$$

We recognize the wave number term as the Fresnel reflection coefficient for perpendicular polarization, and write:

$$r_{j,j+1} \equiv \frac{k_{z,j} - k_{z,j+1}}{k_{z,j} + k_{z,j+1}}, \tag{2.22}$$

and using our definitions for $U_{r,j}$ and $U_{t,j}$ we have:

$$X_j \equiv \frac{R_j}{T_j} = e^{-2ik_{z,j}z_j} \frac{r_{j,j+1} + X_{j+1}e^{2ik_{z,j+1}z_j}}{1 + r_{j,j+1}X_{j+1}e^{2ik_{z,j+1}z_j}}. \tag{2.23}$$

In the last layer $X_{n+1} = R_{n+1} = 0$, as there are no more interfaces from which to reflect. One can thus start from X_n and iteratively solve for X_1, and therefore R_1.

Thus far we have assumed perfectly smooth, flat interfaces between media. In the physical world, at some level no interface can be perfectly flat or smooth. A liquid-vapor interface, for example, will have capillary waves, and a solid-liquid interface will have imperfections on the solid surface. The effect of this roughness can not always be ignored in a reflectometry simulation. To include the effect of roughness at each interface we multiply the

Fresnel reflection coefficient by $\exp(-2k_{z,j}^2\sigma_j^2)$, termed the Beckmann-Spizzichino factor[3]. This results in:

$$X_j \equiv \frac{R_j}{T_j} = e^{-2ik_{z,j}z_j}\frac{\tilde{r}_{j,j+1} + X_{j+1}e^{2ik_{z,j+1}z_j}}{1+\tilde{r}_{j,j+1}X_{j+1}e^{2ik_{z,j+1}z_j}}, \tag{2.24}$$

where

$$\tilde{r}_{j,j+1} = r_{j,j+1}\exp(-2k_{z,j}k_{z,j+1}\sigma_j^2). \tag{2.25}$$

For the sake of the continuity of our current discussion, the derivation of this result will be described later.

Note that the last interface in figure 2.2 is like the special case of a single interface depicted in figure 2.1, wherein there is no reflected component R_2 (i.e., $R_2 = X_2 = 0$). This is the situation described by the Fresnel equations. We see that in a case like figure 2.1, where we set $z_1 = 0$, $X_1 = R_1 = r_{1,2}$. Equation 2.15 arises simply from $t_{1,2} = 1 - r_{1,2}$.

We can make use of Snell's law to calculate $k_{z,j}$ for each layer j:

$$k_{z,j} = \sqrt{k_j^2 - k_{j,x}^2} = \sqrt{k_j^2 - k_1^2\text{Cos}^2(\theta_1)}. \tag{2.26}$$

Rather than considering R as a function of λ or θ_i, in practice one generally works in terms of momentum transfer $\vec{Q}$:

$$\vec{Q} \equiv \vec{k}_r - \vec{k}_i, \tag{2.27}$$

where $\vec{k_i}$ is the wave number of the incident beam, and $\vec{k_r}$ is that of the reflected beam. Reflectometry instruments generally output their data as a function of Q, rather than in terms of λ or θ.

Given that in the bulk of this work we will be considering only specular reflectivity, which is the case in which $\theta_r = \theta_i$, Equation 2.27 becomes:

$$Q = Q_z = 2k_z = \frac{4\pi Sin(\theta_i)}{\lambda} \cong 4\pi\theta_i/\lambda. \tag{2.28}$$

The approximation is valid because one must work near grazing incidence. At the critical angle we define the critical momentum transfer $Q_c \equiv Q(\theta_c)$, below which all incident radiation is reflected (ignoring adsorption).

There are various advantages to working in terms of Q rather than in terms of λ and θ_i. As some reflectometry instruments measure reflection intensity R as a function of λ while holding θ_i constant, and others vary θ_i at constant λ, by working in terms of Q we can keep discussion and analysis independent of a given instrument or technique. In terms of simulating reflectometry mathematically for analysis, one can avoid writing extra software for different types of instruments, which both reduces the likelihood of error by reducing complexity, and can potentially make the software easier to use.

There can also be some direct computational advantages to working in terms of Q. We begin by discussing the case for neutrons, and then generalize. For neutrons one can generally ignore the imaginary part of the refractive index. We then have:

$$k_j = \frac{2\pi n_j}{\lambda} \cong \frac{2\pi}{\lambda}\left(1-\delta_j\right) = \frac{2\pi}{\lambda}\left(1-\frac{\lambda^2}{2\pi}\mathrm{SLD}_j\right), \tag{2.29}$$

where the scattering length density $\mathrm{SLD}_{\mathrm{neutron},j} \equiv \left(\rho_n b\right)_j$.

Now from Equation 2.26, and recalling that for small angles $\mathrm{Cos}(\theta) \cong 1-\theta^2/2$,

$$k_{z,j} \cong \sqrt{\left[\frac{2\pi}{\lambda}\left(1-\frac{\lambda^2}{2\pi}\mathrm{SLD}_j\right)\right]^2 - \left[\frac{2\pi}{\lambda}\left(1-\frac{\lambda^2}{2\pi}\mathrm{SLD}_1\right)\right]^2 (1-\theta^2)}. \tag{2.30}$$

Keeping second order terms,

$$k_{z,j} \cong \sqrt{4\pi(\mathrm{SLD}_j - \mathrm{SLD}_1) + \frac{4\pi^2}{\lambda^2}\theta^2} \cong \sqrt{4\pi(\Delta SLD_j) + Q^2/4}. \tag{2.31}$$

Equation 2.31 clarifies the calculation by separating the radicand into a scattering length density term, which comes directly from the modeled profile, and a momentum transfer term, which is the form the independent data for the calculation will usually take. Equation 2.26 and Equation 2.31 are fairly equivalent in the required number of computational operations per simulation if the instrument is varying the angle and holding wavelength constant, as in both cases the profile information (k_j or $4\pi(\Delta SLD_j)$) need be calculated once per reflectivity curve, and the terms ($k_1^2\mathrm{Cos}^2(\theta_1)$ or $0.25Q^2$) once per data point. On the other hand, if the instrument varies wavelength while holding angle constant, if using Equation 2.26 the dependence of k_j on λ requires one to either recalculate the entire profile for every

data point, or to simulate the calculation by pretending that it is θ that is being varied rather than λ. The first option can be very computationally expensive if the profile is simulated with many layers, and the second is unaesthetic, overly complicated, and can lead to errors elsewhere by causing incorrect assumptions. Finally, notice that Equation 2.26 involves the subtraction of two terms that are typically many orders of magnitude greater than their difference, as the incident angle will generally be very small, and the refractive indices for neutron and x-ray reflectometry are typically very close to 1. This necessitates a choice between computational cost and accuracy that is much less an issue in Equation 2.31.

For x-ray reflectometry one often need be far more concerned about absorption, especially near an absorption edge. We can still use Equation 2.31 by defining SLD as a complex quantity including the absorption coefficient of the medium:

$$\mathrm{SLD}_{\mathrm{xray},j} \equiv \rho_e r_e - \frac{i}{2\lambda}\mu_x. \tag{2.32}$$

While this does unfortunately include the wavelength of the x-ray beam in the profile calculation, this is not as much as of an issue as it would be with neutron reflectometry because λ is generally held constant while measuring an x-ray reflectometry curve, θ being varied instead. One will therefore not need to recalculate the entire scattering length density profile for each simulated data point. Thus one still benefits from all the advantages of Equation 2.31

2.1.3 Software model of reflectometry

A complete listing of the computer code used in calculating a reflectometry curve for a given profile and incident beam is beyond the scope of the current chapter, but can be obtained from

http://www.mattbrownswebsite.com/professional/SimulationCode/ReflectometryCode.aspx.

Here we explain various parts of the software in the context of our current discussion. The bulk of our reflectometry calculations are done by a c++ class called ReflectometerNative. In calculating a reflectometry curve the first step is to represent a profile in terms of a series

of slabs of uniform composition. As the mechanism of converting an adsorption profile into a series of uniform layered slabs has nothing to do directly with reflectometry, this is done external to ReflectometerNative, and the results are passed to ReflectometerNative in the form of an object of class ProfileContaier.

```
ReflectometerNative(ProfileContainer * t_profileContainer)
{
    this- > Initialize(t_profileContainer);
}
```

The object of class ProfileContainer which is passed to ReflectometerNative contains an array which represents the profile as a series of slabs, with each slab being represented by an object of class ProfileSlab. Each ProfileSlab will have information about its width, scattering length density, and the roughness of its top interface. When ReflectometerNative is initialized this profile is converted to a form wherein each layer will have the result of the scattering length density term from Equation 2.31.

/* Initializes or reinitializes both the profileContainer field and fields directly related to the contents of profileContainer.*/

```
void Initialize(ProfileContainer * t_profileContainer)
{
    this- >profileContainer = t_profileContainer;
    this- >sldFactorProfile = this- >ScattLengthDensfactor(
```

```
    this− >profileContainer− >GetProfileSlab_Unchecked(0), this-¿profileContainer− >get_Length());
    this− >profileDepth = this− >GetProfileDepth();
}

/* Returns a representation of the scattering length density profile. Each slab contains
the value 4 * pi * (sld_top - sld_current). This part of the calculation is independent
of Q, and is stored here so as to only need to be calculated once for a given profile,
rather than for each value of Q. */

complex<float> * ScattLengthDensfactor(ProfileSlab * l_slabList, int slabCount)
{
    complex<float> * sldProfile = new complex<float>[slabCount];
    complex<float> sldTop = l_slabList[0].get_ScatteringLengthDensity();
    for(int slabIndex = 0; slabIndex < slabCount; slabIndex++)
    {
        complex<float> sldCurrent = l_slabList[slabIndex].get_ScatteringLengthDensity();
        sldProfile[slabIndex] = unit_Times_4_pi * (sldTop - sldCurrent);
    }
    return sldProfile;
}
```

Once the ReflectometerNative object is initialized the function ReflectivityCurve can be called to calculate the simulated reflectometry data. An Array is initialized to hold the results of the simulation data, and the Q dependent term in Equation 2.31 is calculated for each independent data point that will be used. A roughness term is calculated for each slab, and the results stored in an array. Finally, a loop iterates over the dependent data terms, calculating a reflectivity point for each qFactor.

/* Returns a reflectivity curve assuming no spread in Q. That is, each point is calculated under the assumption that Q is infinitely sharp. */

```
inline float * ReflectivityCurve(float * momentumTransfer, int l_length)
{
    float * reflectivitySimData = new float[l_length];
    float * qFactor = this- >MomentmTransFactor(momentumTransfer, l_length);
    this- >roughness = this- >FindRoughness();
    for (int index = 0; index < l_length; index ++)
    {
        reflectivitySimData[index] = this- >ReflectivityPoint(qFactor[index]);
    }
    delete (qFactor);
    return reflectivitySimData;
}

float * FindRoughness()
{
    ProfileSlab * profileSlab = this- >profileContainer- >GetProfileSlab_Unchecked(0);
    int length = this- >profileContainer- >get_Length();
    float * l_roughness = new float[length];
    for (int index = 0; index < length; index ++)
    {
        l_roughness[index] = profileSlab[index].get_SigmaTopSquared();
    }
    return l_roughness;
```

```
}
```

Each reflectivity point is calculated using Equation 2.24. The function ReflectivityPoint keeps track of the previous R/T ratio, as well as the previous wave number as it loops over all the layers in the profile to calculate the R/T ratio for each one by calling the function GetRTRatio. GetRTRatio in turn finds the current Fresnel reflectivity coefficient, multiplies by the roughness term if it is significant, and finally calculates the ratio. Note that for profiles represented by many layers, only a few of which have significant roughness terms, one could probably make a worthwhile improvement in efficiency by dividing the profile up at layers with roughness terms, thus avoiding many unnecessary calculations.

```
 /* finds reflectivity for a single value of q (momentum transfer). This is done
under the assumption that there is no spread in q. (ie, q is infinitely sharp) */

inline float ReflectivityPoint(float qFactor)
{
    complex<float> rtRatio;
    complex<float> rtRatio_Previous = 0;
    int slabCount = this->profileContainer->get_Length();
    float depthCurrent = 0.0f;
    complex<float>waveNumber_Z;
    complex<float> waveNumber_Z_Previous = this->GetWaveNumberZ(qFactor,
        this->sldFactorProfile[slabCount-1]);

    for (int slabIndex = slabCount - 2; slabIndex > -1; slabIndex--)
    {
        waveNumber_Z = this->GetWaveNumberZ( qFactor, sldFactorProfile[slabIndex]);
```

```
        rtRatio = this−>GetRtRatio(rtRatio_Previous, waveNumber_Z,
            waveNumber_Z_Previous, this−>profileDepth[slabIndex+1],
            this−>roughness[slabIndex+ 1]);
        waveNumber_Z_Previous = waveNumber_Z;
        rtRatio_Previous = rtRatio;
    }
    return NormSquared(rtRatio);
}

inline complex<float> GetWaveNumberZ(float qFactor, complex<float>sldPartCurrent)
{
    complex<float> value = sqrt(qFactor + sldPartCurrent);
    return value;
}

/* gets the ratio of reflectivity coefficient over transmittivity coefficient.*/

inline complex<float> GetRtRatio(complex<float> rtRatio_prev,
    complex<float> waveNumber_Z, complex<float>waveNumber_Z_Previous,
    float depthCurrent, float t_roughnessFactor )
    {
    complex<float> fresnelCoefficient=this−>FresnelCoefficient
        (waveNumber_Z,waveNumber_Z_Previous);
    if(t_roughnessFactor > 1e-3)
    {
        fresnelCoefficient *= exp(-2.0f * waveNumber_Z * waveNumber_Z
            * t_roughnessFactor);
```

```
    }

    complex<float> phaseIncident = this->Phase(-depthCurrent, waveNumber_Z);
    complex<float> phaseTransmit = this->Phase(depthCurrent, waveNumber_Z_Previous);
    complex<float> rtRatio_Prev_X_PhaseTr = rtRatio_prev * phaseTransmit;
    return phaseIncident * (fresnelCoefficient + rtRatio_Prev_X_PhaseTr)
        /(1.0f + fresnelCoefficient * rtRatio_Prev_X_PhaseTr);
    }

inline static float NormSquared(complex<float> complexValue)
{
    float absValue = abs(complexValue);
    return absValue * absValue ;
}
```

2.1.4 Including surface roughness

The following methodology for handling roughness is described in Tolan[2] and references therein. We loosely follow his outline, again adding some details he does not discuss. Rather than being perfectly smooth, real world interfaces will have some roughness, as depticted in figure 2.4 a. Roughness is often simulated by representing a rough interface at a depth z_j as an ensemble of smooth interfaces with a depth $z_j + z(x, y)$, as depticted in figure 2.4 b. The value of $z(x, y)$ is weighted by a probability density $P_j(z)$. So to get X_j, one averages X_j(x,y) over the interface. The mean value of $\mu_j \equiv z(x, y)$ is given by:

$$\mu_j = \int zP_j(z)dz, \tag{2.33}$$

with root mean square roughness given by

$$\sigma_j^2 = \int (z - \mu_j)^2 P_j(z)dz. \tag{2.34}$$

One can simulate roughness by using a profile wherein $n(z)$ in the vicinity of the inter-

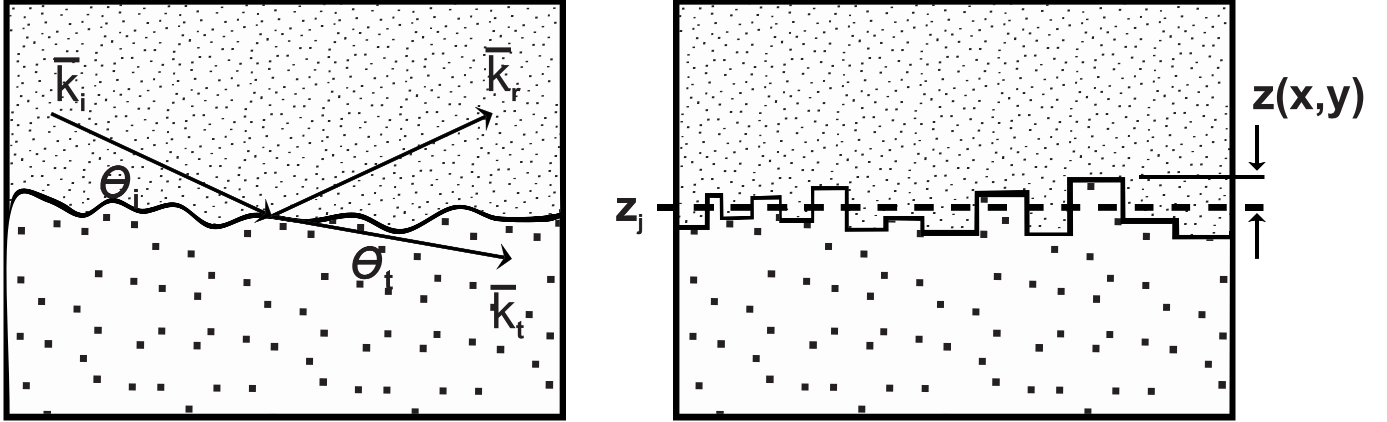

Figure 2.4: *a.) Depiction of a rough interface between two media. b.) A rough interface can be simulated as an ensemble of smooth interfaces displaced from the average depth z_j by some value $z(x, y)$.*

face represents the refractive index averaged over the x-y plane at depth z. This can be represented as

$$n(z) = \frac{n_j + n_{j+1}}{2} + \frac{n_j - n_{j+1}}{2} \int_z^{\infty} P(\mathrm{z}')d\mathrm{z}'. \tag{2.35}$$

The above could now be used to simulate the interface itself as a series of uniform layers. To see why, if at a particular point $\{x', y', z'\}$, the interface lies at $z > \mathrm{z}'$, then $n(\mathrm{x}', \mathrm{y}', \mathrm{z}') = n_j$. Otherwise $n(\mathrm{x}', \mathrm{y}', \mathrm{z}') = n_{j+1}$. In taking this approach, one simply replaces the integral with the function one wishes to use to approximate the interfacial transition. A common choice is to use an error function:

$$\mathrm{erf}(x) = \frac{2}{\sqrt{\pi}} \int_0^z e^{-t^2} dt \tag{2.36}$$

$$n(z) = \frac{n_j + n_{j+1}}{2} - \frac{n_j - n_{j+1}}{2} \mathrm{erf}\left(\frac{z - z_j}{\sqrt{2\sigma_j}}\right). \tag{2.37}$$

However one can often accomplish the same thing in a more efficient manner, replacing a series of layers used to represent roughness with a simple factor included in the Fresnel reflection coefficient. We will use the error function above to illustrate the procedure. The

first step is to find the probability function associated with the chosen roughness profile representation by differentiation. Here we have

$$P_j(z) = \frac{1}{\sqrt{2\pi}\sigma_j} \exp\left(\frac{z^2}{2\sigma_j^2}\right). \tag{2.38}$$

This result is then used to average the effect on X_j of offsetting the z coordinate of the interface.

Rather than trying to average over X_j to determine the effect of roughness on reflectivity, we instead solve Equation 2.20 and Equation 2.21 for R_j and T_j in terms of R_{j+1} and T_{j+1} and the Fresnel reflection and transmission coefficients $r_{j+1,j}$ and $t_{j+1,j}$:

$$R_{j+1,j} = \frac{1}{t_{j+1,j}} \left\{T_j r_{j+1,j} \exp[-i(k_{z,j+1} + k_{z,j})z_j] + R_j \exp[-i(k_{z,j+1} - k_{z,j})z_j]\right\} \tag{2.39}$$

$$T_{j+1,j} = \frac{1}{t_{j+1,j}} \left\{T_j \exp[i(k_{z,j+1} - k_{z,j})z_j] + R_j r_{j+1,j} \exp[i(k_{z,j+1} + k_{z,j})z_j]\right\} \tag{2.40}$$

We now average $R_{j+1,j}$ and $T_{j+1,j}$, and defining a phase factor average f_j as

$$f_j(k) \equiv \exp(ik\mu_j) \int \exp(-ikz) P_j(z) dz, \tag{2.41}$$

we can write the results as:

$$\tilde{R}_{j+1} = \frac{1}{\tilde{t}_{j+1,j}} \left\{T_j \tilde{r}_{j+1,j} \exp[-i(k_{z,j+1} + k_{z,j})z_j] + R_j \exp[-i(k_{z,j+1} - k_{z,j})z_j]\right\} \tag{2.42}$$

$$\tilde{T}_{j+1,j} = \frac{1}{f_t \tilde{t}_{j+1,j}} \left\{T_j \exp[i(k_{z,j+1} - k_{z,j})z_j] + R_j f_r \tilde{r}_{j+1,j} \exp[i(k_{z,j+1} + k_{z,j})z_j]\right\} \tag{2.43}$$

Here we have the Fresnel coefficients for rough interfaces:

$$\tilde{r}_{j+1,j} = \frac{f_j(k_{z,j+1} + k_{z,j})}{f_j(k_{z,j+1} - k_{z,j})} r_{j+1,j} \tag{2.44}$$

$$\tilde{t}_{j+1,j} = \frac{1}{f_j(k_{z,j+1} - k_{z,j})} t_{j+1,j}, \tag{2.45}$$

and f_r and f_t are defined by

$$f_r \equiv \frac{f_j(k_{z,j+1} - k_{z,j})}{f_j(-k_{z,j+1} + k_{z,j})} \frac{f_j(-k_{z,j+1} - k_{z,j})}{f_j(k_{z,j+1} + k_{z,j})} \tag{2.46}$$

$$f_t \equiv \frac{f_j(k_{z,j+1} - k_{z,j})}{f_j(-k_{z,j+1} + k_{z,j})}. \tag{2.47}$$

If the arguments are real numbers (i.e., no absorption), $|f_r| = |f_t| = 1$. This is true to a good approximation even near the critical angle where absorption is present. Thus the only important difference between the pair of equations 2.42 and 2.43 on the one hand, and equations 2.39 and 2.40 on the other, is the substitution of $\tilde{r}_{j,j+1}$ and $\tilde{t}_{j,j+1}$ for their smooth interface counterparts. We then make this same substitution in Equation 2.23 (or simply derive this result from Equation 2.42 and Equation 2.43) we get

$$\tilde{X}_j \equiv \frac{R_j}{T_j} = e^{-2ik_{z,j}z_j} \frac{\tilde{r}_{j,j+1} + X_{j+1}e^{2ik_{z,j+1}z_j}}{1 + \tilde{r}_{j,j+1}X_{j+1}e^{2ik_{z,j+1}z_j}}. \tag{2.48}$$

The task of finding roughness is now reduced to representing the roughness of an interface with a probability function that can be used in Equation 2.41 in order to calculate the roughness Fresnel reflection coefficient via Equation 2.44. In the case of the error function we used above, we get what is referred to as the Nevot-Croce factor[4] ,

$$\tilde{r}_{j,j+1} = r_{j,j+1} \exp(-2k_{z,j}k_{z,j+1}\sigma_j^2). \tag{2.49}$$

In the analysis discussed herein we use primarily another factor which can be derived by using an error function profile, but wherein the averaging is done over Equation 2.19 and Equation 2.20. This results in the Beckmann-Spizzichino factor[3]

$$\tilde{r}_{j,j+1} = r_{j,j+1} \exp(-2k_{z,j}^2\sigma_j^2). \tag{2.50}$$

The above results were originally obtained by solving the Helmholtz equation, Equation 2.16, directly for error factor profiles, but each using a different set of approximations. Beckmann and Spizzichino[3] assumed the local surface curvature to be much smaller than the wavelength of the incident beam. Nevot and Croce[4] assumed a rapid change in local surface curvature. In practice the results differ very little provided that surface roughness is sufficiently small, so we chose to use Equation 2.50 for computational efficiency.

2.1.5 Resolution

The discussion thus far has assumed a monochromatic beam incident at a specific angle. In reality a beam can not be perfectly monochromatic, and a beam of finite width will

include particles incident at a small range of angles. Both these factors produce a spread in momentum transfer for a given measurement. A given measurement is thus an average taken over a range ΔQ, weighted by some distribution function, typically taken as a gaussian. This is a particular concern near Q_c, where drop off in intensity is generally very rapid. For a beam centered at Q just above Q_c, contributions from below Q_c will reduce the magnitude of the reflectivity, thus rounding the critical edge. Just below Q_c the contributions from a small region of size ΔQ just below Q may involve reflectivities so much higher than the value at Q so as to dominate the signal, resulting in a much higher value for R than a theory assuming discrete values for Q would indicate.

Resolution was not a concern for the x-ray reflectometry experiment discussed in later chapters. Firstly, for an x-ray beam, typically $\Delta\lambda/\lambda < 10^{-4}$, which can be taken as monochromatic. Secondly, the beam intensity at APS is such that near θ_c, where resolution tends to be an issue, a beam of width $\sim 1mm$ will provide a sufficient reflected beam. In the case of either table top x-ray reflectometer machines, or neutron reflectometers the incident beam intensity is much lower, and one typically chooses beam dimensions which will utilize as much of the sample surface as possible. For our neutron reflectometry experiment we used a sample surface of $\sim$ 2.5 cm wide and 5 cm long. The instrument was programmed to make maximum use of this area for each measurement, resulting in $\Delta\theta/\theta \sim 0.025$. Also, for the instrument we used, $\Delta\lambda/\lambda = 0.025$. Because of the small critical angle of our sample, the reasons for which are discussed in chapter 5, resolution was a real concern. Simulations including finite resolution had to be done to either eliminate resolution as a concern, or to model the data correctly if effects due to finite resolution proved to be important. It turned out that resolution was not an issue in our case, but a brief discussion is included for completeness. Again we loosely follow an outline given my Tolan[2] .

When considering only radiation confined to the incident plane we need consider resolution in the x and z directions. In our case we do not expect specific variations in R in the x direction, and since we are considering specular reflection we are treating any x component

of the momentum transfer as being negligible anyway (hence Equation 2.28), so we only concern ourselves here with resolution in the z direction.

Differentiating Equation 2.28 with respect to both λ and θ, and combining the absolute values of the results, we get:

$$\varrho_z = \frac{4\pi}{\lambda}\Delta\theta + \frac{4\pi}{\lambda^2}\theta\Delta\lambda = Q\left(\frac{\Delta\theta}{\theta} + \frac{\Delta\lambda}{\lambda}\right). \tag{2.51}$$

The practical task of simulating finite resolution of a beam is accomplished by choosing a set of wave vector values K_i centered around, and within a specified range of Q. We calculate reflectivity for all of these points, and convolve the results based on a gaussian distribution. The class ReflectometerNative has a function ReflCurveZResolution to calculate a reflectivity curve taking finite resolution in z into account. This function makes use of the class ResolutionCalc to handle calculations not directly related to reflectometry.

```
float * ReflCurveZResolution(float * momentumTransfer, int l_length,
    float deltaLambdaRatio, float deltaThetaRatio, int pointsEachSide,
    float resQstepDenominator)
{
    int pointsCount = pointsEachSide * 2 + 1;
    float * reflectivitySimData = new float[ l_length];
    int qIndex;
    for(qIndex = 0; qIndex < l_length; qIndex ++)
    {
        float qCurrent = momentumTransfer[qIndex];
        float * resolutionQList = ResolutionCalc::GetResQList(qCurrent, deltaThetaRatio,
            pointsEachSide, resQstepDenominator);
        float * resolutionReflData = this- >ReflectivityCurve(resolutionQList, pointsCount);
        reflectivitySimData[qIndex] = ResolutionCalc::ConvolveReflData(resolutionQList,
```

```
        resolutionReflData, pointsCount, pointsEachSide, deltaLambdaRatio, deltaThetaRatio);
    delete(resolutionQList, resolutionReflData);
  }
  return reflectivitySimData;
}
```

The following functions are from the class ResolutionCalc. They are all static functions, meaning that an object of class ResolutionCalc isn't created in order to call these functions.

```
/* given a q value, returns a list of equally spaced values, with q as the middle value.
pointsEachSide is the number of values above and below q. deltaThetaRatio is Q/deltaQ.
The step size is ~ proportional to deltaQ (deltaThetaRatio * q), and
inversely proportional to stepSizeDenominator. Setting stepSizeDenominator = 1.0f will
set the step size to (deltaThetaRatio * q) */

inline static float * GetResQList(float q, float deltaThetaRatio, int pointsEachSide,
  float stepSizeDenominator)
{
  int pointCount = pointsEachSide * 2 + 1;
  float * qList = new float[pointCount];
  int midPoint = pointsEachSide; // because of the zero offset
  qList[midPoint] = q;
  if(pointsEachSide > 0)
  {
    float stepSize = q * deltaThetaRatio/stepSizeDenominator;
    for(int index = 0; index < pointsEachSide; index++)
    {
```

```
            int stepsFromMidPoint = pointsEachSide - index;
            qList[index] = q - stepSize * stepsFromMidPoint;
            qList[pointCount - 1 - index] = q + stepSize * stepsFromMidPoint;
        }
    }
    return qList;
}

inline static float ConvolveReflData(float * qList, float * reflData, int l_length,
    int pointsEachSide, float deltaLambdaRatio, float deltaThetaRatio)
{
    float normalization = 1;
    int middlePointIndex = pointsEachSide;
    float reflPointSum = reflData[middlePointIndex];
    float middleQ = qList[middlePointIndex];
    for(int index = 0; index < l_length; index ++)
    {
        if(index != middlePointIndex)
        {
            float qCurrent = qList[index];
            float deltaQz = DeltaQz(qCurrent, deltaLambdaRatio, deltaThetaRatio);
            float qResolution = middleQ - qCurrent;
            float gaussResFactor = GausianResolutionFactor(qResolution, deltaQz);
            reflPointSum += reflData[index] * gaussResFactor;
            normalization += gaussResFactor;
        }
    }
```

```
    return reflPointSum / normalization;
}

/* returns a resolution factor for Qz, which is a measure of how sharply Q
can be defined. */

inline static float DeltaQz(float q, float deltaLambdaRatio, float deltaThetaRatio)
{
    float value = q * (deltaLambdaRatio + deltaThetaRatio);
    return value;
}

/* Given a Q resolution and deltaQz, which is a factor dependent upon the sharpness
with which Q can be defined, returns a gaussian factor */

inline static float GausianResolutionFactor(float qResolution, float deltaQz)
{
    float argument = - qResolution * qResolution * (0.5f * gaussExpFactor)
        / ( deltaQz *  deltaQz); return exp(argument);
}
```

Simulations done with the above code indicated that resolution was not an issue in our neutron reflectometry measurements. In fact to begin to see a significant difference by including resolution we had to use $\Delta\theta/\theta = 0.05$, double what our calculations gave based on the geometry of the beam line and sample cell.

Neutron and x-ray reflectometry are versatile techniques, of which we have only touched the basics here. We discussed the basic physics, and outlined how these techniques can be modeled with software. We also stuck with the special case of specular reflectivity. Off spec-

ular measurements are important in determining background for a specular measurement, and also have direct applications on their own. Measurements in which neutrons of different spin polarizations are distinguished are important in studying magnetic materials. The availability of modern x-ray facilities which produce highly coherent beams can be used to investigate surface correlation features. A discussion of these variations is, however, beyond our scope.

2.2 Ellipsometry

Ellipsometry is a technique wherein surface structure is probed by measuring the effect that reflection from a surface has on the elliptical polarization of light. It was data acquired by this technique by Smith and Law[5 6 7] that was successfully described by Carpenter et al. with universal scaling theory. While we do not describe new data from this technique here, we do describe retrospective analysis of ellipsometry data acquired by Cho, Law, and Grey[8]. The purpose of this section is to give a brief overview of ellipsometry, and of some of the physics we use in analyzing ellipsometric data. As it is not the primary technique used in the research described in this work, we do not give a full description. For a much more detailed description, as well as a full derivation of the following outline, please see ref.[9] . Note that by convention, for radiation of visible wavelengths reflecting from a surface the incident and transmitted angles are measured from the normal of the surface. Also note that in choosing symbols to represent variables in both this section and the last we try to be consistent with symbols found in the literature regarding the respective techniques. This unfortunately leads to using Q in this section to represent a vector in a matrix equation, whereas it was used as a wave vector in the previous section.

We begin with a brief reminder of the definition of Brewster's angle, as this is the angle at which Ellipsometry measurements are generally taken. We then define the coefficient of ellipticity and what it means. Finally we derive a method by which Maxwell's equations can be solved numerically to simulate ellipsometry measurements.

For $\lambda \sim 0.1$nm, as is typical for the reflectometry techniques described above, there is usually no practical difference between radiation polarized perpendicular and parallel to the incident plane. For optical wavelengths, where differences in refractive index can be large, the difference in reflection coefficients for the two polarizations become significant. This difference is the basis of ellipsometry.

Writing the Fresnel coefficient for parallel polarized radiation as

$$r_p = \frac{\cos\theta_i - (n_i/n_t)\cos\theta_t}{\cos\theta_i + (n_i/n_t)\cos\theta_t}, \tag{2.52}$$

and combining this with Snell's law

$$n_i \sin\theta_i = n_j \sin\theta_j, \tag{2.53}$$

it can be shown that there is an angle, defined as the Brewster angle θ_B, such that there will be no reflected component:

$$\frac{n_t}{n_i} = \tan\theta_B. \tag{2.54}$$

For an interface in the physical world, wherein transition from n_i to n_t will occur over a finite length scale, r_p will generally not fall to zero, and the Brewster angle is defined as the angle at which the real part of r_p is minimized. This is the angle typically chosen for an ellipsometry measurement both as a suitable fixed point of reference and because of the mathematical simplicity of analyzing the result.

The parameter of interest in ellipsometry, called the coefficient of ellipticity, is the imaginary part of the ratio of perpendicular and parallel reflection coefficients:

$$\overline{\rho} \equiv \mathrm{Im}\left(\frac{r_p}{r_s}\right). \tag{2.55}$$

Rather than depending on a change in relative intensities, $\overline{\rho}$ is a measure of the relative phase shift between perpendicular and parallel polarized components that results from reflection. It is this that makes possible resolutions of 0.05 nm or better, in spite of using radiation with $\lambda = 632.8$ nm, for example.

The value of $\overline{\rho}$ will depend on both the shape of the interfacial profile by way of the spatial dependence of the refractive index, as well as the length scale over which the profile occurs. If $\overline{\rho}$ is measured as a function of λ, the case referred to as spectroscopic ellipsometry, one can determine both the shape of a profile, as well as its length scale. The measurements taken by Smith and Law[5 6,7], and later analyzed by Carpenter et al.[1] , were done with monochromatic ellipsometry; i.e., at constant wavelength. A single ellipsometric measurement would therefore not suffice to determine both the shape and length scale of a profile. However, Carpenter et al. were testing a theory wherein the profile was expected to scale with temperature in a known way. This allowed them to use temperature as the independent parameter. We mention here that the variation of $\overline{\rho}$ with θ is such that θ is not a viable independent parameter.

In the Parratt formalism described above for reflectometry we used an iterative approach to solve Maxwell's equations numerically to simulate reflectometry from a layered system. We use a similar approach in analyzing ellipsometry data from a continuous profile. The profile is approximated as a series of layers, and Maxwell's equations are solved iteratively over all layers to meet expected boundary conditions. We here describe a method wherein the solution to Maxwell's equations at each interface is described with a 2 x 2 matrix, the solution for the whole profile being obtained by matrix multiplication. We outline the approach for light polarized parallel to the incident plane. The case for perpendicular polarization can then be found by a simple substitution. We begin by assuming solutions of the form

$$\overrightarrow{E}(\overrightarrow{r},t) = \hat{x}U(z)e^{i(k_0\alpha y-\omega t)}, H_y = V(z)e^{i(k_0\alpha y-\omega t)} \tag{2.56}$$

to the following set of second order differential equations which arise from Maxwell's equations:

$$\frac{d^2U}{\mathrm{dz}^2} - \frac{d(\ln\mu)}{\mathrm{dz}}\frac{\mathrm{dU}}{\mathrm{dz}} + k_0^2(n^2-\alpha^2)U = 0, \tag{2.57}$$

$$\frac{d^2V}{\mathrm{dz}^2} - \left[\frac{d}{\mathrm{dz}}\ln(\epsilon - \frac{\alpha^2}{\mu})\right]\frac{\mathrm{dV}}{\mathrm{dz}} + k_0^2(n^2-\alpha^2)V = 0. \tag{2.58}$$

We will have two pair of linearly independent solutions $\{U_1, V_1\}$, and $\{U_2, V_2\}$, which are not unique. Given an arbitrary set of boundary conditions

$$U(0) = u, V(0) = v, \tag{2.59}$$

we can write the solution as the matrix equation:

$$Q = \mathrm{N}\mathrm{Q}_0 \tag{2.60}$$

where

$$Q_0 \equiv \binom{u}{v}, Q \equiv \binom{U(z)}{V(z)}, \quad N \equiv \begin{pmatrix} U_2(z) & U_1(z) \\ V_2(z) & V_1(z) \end{pmatrix} \tag{2.61}$$

For our purposes we rewrite Equation 2.60 in the form

$$Q_0 = \mathrm{M}\mathrm{Q}, \tag{2.62}$$

where M, which is the inverse of N, turns out to be

$$M \equiv \begin{pmatrix} V_1(z) & -U_1(z) \\ -V_2(z) & U_2(z) \end{pmatrix} = \begin{pmatrix} m_{1,1} & m_{1,2} \\ m_{2,1} & m_{2,2} \end{pmatrix}. \tag{2.63}$$

Solving for the pair of boundary conditions $\{u = 0, v = 1\}$ and $\{u = 1, v = 0\}$, we get a solution

$$M = \begin{pmatrix} \cos(k_0 nz\cos\theta) & \frac{-i}{p}\sin(k_0 nz\cos\theta) \\ -ip\sin(k_0 nz\cos\theta) & \cos(k_0 nz\cos\theta) \end{pmatrix}. \tag{2.64}$$

For a series of adjacent homogeneous layers, we have

$$Q(z_0) = M_1(z_1 - z_0)M_2(z_2 - z_1)...M_N(z_N - z_{N-1})Q(z_N) = M(z_N - z_0)Q(z_N). \tag{2.65}$$

If the layers are sufficiently thin, i.e. $\delta z_j \equiv z_j - z_{j-1} << \lambda$, and we keep only first order terms, we get

$$M_j \approx \begin{pmatrix} 1 & -ik_0\frac{\delta z_j n_j}{p_j} \quad \cos\theta_j \\ -ik_0\delta z_j p_j n_j \quad \cos\theta_j & 1 \end{pmatrix}. \tag{2.66}$$

For N adjacent layers, this becomes

$$M \approx \begin{pmatrix} 1 & -ik_0\mathcal{B}(z_N - z_0) \\ -ik_0\mathcal{A}(z_N - z_0) & 1 \end{pmatrix}, \tag{2.67}$$

$$\mathcal{A}(z_N - z_0) = \sum_{j=1}^{N} \left(\mu_j - \frac{\alpha^2}{\epsilon_j}\right) \delta z_j, \tag{2.68}$$

$$\mathcal{B}(z_N - z_0) = \sum_{j=1}^{N} \epsilon_j \delta z_{j.} \tag{2.69}$$

Law and Beaglehole[11] found that one can find a solution which converges much more rapidly if instead of treating a profile as a series of layers of constant composition, one approximates it as a series of slabs wherein the dielectric $\epsilon_j(z) = \sqrt{n_j(z)}/\mu_j(z)$ varies linearly:

$$\epsilon_j(z) = a_j(z - z_j) + b_j, \tag{2.70}$$

where

$$a_j = \frac{\epsilon_j - \epsilon_{j-1}}{z_j - z_{j-1}}, \tag{2.71}$$

$$b_j = \frac{\epsilon_{j-1} z_j - \epsilon_j z_{j-1}}{z_j - z_{j-1}}, \tag{2.72}$$

and similarly for permeability. Turning the expressions for $\mathcal{A}$ and $\mathcal{B}$ into integrals, we get

$$M(z_N - z_0) = \prod_{j=1}^{N} M_j(z_j - z_{j-1}) = \prod_{j=1}^{N} \begin{pmatrix} 1 & -ik_0\mathcal{B}_j \\ -ik_0\mathcal{A}_j & 1 \end{pmatrix}, \tag{2.73}$$

$$\mathcal{A}_j = \left[\frac{a_j z^2}{2} + \left(b_j - \alpha^2\right)\right]_{z_{j-1}}^{z_j}, \tag{2.74}$$

$$\mathcal{B}_j = z_j - z_{j-1.} \tag{2.75}$$

For the solution for parallel polarized radiation, we make the replacements

$$\mathcal{A}_j = \left[z - \frac{\alpha^2}{a_j} \ln(a_j z + b_j)\right]_{z_{j-1}}^{z_j}, \tag{2.76}$$

$$\mathcal{B}_j = \left[\frac{a_j z^2}{2} - b_j z\right]_{z_{j-1}}^{z_j}. \tag{2.77}$$

In words, given electromagnetic radiation described by Q after having transversed a profile represented by the characteristic matrix M, one can use equation 2.62 to find the initial state Q_0. In many applications it would be the inverse of M that would be of interest in order to predict the final state of electromagnetic radiation incident in a medium in state Q_0. However, our objective is simply to find the reflection coefficients for both parallel and perpendicular polarized light.

Consider perpendicularly polarized light incident on an interface represented by a characteristic matrix M, wherein the interfacial profile extends form z_0 to z_n. We write down the general solutions for the electric field on either side of the profile:

$$\begin{aligned} \vec{E}_{\text{inc}}(z=z_0) &= \hat{x}\text{A}e^{i(k_0\alpha y-\omega t)}, \\ \vec{E}_{\text{ref}}(z=z_0) &= \hat{x}\text{R}e^{i(k_0\alpha y-\omega t)}, \\ \vec{E}_{\text{trans}}(z=z_n) &= \hat{x}\text{T}e^{i(k_0\alpha y-\omega t)} \end{aligned} \tag{2.78}$$

Given that Maxwell's equations require the tangential component of $\vec{E}$ be continuous across any boundary, the amplitudes of the $\vec{E}$ field on the incident and transmission sides can be written as:

$$\begin{aligned} A+R &= U(z_0) \\ T &= U(z_n), \end{aligned} \tag{2.79}$$

where A, R, and T are the incident, reflected, and transmitted amplitudes.

Given the relation between $\vec{E}$ and $\vec{H}$ for homogeneous media we find the y component of the $\vec{H}$ field

$$\vec{H} = \sqrt{\frac{\epsilon}{\mu}}\hat{k}\times\vec{E} \rightarrow H_y = \sqrt{\frac{\epsilon}{\mu}}\cos\theta E_x, \tag{2.80}$$

and as the tangential components of $\vec{H}$must also be continuous across any boundary, we can write for either side of the profile

$$\begin{aligned} H_y(z=z_0) &= p_i(A-R)e^{i(k_0\alpha y-\omega t)} \\ H_y(z=z_0) &= p_t\text{T}e^{i(k_0\alpha y-\omega t)}, \end{aligned} \tag{2.81}$$

where

$$p_i = \sqrt{\frac{\epsilon_i}{\mu_i}}\cos\theta_i, p_t = \sqrt{\frac{\epsilon_t}{\mu_t}}\cos\theta_t. \tag{2.82}$$

Using Equation 2.80 and Equation 2.82 with Equation 2.62 we get a pair of equations

$$A + R = (m_{1,1} + p_t m_{1,2})\, T, \tag{2.83}$$
$$p_i(A - R) = (m_{2,1} + p_t m_{2,2})\, T.$$

These can be solved for r_s:

$$r_s = \frac{R}{A} = \frac{(m_{1,1} + p_t m_{1,2})\, p_i - (m_{2,1} + p_t m_{2,2})}{(m_{1,1} + p_t m_{1,2})\, p_i + (m_{2,1} + p_t m_{2,2})}. \tag{2.84}$$

A similar procedure to the above is used to find r_p. The result is identical, except that p is replaced with q, where

$$q_i = \sqrt{\frac{\mu_i}{\epsilon_i}}\cos\theta_i, q_t = \sqrt{\frac{\mu_t}{\epsilon_t}}\cos\theta_t. \tag{2.85}$$

The values of r_s and r_p are now used to calculate $\bar{\rho}$, with $\theta_i = \theta_B$. As we are not in general dealing with a simple Fresnel interface one must find the Brewster angle through an iterative process, finding the angle for which the real part of r_p is minimized.

Ellipsometry is a very non evasive technique useful in a great variety of surface studies. While our work only made use of monochromatic ellipsometry, spectroscopic ellipsometry would be a very powerful tool indeed for studying phenomena related to what we investigate in this work. Where applicable, it is an excellent complement to the reflectometry techniques discussed in the previous section.

Bibliography

[1] L. G. Parratt, Phys. Rev., **95**, 359, (1954).

[2] M. Tolan, in *X-ray scattering from Soft-Matter Thin Films*, edited by G. Höhler (Springer-Verlag, New York, 1999), p. 5.

[3] P. Beckmann and A. Spizzichino, *The Scattering of Electromagnetic Waves From Rough Surfaces* (Pergamon, New York, 1963).

[4] L. Nevot and P. Croce, Revue de Physique applique'e, **15**, 761, (1980).

[5] D. S. Smith and B. M. Law, Phys. Rev. E, **54**, 2727, (1996).

[6] D. S. Smith, B. M. Law, M. Smock and D. P. Landau, Phys. Rev. E, **55**, 620, (1997).

[7] D. S. Smith and B. M. Law, Phys. Rev. E, **52**, 580, (1995).

[8] J. J. Cho, B. M. Law and K. Grey, J. Chem. Phys., **116**, 3058, (2002).

[9] D. S. Smith, Ph.D. thesis, Kansas State University, 1996.

[10] J. H. Carpenter, J. H. J. Cho and B. M. Law, Phys. Rev. E, **61**, 532, (2000).

[11] B. M. Law and D. Beaglehole, J. Phys. D (Great Britain), **14**, 115, (1981).

Chapter 3

Ultra-stable oven designed for x-ray reflectometry and ellipsometry studies of liquid surfaces

Reprinted with permission from M. Brown, S. Uran, B. Law, L. Marschand, L. Lurio, I. Kuzmenko and T. Gog, Review of Scientific Instruments **75**, 2536 (2004). Copyright 2004, American Institute of Physics.

3.1 Introduction

The physical properties of thin liquid films are important for many applications, i.e. lubrication, painting, coating and adhesion. Various studies of thin liquid films and interfaces over the last four decades have contributed significantly to our understanding of their structure.[1,2] One of the techniques commonly used for structural determinations is X-ray reflectivity.[3,4] This technique is sensitive to electron densities on thin (angstrom range) liquid films and has been extensively used to determine interfacial structures in liquids. Ellipsometry is another powerful reflectivity technique,[5,6] used frequently in film thickness determinations. It is a simple, quick, non-invasive tabletop technique with submonolayer sensitivity to thin films. There are various advantages to being able to do both ellipsometry and X-ray reflectometry on the same sample. First, ellipsometry can be used to characterize the stability and dynamics of a system in our laboratory; the understanding of which aids in the optimization

of time at a national X-ray facility where beam time is much more limited. Second, the techniques are complementary in that they are sensitive to differing length scales relevant to the systems under study, as described below. Additionally, if a model can be found that simultaneously describes the ellipsometric and x-ray reflectometry results then this agreement provides strong evidence that the experimental results are manifestations of the physical phenomenon of interest rather than a result of some experimental artifact. We are interested in using both ellipsometry and X-ray reflectometry to study the surfaces of liquid mixtures near a second-order phase transition, where even a small change in temperature can strongly influence both the thickness and structure of the interfacial region.[7] The need for precise temperature control makes such measurements challenging. Ideally the oven should be stable to 1mK per day with transverse temperature gradients within the oven less than 1mK/cm. Transverse temperature gradients induce convective motion within the liquid mixture which can perturb the interfacial structure. In a binary liquid mixture the surface composition varies as a function of depth z over length scales on the order of the correlation length ξ. For critical mixtures, the correlation length $\xi \approx t^{-0.63}$ is a divergent function of the reduced temperature $t = (T - T_c)/T_c$ relative to the mixtures critical temperature, T_c, and hence the interfacial structure is a sensitive function of t. This surface variation caused by the preferential adsorption of one of the components gives rise to a local volume fraction $v(z/\xi)$ which deviates from its bulk value $v(\infty)$ depending upon the dimensionless depth into the liquid. As mentioned above, the two experimental techniques measure different aspects of the local volume fraction because of differing sensitivities to the correlation length ξ.

In ellipsometry, the ellipticity $\overline{\rho} \equiv \mathrm{Im}(\frac{r_p}{r_s})$ at the Brewster angle is measured[8] where r_i is the complex reflection amplitude for polarization i. For thin films ($\xi/\lambda << 1$), the ellipticity $\overline{\rho}$ is related to the optical dielectric profile $\epsilon(z)$ at the surface via the Drude equation[9]

$$\overline{\rho} = \frac{\pi}{\lambda} \frac{\sqrt{\epsilon_1 + \epsilon_2}}{(\epsilon_1 - \epsilon_2)} \int_{-\infty}^{\infty} \frac{(\epsilon(z) - \epsilon_1)(\epsilon(z) - \epsilon_2)}{\epsilon(z)} dz \tag{3.1}$$

Here λ is the vacuum wavelength of light while $\epsilon(z)$ varies between its value in the incident ($\epsilon_1 = \epsilon(-\infty)$) and reflected ($\epsilon_2 = \epsilon(\infty)$) media. For thick films Eq. 3.1 is no longer valid and the ellipticity $\overline{\rho}$ must be determined by numerically solving Maxwells equations.[10,11] To determine the local volume fraction $v(z)$ from $\overline{\rho}$ one must relate $\epsilon(z)$ to $v(z)$. The usual assumption for AB mixtures is that these two quantities are related via the two component Clausius-Mossotti equation[12]

$$f(\epsilon(z)) = v(z)f(\epsilon_A) + (1 - v(z))f(\epsilon_B) \tag{3.2}$$

where

$$f(x) = (x - 1)/(x + 2) \tag{3.3}$$

and $epsilon_i$ is the optical dielectric constant of component i. Analogous considerations are also applicable for X-ray reflectometry. In the first Born approximation, valid at large scattering vectors q away from the critical scattering vector, x-ray reflectivity measures[3,4]

$$R(q) = R_F \left| \frac{1}{\rho(\infty)} \int \frac{d\rho(z)}{dz} e^{iqz} dz \right|^2 \tag{3.4}$$

in the absence of any surface roughness where $\rho(z)$ is the local electron density with bulk density $\rho(\infty)$ and $R_F \sim q^{-4}$ is the Fresnel reflectivity for an infinity sharp and unstructured interface. Alternatively, $R(q)$ can be determined by numerical solving Maxwells equation where these results are valid for all q. For X-ray reflectometry, $\rho(z)$ is assumed to be related to $v(z)$ via

$$\rho(z) = vz\rho_A + (1 - v(z))\rho_B \tag{3.5}$$

where ρ_i is the electron density for component i. Ellipsometry and x-ray reflectometry provide rather differing experimental measures of $v(z)$ as is evident from Eqs. 3.1 - 3.5. Hence, experimental measurements using these two techniques will highly constrain the functional form $v(z)$ that can describe both data sets.

3.2 Construction Details.

In order to build ovens possessing good temperature stability as well as small transverse temperature gradients, the ovens need to be designed symmetrically where cylindrical symmetry is usually the most convenient. Our oven and sample cell can therefore be viewed as three concentric cylinders: an inner passive glass sample cell together with an aluminum jacket, a middle actively controlled heater shell, and an outer water cooled shell. The disassembled components are shown in Fig. 1. On assembly the aluminum jacket is held concentrically about the sample cell via appropriately placed O-rings. The aluminum jacket, heater shell, and water shell are then held concentrically with respect to each other via nylon tipped set screws where a 1mm air gap separates the jacket, heater shell, and water shell, thus providing a weak thermal link. During assembly it is very important to maintain the cylindrical symmetry to high accuracy in order to minimize thermal instabilities and thermal gradients. The fully assembled oven of total length 10 inches and outer cylindrical diameter 4 inches is shown in Fig. 2. X-ray scattering and reflectivity measurements are made along the cylinder axis while ellipsometry measurements can be conducted through the semi-cylindrical glass windows. The Luer lock needle L1 has two purposes: (i) it enables one to replace air with helium gas, thus minimizing the build up of ozone gas and (ii) it acts as a fill port for the critical liquid mixture. Luer lock needle L2, which dips into the liquid sample trough, acted as a sample extraction needle. By over-pressurizing the oven via L1 using helium gas, a liquid sample can readily be extracted out of L2 for further testing. There are a number of important construction details that require more extensive description. The outer water cooled shell is double wrapped with copper tubing so that water enters and exits the tubing from the same side, as shown in Fig. 1. In this configuration the double wrapping ensures that the colder inlet water compensates for the hotter outlet water. Single wrapping of the copper tubing, with the water inlet and outlet on opposite ends of the cooler shell would, by contrast, induce a temperature gradient along the length of the cooler shell. In normal operation the cooler shell was maintained at $\sim 3^oC$ below the temperature of the heater

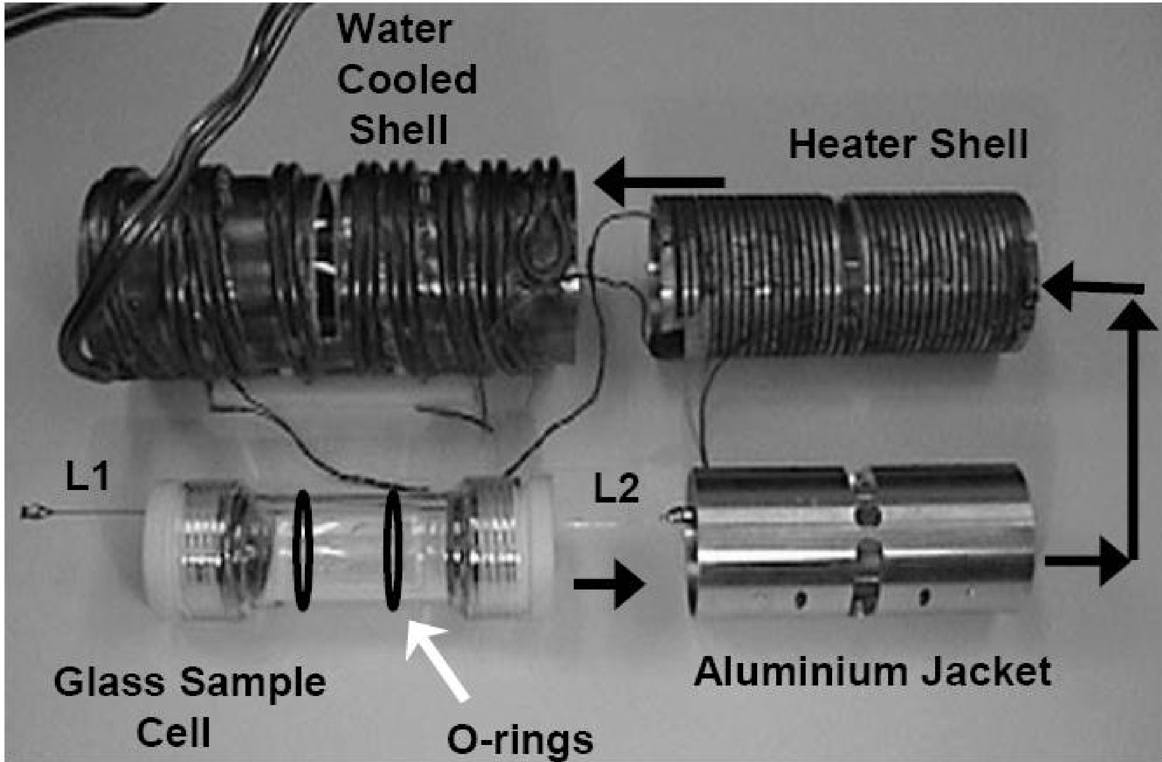

Figure 3.1: *Disassembled X-ray/ellipsometry oven components. The black arrows qualitatively indicate how the components are reassembled. L1 and L2 are, respectively, Luer lock fluid fill and extraction needles.*

shell using a water bath possessing a stability of $\sim 0.01^oC$.

The heater shell (Fig. 1) is constructed from aluminum and has very uniform machined grooves along its length. Laminated heating wire, possessing a resistance of $1.6\Omega/ft$ (Pelican Wire Co.), is permanently embedded in the grooves using the epoxy Wakefield Delta Bond 155. To minimize any temperature gradients it is important to ensure that the resistance of the heating wire is identical on the left and right halves of the heater oven before permanently embedding the wire in the grooves. Note that the use of heating wire provides more uniform heating than, for example, two Minco heaters placed symmetrically on the left and right halves of the oven because Minco heaters are only specified to be identical to within 10%. For optimal control and measurement of the temperature, the temperature sensing element must exhibit a large reproducible change in some physical property per ^oC, in the temperature

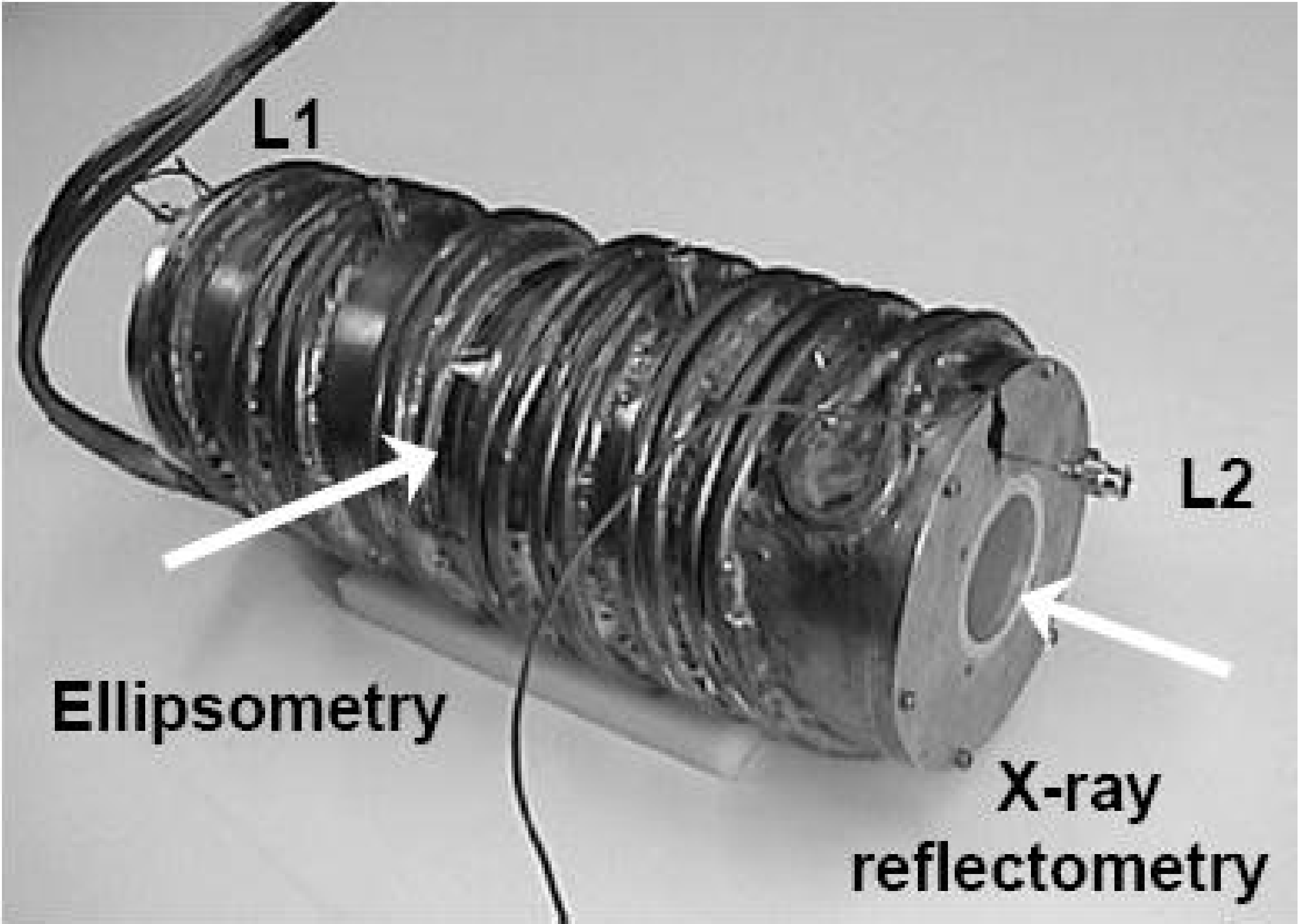

Figure 3.2: *Assembled X-ray/ellipsometry oven where the windows for x-ray and ellipsometry measurements are indicated by the white arrows.*

range of interest. Most of the critical mixtures that we study possess a critical temperature somewhere between 20^oC. In this range, thermistors possess an excellent sensitivity where the resistance decreases with increasing temperature and the temperature can readily be measured to sub-mK resolution. We use Yellow Springs Instrument 44034 thermistors as the sensing and measuring element where the nominal resistance at 25^oC is $5k\Omega$. They are extremely useful for measuring relative changes in the temperature in the vicinity of the critical temperature. Although these thermistors only have a nominal accuracy of 0.1^oC, thermistors possessing identical serial numbers exhibit much better thermal characteristics

than this. From a dozen thermistors (of identical serial number), one can usually find 3 or 4 matched pairs which exhibit identical readings in the vicinity of T_c to within a few mK. Such matched pairs are useful for accurately measuring temperature gradients as described later. One of these thermistors, immersed in thermally conducting paste (Omegatherm 201) within a 1.25 inch deep hole inside the heater shell, serves as the sensing element for a Lakeshore DRC-91C temperature controller.

Critical mixtures are very sensitive to the presence of impurities. Impurities on the order of a few percent can change the critical temperature by many degrees.[13] This change in T_c is not problematic, provided that T_c is stable and does not drift significantly with time. If the critical mixture reacts with any components of the sample cell T_c is likely to drift with time. From past experience we only trust a few materials to be in direct physical contact with our critical mixtures, specifically, certain glasses (pyrex, fused and crystalline quartz), teflon, teflon-encapsulated O-rings, and chemically resistant stainless steel (type 316). As a point of reference, for certain glass encapsulated critical mixtures such as isobutyric acid + water, T_c might drift at most a few mK/month. Our sample cell has therefore been constructed primarily from these materials where we have taken particular care about which materials come into direct contact with the critical mixture.

The glass sample cell (GC in Fig. 3a) is constructed from two threaded glass connectors (Ace Glass, Cat. No. 7644-25) where two teflon bushings (Ace Glass, Cat. No. 7506-35) hold two type 316 stainless steel end caps (SSC) in place with the sealing between the stainless steel and glass being accomplished using chemically resistant Kalrez O-rings.[14] The internal construction of the sample cell is shown in Fig. 3a together with the fill (L1) and extraction needles (L2). The end caps possess kapton windows through which x-rays can pass. A glass sample trough is situated inside a larger overflow teflon trough. Within the glass trough a glass slide is positioned approximately 0.5mm below the top edge of the glass trough using a U-shaped glass support (Fig. 3b). With the critical mixture heated well into the one-phase region (to prevent phase separation during filling), sufficient liquid is placed

into the glass trough such that it overflows this container and flows into the larger teflon trough. In this manner the liquid/vapor surface is configured to sit above the glass trough where the glass slide helps to minimize vibrational disturbances of this liquid/vapor surface. It is important to pre-align the glass trough horizontally because the x-rays are incident on the liquid/vapor surface near grazing incidence. To assist with this horizontal alignment the glass trough possesses an aluminum mirror on its bottom surface; horizontality is attained when a vertical laser beam is reflected back on itself from the mirrored bottom surface. The glass trough is readily cleaned using a glass etch solution (5% HF, 35% HNO3 and 60% H2O by volume), then rinsed well in ultra-clean water before drying. As ellipsometry is sensitive to any optical birefringence, it is important to anneal any glass windows through which the ellipsometric beam may pass. These components should also be held in a manner which minimizes mechanical stress to the glass. Transverse temperature gradients along the axis of the sample cell are measured using matched thermistors which are placed in good thermal contact with the stainless steel end caps using thermal paste. The temperature is measured to sub-mK accuracy via a simple voltage measurement series circuit (Fig. 4) incorporating an ultra-stable voltage source, LM399. The precision voltage reference LM399 is temperature compensated with less than 2 ppm drift per ^{o}C.[15] The Vishay Dale precision reference resistance R0 ($\sim 250k\Omega$) with a temperature coefficient of $50ppm/^{o}C$ limits the current through the thermistor to $\sim 20\mu A$ to minimize any Joule heating of the thermistor, which may perturb the temperature measurement itself.

3.3 Results and discussion

Fig. 5 shows typical long time scale temperature and temperature gradient data where the temperature was changed by $0.15^{o}C$ at time $\tau = 0s$. From Fig. 5a, one observes that after 3.5 hours the system has reached its final equilibrium temperature and is stable to within $\sim 0.5mK$ over many hours. Fig. 5b depicts temperature gradient data collected using matched thermistors where one observes that the temperature gradient holds steady

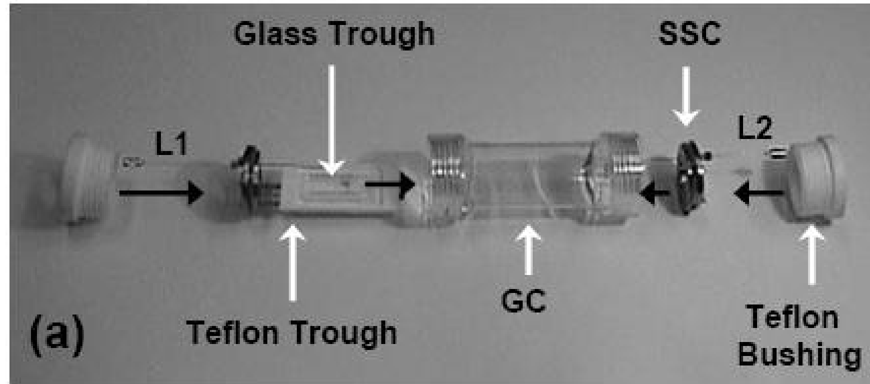

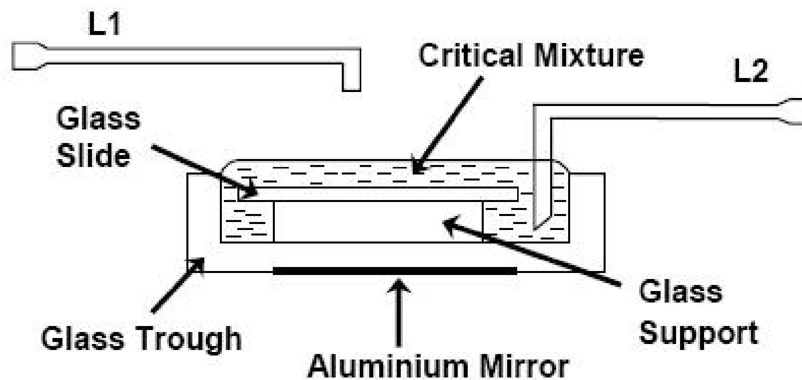

Figure 3.3: *(a) Disassembled sample cell showing the glass and teflon troughs, fill (L1) and extraction (L2) Luer lock needles, glass cell (GC), stainless steel cap (SSC), and teflon bushings. The black arrows qualitatively indicate how the components are reassembled. (b) Schematic cross-section of critical mixture in the glass trough.*

at less than $0.5mK/cm$ over the measurement period. In our first experimental test of this oven, we have studied the liquid/vapor surface of the non-polar critical liquid mixture 1,1,2,2-tetrabromoethane + n-dodecane in the one-phase region ($T > T_c$). This mixture possesses both good x-ray and ellipsometric contrast. The ellipsometric results were collected with the glass slide and glass support removed from the glass trough (to minimize any optical interference) where the results (solid squares, Fig. 6a) are compared with earlier measurements (open circles, from Ref. 16). Good agreement is found between these two

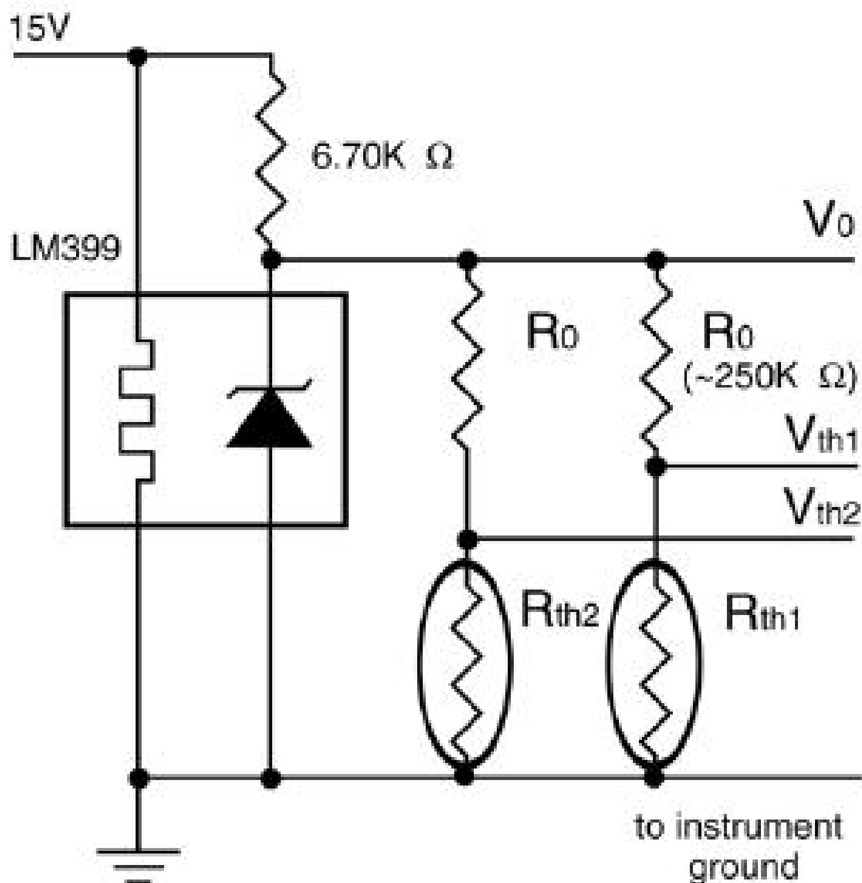

Figure 3.4: *Series circuit for accurately measuring temperatures and temperature gradients. The thermistor resistances (R_{th1}, R_{th2}) are determined by accurately measuring the voltages V_0, V_{th1} and V_{th2} and then converting these resistances to temperatures using the associated thermistor calibration table.*

ellipsometric measurements. X-ray reflectivity (Fig. 6b) and off-specular measurements (not shown) were also collected from the liquid/vapor surface of this same stock critical mixture using beamline 9-ID (CMC-CAT) at the Advanced Photon Source located at Argonne National Laboratory. A few mL of the critical mixture overfilled the glass trough. At each temperature, the system was equilibrated for approximately 4 hours to ensure thermal and diffusive equilibrium where the x-ray data took an additional 2 hours to collect. To prevent the slow degradation of this critical mixture by X-rays, a few additional mL of the

mixture were added at the end of each X-ray run. The ellipsometric and x-ray data in Fig. 6, demonstrate an interesting fact that was not obvious to us before the measurements. For critical adsorption ellipsometry and x-ray reflectometry are most useful in complementary temperature regimes; ellipsometry exhibits the greatest changes in $\overline{\rho}$ close to T_c for reduced temperatures $t < 10^{-2}$ (i.e. $T - T_c \leq 3^oC$) whereas, by contrast, x-ray reflectometry exhibits the greatest changes far from T_c for $25^oC \leq T - T_c \leq 5^oC$. (In Fig. 6b the $\Delta T = T - T_c = 1^oC$ and 5^0C data are almost identical, whereas, there are large differences between the 5, 15 and 25^oC data.) Complementary ellipsometric and x-ray reflectometry measurements from the same sample are therefore extremely useful in trying to deduce a local volume fraction $v(z/xi)$ which can describe both data sets. A coherent interpretation of these experimental results is still under consideration. Finally we should mention an unexpected problem which arose during the x-ray experiment due to the sample cell design. It was found that at higher temperatures gas bubbles were emitted into the liquid sample from the extraction needle (L2) due to differences in air pressure between the needle and the remainder of the sample chamber. This unintentional problem was overcome by equalizing the pressure via an external tube between L1 and L2. We did not notice any temperature stability or temperature gradient problems with this tube in place.

In summary we have described the construction of an accurate x-ray and ellipsometry oven which is stable to $\sim 1mK/day$ and possesses transverse temperature gradients of less than 1mK/cm. This oven is useful for studying the surface of critical liquid mixtures where accurate temperature control is a prerequisite. The oven can also be used to study adsorption at, for example, the Si wafer/gas interface with the insertion of a Si wafer in place of the glass trough. Neutron reflectometry from the surfaces of these systems can also be undertaken within this oven by replacing the kapton windows with fused quartz windows.

This work was supported by DOE under grant number DE-FG03-02ER46020 and NSF under grant number DMR-0097119. Work at the CMC Beamlines is supported in part by the Office of Basic Energy Sciences of the U.S. Dept. of Energy and by the National

Science Foundation Division of Materials Research. Use of the Advanced Photon Source is supported by the Office of Basic Energy Sciences of the U.S. Department of Energy under Contract No. W-31-109-Eng-38.

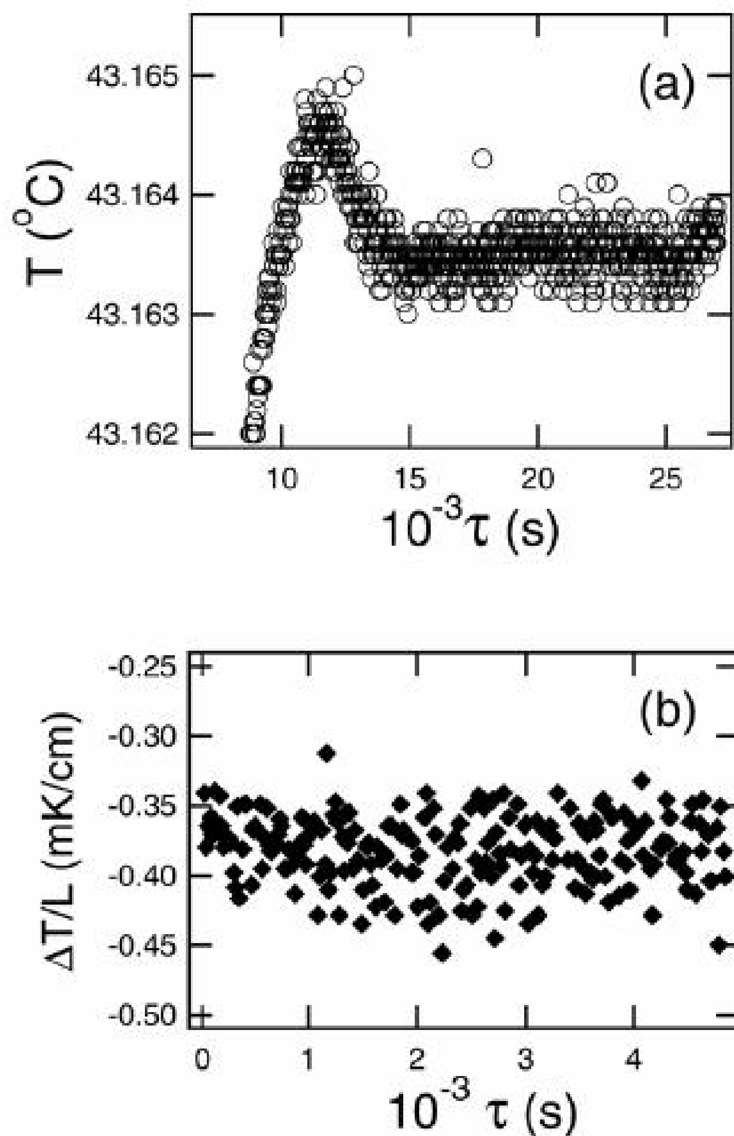

Figure 3.5: *(a) Variation in temperature after a temperature jump of* 0.15^oC *at time* $\tau = 0s$*. The oven has reached its final equilibrium temperature after 3.5 hours and is stable to 0.5mK over many hours. (b) Representative temperature gradient data measured using matched thermistors at either end of the sample cell.*

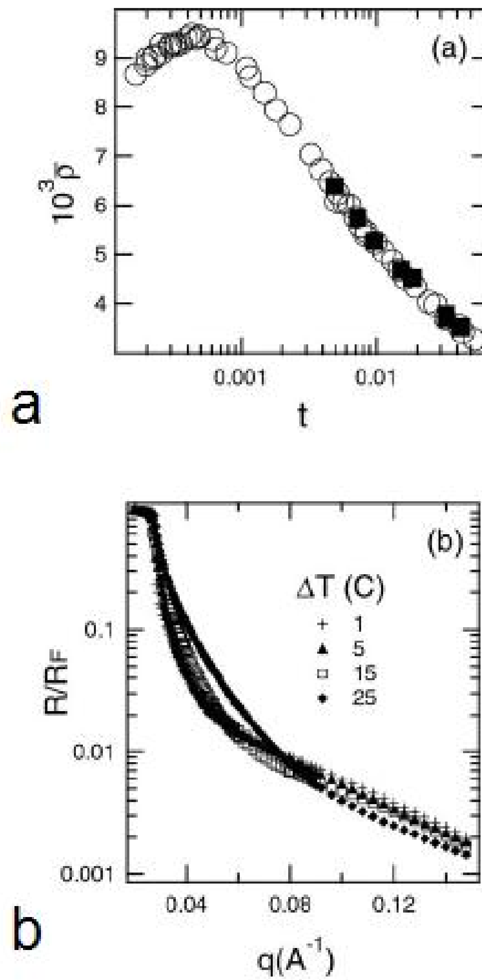

Figure 6, Matthew D Brown, Review of Scientific Instruments.

Figure 3.6: *Experimental measurements from the liquid/vapor surface of the critical mixture 1,1,2,2-tetrabromoethane + n-dodecane. (a) Ellipticity $\overline{\rho}$ versus reduced temperature t where the current measurements (solid squares) are compared with prior measurements (open circles, Ref.[16]). (b) Normalized X-ray reflectivity $R(q)/R_F$ versus scattering vector q at various temperature differences $\Delta T = T - T_c$.*

Bibliography

[1] A. W. Adamson, “Physical Chemistry of Surfaces“, 4th ed. (Wiley, New York, 1982).

[2] Fluid Interfacial Phenomena, C. A. Croxton (ed.), (Wiley, New York, 1986).

[3] P. S. Pershan and J. Als-Nielsen, Phys. Rev. Lett. **52**, 759 (1984)..

[4] M. Tolan, X-ray scattering from soft-matter thin films, Springer Tracts in Modern Physics, Vol. 148 (Springer, Berlin, 1999).

[5] R. M. A. Azzam and N. M. Bashara, Ellipsometry and Polarized Light (Elsevier, Amsterdam, 1987).

[6] See D. Beaglehole in Ref. [2].

[7] B. M. Law, Prog. Surf. Sci. **66**, 159 (2001).

[8] D. Beaglehole, Physica **100B**, 163 (1980).

[9] P. Drude, The Theory of Optics (Dover, New York, 1959).

[10] M. Born and E. Wolf, Principles of Optics 6th ed. (Pergamon, Oxford, 1980).

[11] B. M. Law and D. Beaglehole, J. Phys. D **14**, 115 (1981).

[12] R. F. Kayser, Phys. Rev. B 34, 3254 (1986).

[13] J. L. Tveekrem and D. T. Jacobs, Phys. Rev. A 27, 2773 (1983).

[14] It should be noted that after the X-ray experiment the chemically resistant Kalrez O-rings had swollen considerably and perhaps teflon-encapsulated O-rings would be a better choice in future.

[15] Linear Applications Handbook, (National Semiconductor Corp., Santa Clara, 1986).

[16] J.-H. J. Cho, B. M. Law, and K. Gray, J. Chem. Phys. **116**, 3058 (2002).

Chapter 4

X-ray Specular Reflectivity Study of a Critical Binary Fluid Mixture

Reprinted article with permission from L. W. Marschand, M. Brown, L. B. Lurio, B. M. Law, S. Uran, I. Kuzmenko and T. Gog, Physical Review E **72**, 011509 (2005).

At the liquid-vapor interface of a binary fluid mixture, the component with the lowest surface tension will segregate to the surface even above the temperatures where the two fluids are mixed in the bulk. With increasing depth, z, into the fluid, the composition returns to its bulk value. Near the critical point, the length scale over which the composition returns to its equilibrium value will be determined by the bulk-fluid correlation length $\xi = \xi_0 t^{-\nu}$ with ξ_0 a correlation length amplitude, $t = (T - T_c)/T_c$, and ν a critical exponent. For systems in the 3-D Ising universality class it is expected that $\nu \approx 0.632$.

Based on the predictions of Fisher and de Gennes[1], very close to the critical point, and in the limit of a sufficiently strong and short range surface field, h_1, the profile should have a universal scaling form given by:

$$m(x) = Mt^{\beta}P(x). \tag{4.1}$$

Here the order parameter, m is related to the volume fraction of the surface segregating component via $m = \Phi(z) - \Phi(\infty)$ and Mt^{β} describes the shape of the coexistence curve for the specific binary fluid mixture. The depth into the fluid is given as a function of

dimensionless coordinates $x = (z + z_e)/\xi$ where z_e is a system dependent offset value. The critical exponent β is expected to have the value of about 0.328.

Based on simple scaling arguments, the limiting forms of the universal function, P, for small and large x are expected to be

$$\begin{aligned} P(x) &\to P_0 x^{-\beta/\nu} \text{ for } \; x \to 0 \\ P(x) &\to P_\infty e^{-x} \text{ for } \; x \to \infty \end{aligned} \tag{4.2}$$

where the small and large x behavior originate from, respectively, Fisher and de Gennes[1] and Liu and Fisher[2]. The theoretical predictions of Fisher and de Gennes have been subsequently refined by Monte-Carlo[3], Renormalization Group[4] and an interpolation scheme[5], which gave rise to values of 0.866, 0.717 and 0.94 ± 0.05, respectively for P_0 and 1.5 and 1.621, respectively for P_∞ (the interpolation scheme did not provide a prediction for P_∞). There have also been a number of experimental tests. Light reflection measurements probe integrals over the critical adsorption profile, and are mainly sensitive to the temperature dependence of scaling variables. Schlossman *et. al.* used optical reflectivity to confirm the asymptotic behavior predicted in Eq. 2[6]. A summary of ellipsometry studies, which measures the optical reflectance at the Brewster angle, has been published by Carpenter *et. al.*[7]. These authors find they can describe a wide range of results using a model denoted $P1$, which uses asymptotic limits for the scaling function up to second order in an expansion in the large x and small x regions where x is the dimensionless parameter defined above[8]. These limits are matched at a crossover point, x_0 (the only freely adjustable parameter) up to their first derivative in x. They were able to fit ellipsometry data from five different critical binary fluids using values of $P_0 = 0.788$, $P_\infty = 0.963$ and $x_0 = 1.15$[7,9]. Direct tests of the shape of the profile have been made via neutron scattering measurements[10–12]. Howse *et. al.* studied a system of 2-butoxyethanol+deuterium oxide. The neutron scattering data were well described by a model using a power law profile for small x with an exponent of 0.52±0.02. This is within errors of the predicted value of $\beta/\nu = 0.516$. They found $P_0 = 0.11$; significantly smaller than the expected value from Monte Carlo calculations of 0.866[3].

Zhao *et. al.* studied methanol + deuterated cyclohexane. Their neutron measurements could be fit with a scaling form proposed by Liu and Fisher:

$$P(x) = P_0 \left[(1 + cx)/x\right]^{\beta/\nu} \exp(-x). \tag{4.3}$$

The parameters β/ν and P_0 were coupled in the fits. If they fixed $P_0 = 1$ then $\beta/\nu = 0.50 \pm .05$, while for β/ν fixed to its theoretical value, $P_0 = 0.34$. Jestin *et. al.* looked at n-hexane + perfluorohexane and methanol + cyclohexane with either of the two components deuterated. They obtained good neutron reflectivity fits with the Liu Fisher form. The methanol + cyclohexane mixtures gave values of P_0 close to the predicted 0.866, but β/ν were 5 to 10% smaller than theory. For n-hexane + perfluorohexane they obtained $P_0 = 1.78$ which is much larger than theory. They hypothesize that this large value of P_0 may indicate a different profile shape for the case of a large surface tension difference between the components.

All of the neutron scattering measurements, to date, have been limited to small wavevector transfer, defined by $Q = 4\pi \sin(\theta)/\lambda$, with θ the incident angle. In the present measurement we have carried out an x-ray specular reflectivity measurement with high angular resolution, and out to large $Q_{\max} = 2.3\text{nm}^{-1}$. This provides sensitivity to features at the molecular length scale such as the formation of a surface monolayer.

In the Born approximation, the intensity of x-ray reflection vs. angle can be related to the absolute magnitude of the Fourier transform of the scattering length density.

$$R(Q)/R_F(Q) = \left| \frac{1}{\rho(\infty)} \int_{-\infty}^{\infty} e^{iQz} \frac{d\rho(z)}{dz} dz \right|^2 \tag{4.4}$$

Here ρ is the x-ray scattering length density, $R(Q)$ is the measured reflectivity and $R_F(Q)$ is the ideal Fresnel reflectivity for a perfectly sharp interface.

When multiple scattering cannot be ignored, the reflectivity can be approximated by the Parratt[13] method, in which Maxwell's equations are solved for a system of uniform density slabs that approximate the profile. In neither case can the x-ray scattering data be directly

inverted, without further assumptions, since the phase of the reverse Fourier transform is not available. Techniques have been developed, however, that allow the phase to be recovered through the imposition of physical constraints on the possible profiles. These have been recently reviewed by Tolan[14]. We have applied the technique outlined by Sanyal *et. al.*[15] to the present data.

4.1 Reflectivity Experiment

The sample cell was a Pyrex tray inside a two-staged oven[16]. It was horizontally mounted and fitted with 25μm thick Kapton windows. The temperature could be held uniform over the chamber to $\pm$ 1 mK. The sample was a mixture of n-dodecane (Fluka 98+% purity) and 1,1,2,2-tetrabromoethane (Aldrich 99+% purity). The chemicals were used as received from the supplier. This mixture yields excellent x-ray contrast, and has previously been studied via ellipsometry[9]. Both components are non-polar which excludes surface orientational ordering effects[17]. This mixture was prepared to within 1% of its critical composition (45% by volume of dodecane). The sample environment was saturated with the equilibrium vapor of the mixture. In order to minimize vibration, the sample was a thin layer ($<$ 1.5mm) of fluid on top of a flat rectangular 19mm by 45mm glass slide. The sample was surrounded by a 7 mm deep trough filled with the mixture, but the mixture did not contact the windows, thus avoiding problems associated with a meniscus. Due to poor convective mixing in the thin layer, it was necessary to maintain the sample always above its critical temperature of $T_c = 37.5$C, since, should phase separation occur, the mixture could not be remixed *in-situ*. The accumulation of x-ray damage to the sample was prevented by topping the sample cell with fresh mixture after every change in temperature. Reflectivity data were taken from +1C to +30C above T_c. Between measurements the cell was allowed to equilibrate for 2 to 4 hrs until no gradients larger than 1 mK/cm remained. Measurements were performed at CMC-CAT at the Advanced Photon Source. The measured x-ray reflectivity, normalized to the Fresnel reflectivity $R_F(Q)$ for the bulk mixture, is displayed vs. Q, in Fig. 4.1. Just

above the critical angle ($Q_c = 0.277$ nm^{-1}) the reflectivity goes below the Fresnel reflectivity. The Q range of the falloff broadens with increasing temperature. There is also a peak in the scattering between 1 and 2 nm^{-1}.

The reflectivity was compared to the $P1$ model of Carpenter *et. al.* by converting their profile to an electron scattering length profile. This was divided into ∼1000 slabs and the reflectivity was calculated using the Parratt method. This method is discussed in detail by Tolan[14] and Daillant[18]. The model reflectivity did not agree with the measured data. Varying the parameters of the model, (P_0, P_∞ and x_0) did not improve the fits enough to provide a good match to the data because of the peak at ~ 1 nm^{-1}.

In order to obtain a composition profile which could describe the data, the x-ray data was inverted using the phase guessing algorithm described by Sanyal *et. al.*[15]. The basis of this method is to calculate an estimate of the density profile from a reverse transform of the measured scattering. A guess is made for the phase of the transform based on a model profile. For the present study, the initial phase guess was obtained from the $P1$ model, using the Parratt method described above to calculate the model reflectivity. This model profile is iterated, until the reverse transform is consistent with the initial model. Note that while a reverse Fourier transform is used to calculate the phases in this method, the actual reflectivity is calculated from the density profile using the Parratt formalism, which fully accounts for multiple scattering.

Explicitly, the $(m+1)$ iteration of the density profile was calculated via:

$$\begin{aligned} \frac{d\rho_{m+1}(z)}{dz} = \frac{1}{2\pi} \int \int_{-\infty}^{\infty} & \exp\left[iQ\left(z - z'\right)\right] \\ & \sqrt{\frac{R_{ex}(Q)}{R_m(Q)}} \left(\frac{d\rho_m(z')}{dz'}\right) dz' dQ \end{aligned} \tag{4.5}$$

The subscripts m and ex indicate the model and experimental parameters, respectively. The resulting $d\rho(z)/dz$ was modified by subjecting it to physical constraints and the procedure was iterated. We imposed two physical constraints on the fitting inversion process. The

first consisted of the imposition that the liquid-vapor interface be reasonably sharp, which was accomplished by setting the profile to zero for $z < -2$ nm. The second constraint was imposing a monotonically increasing tetrabromoethane concentration from the surface to the bulk, by taking $\rho(z) \rightarrow |\rho(z)|$. This second constraint is physically reasonable, since the dodecane has a much lower surface tension and would be expected to dominate the liquid-vapor interface, and since all present theoretical predictions for the profile are monotonic. It should be recognized that this inversion procedure might exclude other possible inversions of the scattering data, which would involve oscillations in the dodecane concentration near the surface. In order to avoid truncation artifacts the reflectivity curve was extrapolated to larger Q by matching a Gaussian tail to the data. Finally, a small ($\sim 10^{-7}$rads) angular offset was applied to the data so that the critical angle of the simulated density profile would be equal to that of the critical mixture. Such an offset is entirely consistent with this type of experimental setup. This algorithm was iterated until it converged on a profile, typically requiring 20 to 100 iterations. The fits are shown as the solid lines in Fig. 4.1. The uniqueness of the inversion was tested by starting with different initial phase guesses. Both the initial parameter values of Carpenter *et. al.* and the best fit values of these parameters to the x-ray data, yield nearly identical final profiles.

Comparisons were made with the ellipsometry results of Carpenter *et. al.*[7], by extracting the optical index of refraction from resulting composition profiles, and simulating the coefficient of ellipticity as defined by $\overline{\rho} = \text{Im}(r_p/r_s)|_{\theta_B}$ as a function of temperature. This procedure is describe in detail elsewhere[7]. This comparison is displayed in Fig.4.2 . The x-ray profiles give a reasonable correspondence with the measured temperature dependence of $\overline{\rho}$, however the ellipticity coefficients are offset in the positive direction by 2-4 units. We do not presently understand the basis of this offset, although it may be related to differences in the the length scale of in-plane surface roughness that is averaged over by each technique. The surface roughness or the thickness of the liquid/vapor interface can shift the ellipticity values. Up to this point we have not considered the effect of surface roughness on the profile

at the liquid-vapor interface. Capillary waves will roughen the interface and the measured interfacial profile will be a convolution of the intrinsic profile and the surface roughness[19]. The magnitude of the root-mean-square surface height deviations resulting from capillary waves will depend on the area of surface averaged over by the scattering probe, and is typically in the range of 0.3 to 0.7 nm for simple liquids. This roughness will have the effect of rounding out any features on the experimentally measured density profiles. Since ellipsometry and x-ray measurements may average over different surface areas, they may see different effective interface profiles. The liquid-vapor surface tension remains relatively constant over the range of temperatures measured, so the surface roughness will not show critical scaling and any systematic difference between the ellipsometry and x-ray results would most likely show up as a constant offset. Such an effect may account for part of the shift of the ellipsometry results relative to the x-ray results which we observed. However, we have calculated that the deconvolution of the expected interfacial roughness from our measured experimental profiles would only shift the ellipticity factor by around half of the measured difference. Another possible source of the shift could be molecular polarization effects at the surface.

4.2 Summary of Results

The extracted volume fraction of dodecane as a function of depth into the fluid are shown vs. t in Fig. 4.3. An unexpected feature of the profiles is an approximately monolayer wide surface layer saturated with dodecane, followed by an abrupt falloff to approximately 83% dodecane. The rounding of the profile in the region of the monolayer probably results from capillary wave roughness, which cannot be separated from the intrinsic profile. A central prediction of surface critical theory is that the surface composition profile should scale with the bulk correlation length ξ. In order to test this we have scaled the data sets measured at +2C, +3C, +5C, +15C, +20C +25C and +30C to the data taken at +1C. This was done in the following manner: the amplitudes of all the volume fraction profiles were divided by

t^β according to Eq. 1. The value of β was taken as the Ising value of 0.328. The lowest temperature data set (+1C) was then taken as a reference. The volume fraction function for this set was converted to a P function according to Eq. 1 with $\xi_0 = 0.29$ nm[7] and $z_e = 0$ for the +1C data. The higher T data sets were fit to this set by rescaling them according to $P(x) \equiv P[(z + z_e)/\xi]$ with ξ and z_e adjustable parameters. The first 1 nm of each set was excluded from the scaling, since the region near the monolayer should not be expected to scale. The scaled data are plotted in Fig.4.4. The scaling gives a reasonable, but not perfect overlap of the data. The error bar on the best fit dotted line represents the standard deviation of the values for z_e/ξ.

In the inset to Fig. 4.4 the scaling ratio (ξ/ξ_0) obtained from the fits is plotted vs. reduced temperature. Since the scale factor of the +1C data was fixed there is no error bar on that point.

In Fig. 4.4 we have compared the scaled $P(x)$ functions with various predictions. The $P1$ model of Carpenter *et. al.* does not match the scaled data using Carpenter's parameters, although excellent agreement can be obtained if one takes $P_0 = 1.87$, $P_\infty = 1.98$ and $x_0 = 0.96$ (dotted line). Very good agreement is also found with the Liu and Fisher model for the parameters found by Jestin *et. al.* for n-hexane + perfluorohexane.

The scaling represented in Fig. 4.4 assumes an Ising exponent for β, however it is also of interest to see how well the data scales using a mean field value of $\beta = 0.5$. In Fig. 4.5 the data were scaled using this value of β and with ξ and z_e adjustable parameters as before. The values of ξ extracted from these fits are shown in the inset to the figure, and compared with the mean field prediction for the exponent $\nu = 0.5$. This exponent also provides a reasonable description of the t dependence. The data are compared with the predicted mean field form for $P(x) = \sinh(x)$[4]. The mean field functional form does not provide as good a fit to the mean field scaled data as the $P1$ model provided for the Ising scaled data. It is, however, still consistent with the experimental uncertainty in the data, chiefly due to the variation in z_e. The present results differ from previous work

in that the composition profiles show a well defined peak corresponding to a monolayer of pure dodecane saturating the surface. There is a subsequent abrupt fall-off from the this saturated monolayer, to a mixed second layer with $\Phi_{\text{dodecane}} \approx 0.83$. It is not surprising that this monolayer has not been seen before, since no previous probes had comparable spatial resolution. The monolayer thickness, and the magnitude of the discontinuity in composition appears independent of t.

This effect will clearly cause scaling to fail within the first nm of the fluid. We cannot exclude the possibility that this monolayer is due to impurities of shorter alkane chains. The larger z portions of the curves do appear to scale, with a form close to an Ising model with $P_0 = 1.87$, $P_\infty = 1.98$ and $x_0 = 0.96$.

This work was supported by DOE grant DE-FG03-20ER46020. The Advanced Photon Source is supported by DOE grant W-31-109-Eng-38.

Readers may view, browse, and/or download material for temporary copying purposes only, provided these uses are for noncommercial personal purposes. Except as provided by law,this material may not be further reproduced, distributed, transmitted, modified, adapted, performed, displayed, published, or sold in whole or part, without prior written permission from the American Physical Society.

http://link.aps.org/abstract/PRE/v72/e011509

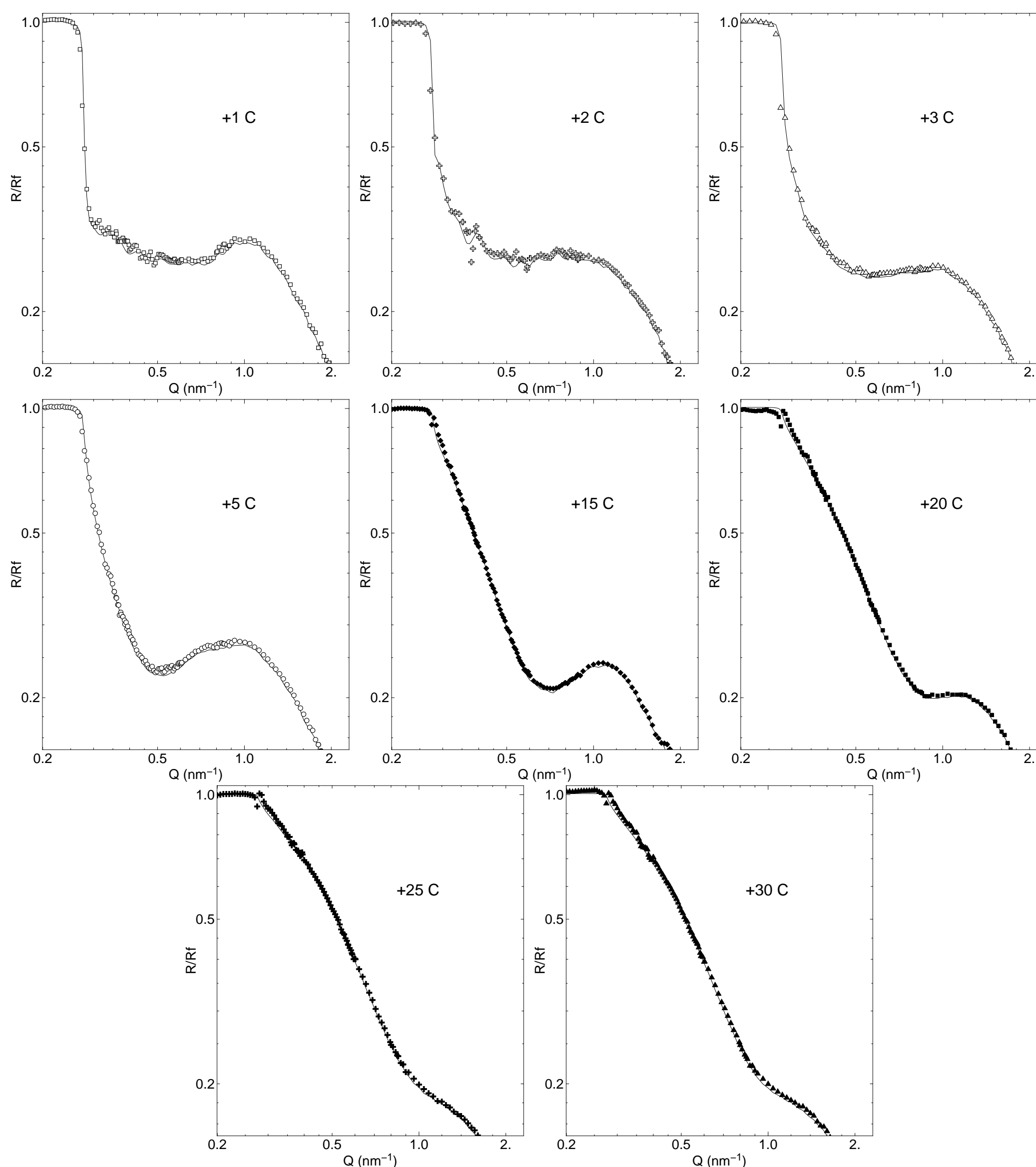

Figure 4.1: *X-ray reflectivity R/R_F from a mixture of dodecane and tetrabromoethane vs Q. The data are normalized by the Fresnel reflectivity for the bulk. The temperatures, relative to T_C are: +1C, +2C, +3C, +5C, +15C, +20C, +25C, +30C. The solid lines are the fits described in the text.*

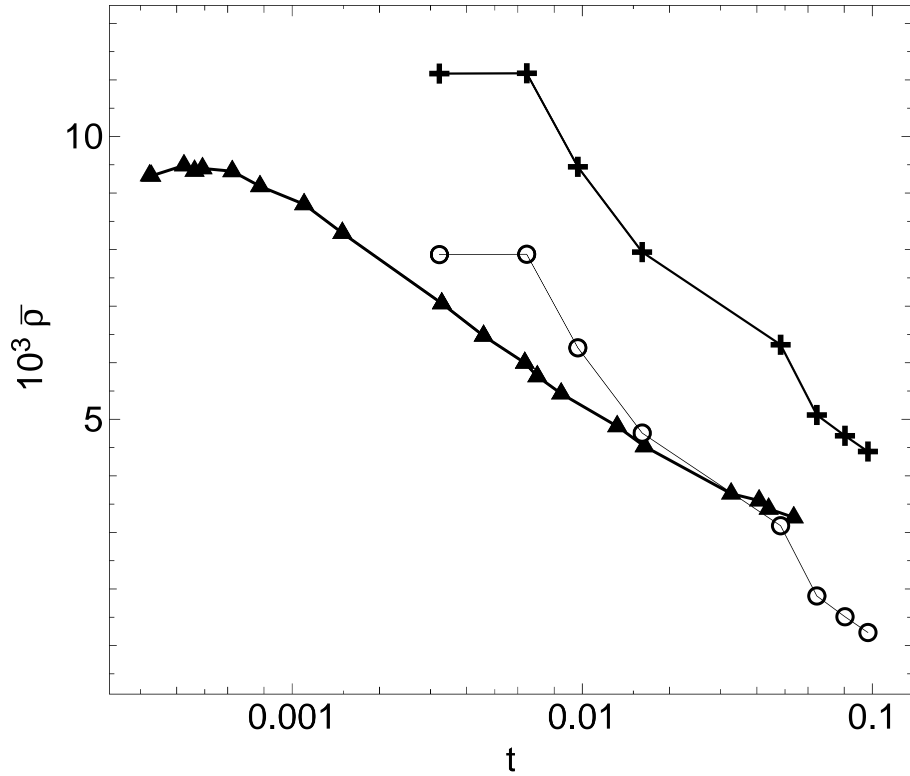

Figure 4.2: *Comparison of ellipsometry and simulated ellipsometry extracted from best fit x-ray density profiles as a function of t. Ellipsometry (triangles), x-ray profiles (crosses), x-ray profile with offset of -3.2 (open circles).*

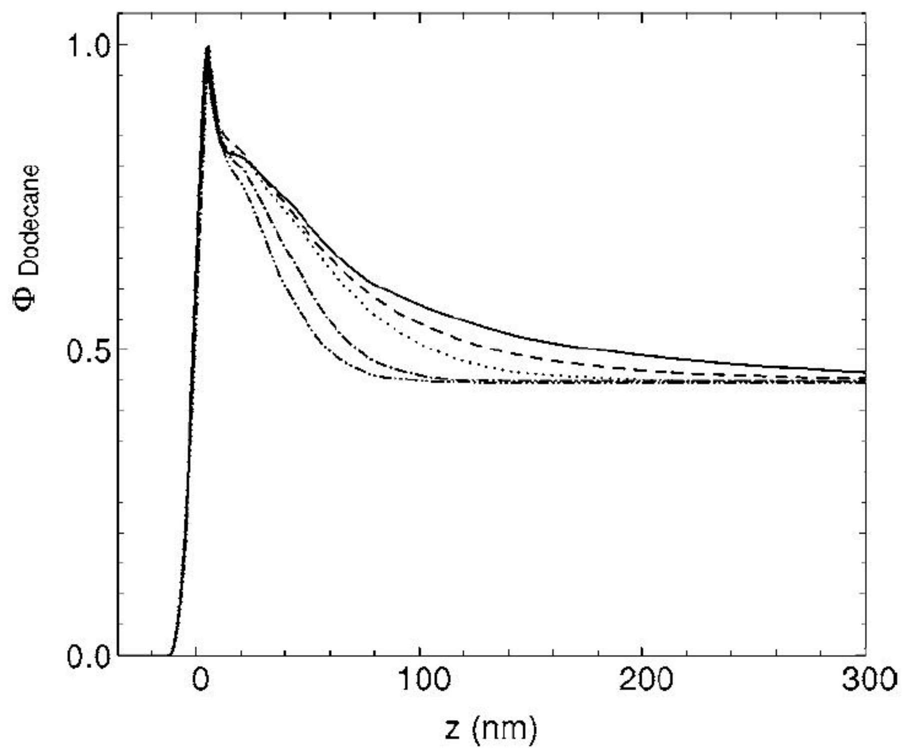

Figure 4.3: *Volume fraction profiles for dodecane as extracted from the x-ray reflectivity at +1C (t=0.0032) (solid line) +3C (t=0.0097) (dash line) +5C (t=0.016) (dot line) +15C (t=0.048) (dot-dash line) and +20C (t=0.064) (dot-dot-dash line).*

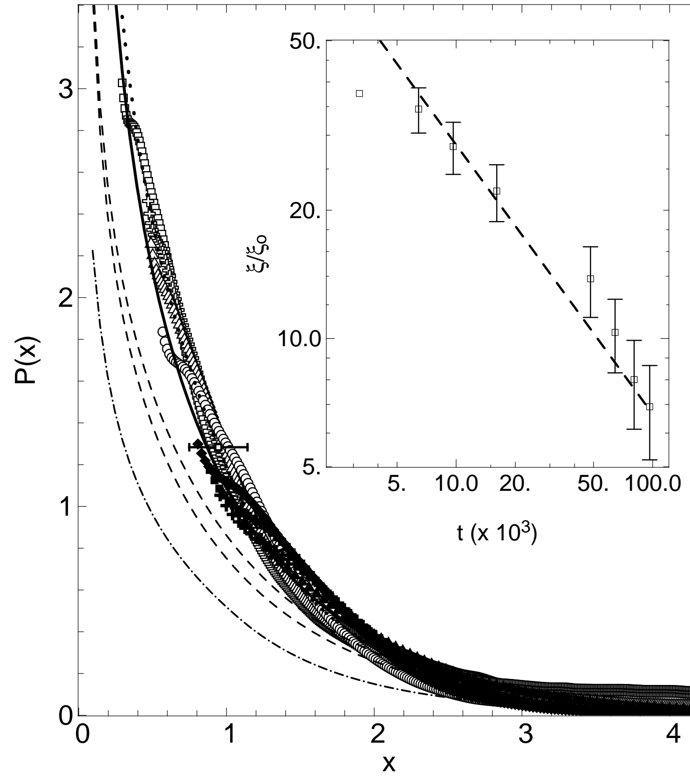

Figure 4.4: *Comparison of scaled volume fraction data. Experimental data (symbols) with temperatures as in Fig. 1. The dotted line is the best fit to the scaled data using the $P1$ model of Carpenter et.al. with $P_0 = 1.87$, $P_\infty = 1.98$ and $x_0 = 0.96$. The solid line is the model of Liu and Fisher with the parameters obtained by Jestin et.al. for the mixture of n-hexane + perfluorohexane. The dashed lines are the Liu and Fisher model parameters obtained by Jestin et.al. for the two methanol + cyclohexane mixtures. The dot-dashed line is the $P1$ model with parameters obtained by Carpenter et.al. The single error bar is the standard deviation of the fitted values for z_e/ξ along the x axis. The inset shows the best fit value of the scaling ratio ξ/ξ_0. This is shown plotted against the Ising model value of* 0.63 *(dashed line).*

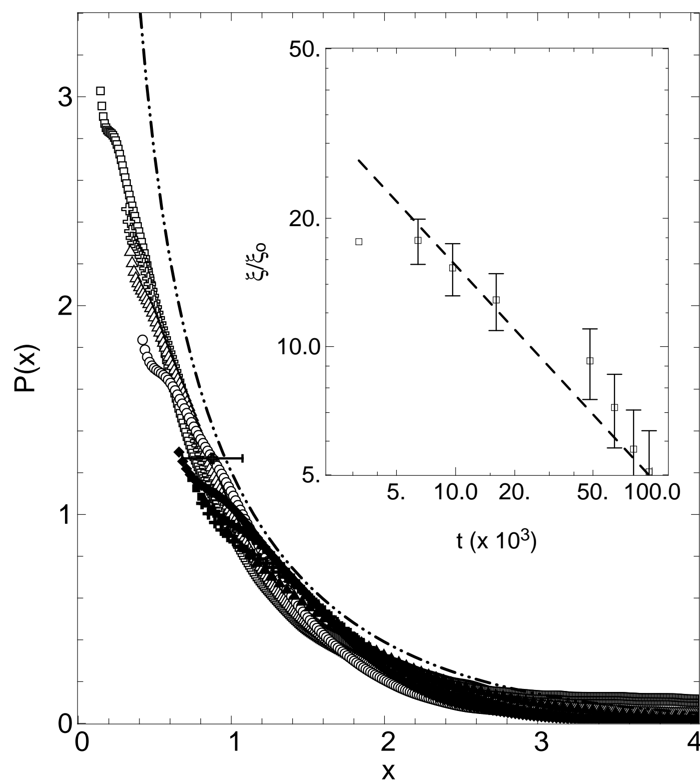

Figure 4.5: *Comparison of scaled volume fraction data. Experimental data (symbols) with temperatures as in Fig. 1 is compared against mean field theory (dot-dot-dashed line). The inset shows the best fit value of the scaling ratio ξ/ξ_0. This is shown plotted against the mean field model value of* 0.50 *(dashed line).*

Bibliography

[1] M. E. Fisher, P.-G. de Gennes, *Cr. Acad. B.* **287**, 207 (1978).

[2] A. J. Liu, M. E. Fisher, *Phys. Rev. A* **40**, 7202 (1989).

[3] M. Smock, H. W. Diehl, D. P. Landau, *Ber. Bunsenges. Phys. Chem.* **98**, 486 (1994).

[4] H. W. Diehl, M. Smock, *Phys. Rev. B* **47**, 5841 (1993).

[5] S. Floeter, G. Dietrich, *Phys. B: Condens. Matter* **97**, 213 (1995).

[6] M. Schlossman, X.-L. Wu, C. Frank, *Phys. Rev. B* **31**, 1478 (1985).

[7] J. H. Carpenter, J. H. J. Cho, B. M. Law, *Phys. Rev. E* **61**, 532 (2000).

[8] J. H. Carpenter, B. M. Law, D. S. P. Smith, *Phys. Rev. E* **59**, 5655 (1999).

[9] J.-H. J. Cho, B. M. Law, Gray, *J. Chem. Phys.* **116**, 3058 (2002).

[10] H. Zhao, A. Penninck-Sans, L.-T. Lee, D. Beysens, G. Jannink, *Phys. Rev. Lett.* **75**, 1977 (1995).

[11] J. R. Howse, J. Bowers, E. Manzanares-Papayanapoulos, I. A. McLure, R. Steitz, *Phys. Rev. E* **59**, 5577 (1999).

[12] J. Jestin, L. T. L. M. Privat, G. Zalczer, *Eur. Phys. J. B* **24**, 541 (2001).

[13] L. G. Parratt, *Phys. Rev.* **95**, 359 (1954).

[14] M. Tolan, *X-Ray Scattering from Soft-Matter Thin Films*, Springer Tracts in Modern Physics (Springer, Berlin, 1999).

[15] M. K. Sanyal, S. Hazra, J. K. Basu, A. Datta, *Phys. Rev. B* **58**, R4258 (1998).

[16] M. Brown, *et al.*, *Rev. Sci. Instrum.* **75**, 2536 (2004).

[17] J.-H. J. Cho, B. M. Law, *Phys. Rev Lett.* **89**, 1046101 (2002).

[18] J. Daillant, A. Gibaud, *X-Ray and Neutron Reflectivity:Principles and Applications*, Lecture Notes in Physics (Springer, Berlin, 1999).

[19] B. R. McClain, M. Yoon, J. D. Litster, S. G. J. Mochrie, *Eur. Phys. J. B.* **10** (1999).

Chapter 5

Comparison of critical adsorption scaling functions obtained from neutron reflectometry and ellipsometry

5.1 Introduction

At a solid-liquid or liquid-vapor interface of a binary fluid mixture there will in general be an adsorbed film in which the relative volume fraction of the components will differ significantly from the bulk composition. This adsorption is driven by a surface field h_1, which results from the difference in surface tensions of the components at that interface, where the component possessing the lower surface tension is more abundant in the adsorbed film compared with the bulk. Over length scales of $\sim 10\xi$, where ξ is the composition correlation length, the adsorbed film will decay to the bulk composition. Various phenomena, such as catalysis, electrolysis, and the permeability of membranes can be influenced by the presence and structure of an adsorbed film[1].

For the special case of a critical binary fluid mixture, which undergoes a bulk second order phase transition from an ordered phase separated state (the 2 phase region) to a disordered mixed state (the 1 phase region) at a critical temperature T_c, Fisher and de Gennes[2] postulated that the adsorption profile $\phi(z)$ at the interface would exhibit interesting

universal, system independent behavior sufficiently close to T_c. $\phi(z)$ is expected to depend upon two variables, a dimensionless depth z/ξ and the surface field h_1. If h_1 is sufficiently large so that the component possessing the lowest surface tension completely saturates the surface (i.e. $\phi(0) = 1$) then the adsorption profile becomes independent of h_1. In this **strong critical adsorption regime** the dependence of $\phi(z)$ upon z/ξ is usually defined using a local order parameter

$$m_{\pm}(z) = \phi(z) - \phi_c, \tag{5.1}$$

where the universal surface scaling behavior can be described by

$$m_{\pm}(z) = M_{-}t^{\beta}P_{\pm}[(z + z_e)/\xi_{\pm}]. \tag{5.2}$$

In these equations ϕ refers to the volume fraction of the preferentially adsorbed component as a function of distance z from the interface and ϕ_c is the bulk critical volume fraction. The coexistence curve, described by $M_{-}t^{\beta}$, separates the one phase from the two phase region of the binary fluid mixture while the correlation length $\xi = \xi_0 t^{-\nu}$ with reduced temperature $t =\mid T - T_c \mid /T_c$ where the bulk critical exponents $\beta \simeq 0.328$ and $\nu \simeq 0.632$[3]. M_{-} and ξ_0 are system dependent parameters. The universal surface scaling function P exhibits differing values in the one phase (subscript $+$) compared with the two phase region (subscript $-$).

For strong critical adsorption m must remain finite and non-zero at the critical temperature ($t = 0$), hence, m must lose it's t dependence for sufficiently small $x = z/\xi << 1$. This can only occur if[2]

$$P_{\pm}(x) \sim c_{\pm}x^{-\mu}, \mu = \beta/\nu. \tag{5.3}$$

The extrapolation length z_e, which appears in Eq. (5.2), prevents $P(x)$ from diverging at $z = 0$. This power law behavior eventually crosses over to an exponential decay

$$P_{\pm}(x) \sim P_{\pm}(\infty) + P_{\infty\pm}e^{-x} \tag{5.4}$$

at sufficiently large x where, because $P(x)$ is a universal function, $c_{\pm}$ and $P_{\infty\pm}$ will be universal numbers. In order that Eq. (5.4) correctly describe the bulk order parameter at

$z \to \infty$ we must additionally have

$$P_+(z \to \infty) \equiv P_+(\infty) = 0 \tag{5.5}$$

$$P_-(z \to \infty) \equiv P_-(\infty) = 1. \tag{5.6}$$

It has taken many, many years to determine a universal form for $P(x)$ which could describe the experimental results of many different critical liquid mixtures. In 1999 Carpenter and coworkers[4] finally found a form for $P(x)$ which could describe the ellipsometric critical adsorption results measured at the liquid-vapor interface of a number of different critical liquid mixtures. However, a disturbing feature which continues to plague this field is that $P(x)$ determined using other experimental techniques, such as neutron and X-ray reflectometry, often disagree with each other and also disagree with the form determined via ellipsometry. The primary purpose of this paper is to compare a careful neutron reflectometry experiment measured at the crystalline quartz-critical binary liquid mixture surface with $P(x)$ determined via ellipsometry.

It is important to prove that $P(x)$ is indeed universal and that the same functional form can describe the experimental results from many different critical binary liquid mixtures measured via many different experimental techniques because $P(x)$ serves as the basis for determining many other universal functions. For example, if the surface field h_1 is small then the surface composition $\phi(z)$ will depend not only upon the dimensionless depth $x = z/\xi$ but also upon h_1 where, in this **weak critical adsorption regime**, the local order parameter $m_\pm(z)$ will be described by a different universal function $G(x, h_1)$[5,6] which will reduce to $P(x)$ in the limit of large h_1. The determination of $G(x, h_1)$ is predicated upon a reliable determination of $P(x)$[7]. In a similar manner, if one of the components is highly polar then one finds that both the local surface composition and local orientational order vary with $x = z/\xi$, where the latter is caused by the interaction between the dipole and it's image when in the vicinity of a surface[8]. Determination of this surface orientational order is also dependent upon an accurate knowledge of $P(x)$[9].

This publication is set out as follows. In Sec. 2 we survey prior work on strong critical

adsorption and summarize the ellipsometric measurements for the $P(x)$ function. The experimental methods and analysis are described in Secs. 3 and 4, respectively. A summary is presented in Sec. 5.

5.2 Survey of prior work

There are a number of key developments in our understanding of critical adsorption. A brief historical perspective of these developments is given below. This survey of prior work will enable the reader to better understand the motivation for the current paper.

The first experimental observation of the effects of strong critical adsorption was made by Rusanov and co-workers[10] using the technique of ellipsometry. This work has largely gone unnoticed by later workers with the exception of Beaglehole[11]. Surprisingly this first observation predates the theoretical predictions of Fisher and de Gennes[2]. In this early work Rusanov et al. observed a divergence in the relative surface adsorption, defined as,

$$\Gamma = \int [m(z) - m(\infty)]dz. \tag{5.7}$$

The divergence in Γ is caused by the fact that $m(z)$ scales with z/ξ where, according to Eq. (5.2),

$$\Gamma \sim P_{\pm} t^{\beta-\nu} \tag{5.8}$$

with a universal integral

$$P_{\pm} = \int [P_{\pm}(x) - P_{\pm}(\infty)]dx$$

which takes differing values in the one and two phase regions.

The theoretical predictions of Fisher and de Gennes, encapsulated in Eqs. (5.2) and (5.3), stimulated a significant experimental effort using a variety of experimental techniques, including ellipsometry[12–15], evanescent-wave reflectometry[16,17], light scattering[18], and volumetry[19] to elucidate the functional form of $P(x)$. Ellipsometry provides a direct measure of Γ (at least far from T_c)[20] while the other techniques provide other (integral) measures

over $P(x)$[16–18]. The variation of $P(x)$ with x (which is hidden inside these universal integrals) can only be ascertained indirectly by getting sufficiently close to T_c ($t \lesssim 10^{-3}$) where ξ is sufficiently large so that, for the optical measurements, interference effects provide a non-linear measure of $P(x)$ via a solution of Maxwell's equations.

The universality of $P(x)$ was not fully appreciated until the work of Liu and Fisher[21] who compared experimental measurements on *two different* critical mixtures to see if a single functional form for $P(x)$ could describe both experiments. As appropriate models incorporating both (5.3) and (5.4) they considered the exponential Pade (EP) model

$$P(x) = c_+ \left(\frac{1}{1 - e^{-x}} + \left(\frac{c_+}{P_{\infty +}} \right)^{-\nu/\beta} \right)^{\frac{\beta}{\nu}} e^{-x}, \tag{5.9}$$

and the power law – exponential model

$$P(x) = c_+ \left(\frac{1}{x} + \left(\frac{c_+}{P_{\infty +}} \right)^{-\nu/\beta} \right)^{\frac{\beta}{\nu}} e^{-x}. \tag{5.10}$$

These functional forms have the advantage that they are continuous for all x. However, they are strictly only applicable in the one phase region because neither of these equations reduce to Eq. (5.6), applicable in the two phase region, in the limit of large x. Liu and Fisher found that the universal cross-over length scale $c_+/ \; P_{\infty +} \simeq 1.2$ in the one phase region by comparison with the evanescent-wave reflectometry results of Schlossman, Wu and Franck[17] and ellipsometry results of Schmidt and Moldover[14].

Theoretical estimates for the actual functional form of $P(x)$ have been derived in 3 dimensions using renormalization group (RG)[22] (to first order in $\epsilon = 4 - d$), Monte Carlo simulations (MC)[23] and local functional theory[24]. The local functional theory results were found to be in excellent agreement with both the RG and MC calculations. However, Smith and Law[26] found that neither the RG nor MC functional forms for $P(x)$ could quantitatively explain experimental ellipsometric data.

Another key measure, providing evidence for universality, is the value of the universal number c_+, which appears in Eq. (5.3). Flöter and Dietrich[25] reanalysed a large number

of earlier optical experimental measurements of strong critical adsorption to obtain an experimental estimate for $c_+ = 0.955 \pm 0.08$ (Table 1). This experimental estimate compared favorably with various theoretical estimates (Table 1) including RG[22], MC[23], interpolation[25] and local functional[24] estimates. One should note, however, that approximate agreement of the **universal number** c_+ from optical experiments with RG and MC estimates does **not** necessarily imply that the **full functional forms** from RG or MC for $P(x)$ can quantitatively describe experimental data, as noted above[26]. Part of the problem is that Eqs. (5.3) and (5.4) only represent the leading order terms. Higher order terms are expected to take the form

$$P_{\pm}(x) = c_{\pm}x^{-\beta/\nu} + c_{1\pm}x^{(1-\beta)/\nu} + c_{2\pm}x^{(2-\beta)/\nu} + c_{3\pm}x^{3-\beta/\nu} + ..., \tag{5.11}$$

at small x[22]. At large x, Liu and Fisher[21] suggested that

$$P_{\pm}(x) = P_{\pm}(\infty) + P_{\infty\pm}e^{-x} + P_{1\pm}e^{-2x} + P_{2\pm}e^{-3x} + ... \tag{5.12}$$

A more refined local functional theory analysis by Borjan and Upton[24] indicates that, for symmetry reasons, the large x expansion should be

$$P_{+}(x) = P_{+}(\infty) + P_{\infty+}e^{-x} + P_{2+}e^{-3x} + ... \tag{5.13}$$

in the *one phase region,* where only odd powers of e^{-x} are present. The presence of these higher order corrections at small and large x, therefore, necessarily influence the determination of $c_{\pm}$. Carpenter et al.[4] used a modified version of Eqs. (5.11) and (5.12), called the 'P1 model', where

$$P_{\pm}(x) = c_{\pm}x^{-\beta/\nu} + c_{1\pm}x^{(1-\beta)/\nu}, \quad x < x_0, \tag{5.14}$$

$$P_{\pm}(x) = P_{\pm}(\infty) + P_{\infty\pm}e^{-x} + P_{1\pm}e^{-2x}, x \geq x_0, \tag{5.15}$$

to re-examine whether or not the ellipsometric data of Smith[20] for four different critical mixtures could be fitted with a single universal function. (For historical reasons, in the one phase region, Eq. (5.15) is a truncation of Eq. (5.12) rather than the more accurate

Eq. (5.13).) In Eqs. (5.14) and (5.15) there are nine parameters $c_{\pm}, c_{1\pm}$, $P_{\infty\pm}$, $P_{1\pm}$ and x_0 that need to be determined where x_0 is a crossover parameter which separates the power law region from the exponential region. Carpenter et al. used the continuity of $P_{\pm}(x)$ and $dP_{\pm}(x)/dx$ at x_0, continuity of $m(z)$ at T_c plus three experimental constraints to reduce the number of adjustable parameters from nine to just one, specifically x_0. By adjusting this single universal parameter x_0, Carpenter described the critical adsorption behavior for four different critical liquid mixtures in both the one and two phase regions. The values for these nine parameters, determined from ellipsometric data, are given in Table 2. This universal functional form for $P(x)$ found by Carpenter also described the ellipsometric data for a non-polar critical liquid mixture at the liquid-vapor surface[27] and a critical mixture in contact with a molecularly smooth Si wafer surface[28]. Carpenter also fitted the one phase ellipsometric data of Smith using the exponential Pade model (Eq. (5.9) and Table 2) and found reasonable but a slightly poorer fit (as indicated by the value of the standard deviation σ) compared with the P1 model. It is important to note that the value of $c_+ = 0.788$ (Table 2) for the P1 model agrees reasonably well with the exponential Pade estimate ($c_+ = 0.817$, Table 2), earlier optical experiments ($c_+ \sim 0.955 \pm 0.08$[25], Table 1) and theoretical estimates ($c_+ \sim 0.717 - 0.94$[22,23,25], Table 1). The difference between c_+ for the P1 model and the optical and theoretical estimates could be due to the presence of the higher order terms in Eqs. (5.14) and (5.15). One can safely state that the leading order amplitude c_+ from visible light optical experiments and theory lies in the range $c_+ \sim 0.72 - 0.96$.

Theoretical work by Dietrich and Schack[29] suggested that both the amplitude c_+ and exponent μ of the power law critical adsorption behavior (Eq. (5.3)) could be measured directly via neutron or X-ray reflectometry. This paper stimulated a number of experimental attempts at measuring these parameter as summarized in Table 1. However, the values determined for $c_+ \sim 0.1 - 1.9$ from neutron[30–33] and X-ray[34] experiments fall in a much broader range than found from visible light optical experiments. The recent neutron reflectometry experiment of Bowers et al.[33] seems to be in closest conformity to theoretical

Technique	Liquid mixture/substrate	c_+	$\mu = \beta/\nu$
RG[22]	Theory	0.717	
MC[23]	Theory	0.866	
Interpolation[25]	Theory	0.94 ± 0.05	
Local functional[24]	Theory	0.857	
Optical[25]	Various/air or glass	0.955 ± 0.08	
Ellipsometry - P1[4]	Various/air	$0.788^{+0.009}_{-0.015}$	
Ellipsometry - EP[4]	Various/air	0.817	
Neutron[30]	MC*/air	0.34	0.52
Neutron[31]	BW*/Si	0.11	0.53 ± 0.02
Neutron[32]	FH/air	1.78 ± 0.2	0.54 ± 0.03
Neutron[32]	CM*/air	0.94 ± 0.15	0.46 ± 0.03
Neutron[32]	MC*/air	0.97 ± 0.15	0.49 ± 0.05
Neutron[33]	H*F/Si	0.90 ± 0.04	0.514 ± 0.018
Neutron (this work)	W*P/quartz	$0.788^{\S}$	$0.519^{\S}$
X-ray[34]	DT/air	1.87	

Table 5.1: *Critical adsorption parameters. The following abbreviations have been used in this table: MC* = methanol + deuterated cyclohexane, BW* = 2-butoxyethanol + deuterated water, FH = n-hexane + perfluorohexane, CM* = cyclohexane + deuterated methanol, H*F =d-hexane+perfluorohexane, W*P= deuterated water + 3-methylpyridine, DT = n-dodecane+tetrabromoethane.*
§*From use of the P1 model.*

Model	Phase	$x_{o\pm}$	$c_\pm$	$c_{1\pm}$	$P_{\infty\pm}$	$P_{1\pm}$	$10^4\sigma$
P1	1	1.15	$0.788^{+0.009}_{-0.015}$	-0.245	$0.963^{+0.117}_{-0.201}$	1.437	1.3756
	2	1.15	$1.117^{+0.013}_{-0.021}$	0.169	$0.572^{+0.357}_{-0.152}$	0.533	
EP	1		0.817		1.035		1.5492

From Ref.[4].

Table 5.2: *Critical adsorption scaling function models*

expectations. However, as mentioned above, agreement of c_+ from experiments with RG and MC estimates does not necessarily imply that the RG and MC models for $P(x)$ will be able to quantitatively explain experimental data. Here we compare the P1 model for $P(x)$, which quantitatively described ellipsometric data[4], with a neutron reflectometry experiment of strong critical adsorption.

For completeness, we should mention one further theoretical approach to critical adsorption before proceeding on to describe the neutron experiments. The scaling regime described by Ising critical exponents, and embodied in Eqs. (5.2) and (5.3), is only valid when fluctuations are important. Outside the scaling regime, the thermodynamic behavior is described by mean field concepts. Kiselev and coworkers[35] developed a (complicated) cross-over adsorption theory which incorporates both the cross-over in surface behavior as well as the cross-over in bulk behavior. Ising behavior is found at $\mid t \mid << Gi$, close to T_c, and for distances $z >> \xi_o Gi^{-\nu}$. This behavior crosses over to mean field behavior at $\mid t \mid >> Gi$, far from T_c. Here Gi is the Ginzburg number. A study of a series of non-critical liquid mixtures of aniline plus cyclohexane[36] indicated that Gi lies in the broad range $0.0005 < Gi < 0.005$. This cross-over adsorption theory is perhaps most useful for describing off critical liquid mixtures over a wide temperature and composition range. The concepts within this theory should also be applied to critical mixtures at $\mid t \mid >> Gi$ and for distances $z << \xi_o Gi^{-\nu}$. The cross-over adsorption theory does not include the higher order corrections to $P(x)$, described by Eqs. (5.11) - (5.13). It is not yet understood how the higher order corrections to $P(x)$ compare with the mean field contributions in the differing reduced temperature and distance regimes.

5.3 Experimental Methods

There are a number of experimental difficulties associated with neutron and X-ray experiments of strong critical adsorption that make these experiments somewhat difficult to implement. These difficulties could potentially explain some of the differences in the exper-

imental results noted above and listed in Table 1. Specifically, these difficulties include the following:

(A) If one is studying the liquid-vapor surface of a critical liquid mixture then, depending upon the cell design, the beam may have to pass through a macroscopic liquid meniscus at the entrance and exit windows of the sample cell because the incident beam is coming in at very small incident angles near grazing incidence. Differing groups have attempted to get around this meniscus problem in a number of different ways by (i) making the sample cell very long, which may create certain problems with regard to accurate temperature control, (ii) trying to account experimentally for this meniscus effect[32] or (iii) overfilling a sample cell such that the liquid-vapor surface sits above the sample cell lip[34].

(B) If 'strong' transverse thermal gradients are present ($\gtrsim 5mK/cm$) then convective flow within the liquid may perturb the adsorption profile at any surface[37].

(C) Mechanical vibrations can perturb the reflected beam. Vibration problems are frequently minimized by making the bulk liquid sample very thin ($< 1mm$ thick) so that longer wavelength capillary waves are damped out by the presence of the underlying solid cell wall.

(D) Depending upon the scattering length density of the liquid mixture relative to the adjacent substrate (i.e. air or a solid), a large external critical angle may limit how close in temperature one can come to T_c. For example, the critical wave vector is given by

$$Q_c = 4\sqrt{\pi \Delta SLD} \tag{5.16}$$

where ΔSLD is equal to the difference in scattering length densities between the two adjacent bulk phases. Surface features of length scale ξ occur approximately at a wave vector

$$Q = \frac{2\pi}{\xi}. \tag{5.17}$$

Hence, for sufficiently large correlation lengths ξ (close to T_c), the critical adsorption features that one would like to study occur at very small Q. At the critical wave vector Q_c, the penetration depth (which determines the probe depth) is infinite. Thus very long range

surface features are probed, but at extremely poor resolution in the vicinity of the critical edge. In order to investigate the scaling region close to T_c, one should therefore make Q_c very small. According to Eq. (5.16) small Q_c can be obtained by selecting similar scattering length densities for the substrate and liquid mixture where, in addition, one would also like good contrast between the adsorbed layer and the adjacent bulk phases. Fig. 5.1 compares the relative benefits of small and large Q_c. Fig. 5.1 a shows neutron reflectivity data for a critical mixture of deuterated water plus 3-methylpyridine (W*P) against a crystalline quartz substrate, which is studied later in this paper. This system possesses a small $Q_c \approx 0.06nm^{-1}$ because the scattering length densities of the two bulk phases are similar (Fig. 5.1 a, inset and Table 3). The deuterated water, which adsorbs against the crystalline quartz substrate, provides good surface contrast relative to the two bulk phases. The solid lines are fits to the experimental data using a P1 model, as described later. For this system one can readily distinguish all of the experimental reflectivity curves between $\Delta T = T_c - T = 0.08°C$ (crosses) and $5.0°C$ (triangles). This behavior should be compared with a system possessing a large Q_c, obtained via computer calculations of the P1 model for the same critical mixture but now against air (Fig. 5.1 b). In this case, the 3-methylpyridine adsorbs at the surface because it possesses the lowest surface tension. $Q_c \approx 0.16nm^{-1}$ where there is a large drop in the reflectivity which is especially prominent for temperatures very close to T_c. The $\Delta T = 0.08°C$ (crosses) and $0.25°C$ (circles) data are almost indistinguishable. Additionally, in a real neutron reflectometry experiment, because of the noise in the data and finite resolution in Q, it may be difficult in practice to distinguish between the $0.25°C$ (circles) and $0.5°C$ (wide diamonds) data. This behavior is reminiscent of an earlier X-ray reflectometry experiment[34], completed by a couple of the current authors, from the liquid-air surface of the critical mixture tetrabromoethane + n-dodecane where Q_c was large with a value of $\approx 0.28nm^{-1}$. In this experiment, it was found that the X-ray data for $\Delta T \lesssim 1°C$ could not be distinguished; hence, phenomena very close to T_c could not be studied. The system W*P against quartz, studied in this paper, has other advantages as

well besides having a small Q_c. The neutrons are incident onto the surface through the small polished crystalline quartz substrate. Problems (A) to (C), mentioned above, are therefore eliminated. There is no liquid meniscus problem. The system is small, hence, it is easy to ensure that transverse thermal gradients are small. The solid substrate damps out any mechanical vibrations.

W*P possesses a closed loop phase diagram with both an upper and a lower critical temperature. For convenience, we chose to work near the lower critical temperature ($T_c \approx 37°C$) where the system was in the one (two) phase region for temperatures below (above) T_c. Deuterated water (isotopic purity of 99.96%, CAS [7789-20-0]) and 3-methylpyridine (99.5+% pure, CAS[108-99-6]) were both obtained from Aldrich and used without any further purification. The critical mixture volume fraction of 69.1% deuterated water was determined using a standard volumetric procedure, where both phases have equal volumes in the two-phase region for temperatures sufficiently close to the critical temperature T_c. In the present case, at $20mK$ above T_c (in the two phase region), the volumes of the two phases were equal to within 2% which indicated a difference from the critical volume fraction of $\Delta\phi \lesssim 0.002$.

The sample cell consisted of a crystalline quartz substrate of width 3.8, length 8.3 and height 1.3 cm and a stainless steel trough of depth 3 mm. A teflon encapsulated O-ring provided a seal between the quartz substrate and the trough. The measurable region of the interface was approximately 2 cm by 5 cm. Two teflon minivalves were used to access the cell. One valve was a fill port while the other valve enabled displaced air to exit the cell. The cell, substrate, and O-ring were separately sonicated in methanol, acetone, and ethanol, and then rinsed with distilled, deionized water. Both teflon valves were similarly sonicated, and purged thoroughly with distilled, deionized water. After 1 day in an oven at $110°C$ the sample cell was assembled inside a laminar flow hood. The sample cell was filled at room temperature with the critical liquid mixture, leaving a bubble of $\sim 3mm$ diameter which subtended no more than 3% of the exposed substrate area. The cell was then elevated to

a temperature of 35°C, which was 2°C below the critical temperature. One valve was then opened to allow the cell pressure to come into equilibrium with the atmospheric pressure. The bubble was necessary to prevent a large buildup of pressure within the sample cell. In general the cell was tilted during measurements, thus removing the air bubble from the reflection region. The sample cell was contained in a temperature controlled environment similar to the one described in[38]. The thermal stability was better than $2.0 mK/h$ where thermal temperature gradients were less than $1 mK/cm$. Three Yellow Springs Instrument 44034 thermistors were used, one for temperature control, and the other two, one at each end of the sample cell, for temperature and temperature gradient monitoring. The critical temperature was measured in the sample cell 3 days before the experiment, and found to be $T_c = 37.055 \pm 0.01°C$. The critical temperature was measured again 2 weeks after the experiment, and had not drifted beyond the original range of uncertainty.

Beamline NG7 at the National Center for Neutron Research at the National Institute of Standards and Technology (NIST) in Gaithersburg, Md was used to collect neutron reflectometry data at a neutron wavelength of $\lambda = 0.476$ nm for a wave vector step size of 0.005/nm, which gave an uncertainty in the wave vector of $\Delta Q = \pm 0.0025$/nm. Measurements were taken at $\Delta T = T_c - T = 0.08$, 0.25, 0.5, 1.12, 2.5, 5, 10, and 20°C below the critical temperature over a 4 day period. From these measurements the critical wave vector was found to be $Q_c = 0.059$/nm for this crystalline quartz-critical mixture surface, which is in reasonable agreement with Eq. (5.16). The temperature range studied is much closer to T_c than was possible with any previous neutron or X-ray experiment, mainly because Q_c is so small. For each measurement the final set point temperature was approached from below. In each case, after giving the system two or more hours to come into thermal equilibrium, two separate 1 hour measurements were taken over the low part of the Q range. By comparing these measurements we could determine if the system had been given enough time to come into thermal equilibrium. Repeatability was tested by repeating our measurement at ΔT = 5°C, with an intervening measurement at ΔT = 2.5°C. Addi-

tionally, measurements taken on the last day of the experiment at ΔT = 10, 20 and 0.5°C were consistent with measurements taken during the first two days at ΔT = 5 and 0.6°C. The first few reflectometry measurements were taken over a Q range of 0.04 to 0.61 nm^{-1}; however, background scattering was found to dominate the data in the upper part of this range. Subsequent measurements were therefore restricted to a maximum Q of 0.25 nm^{-1}. The rms surface roughness of the crystalline quartz-air interface was measured in a separate experiment, using the same reflectometer, and found to have a value of 0.34 ± 0.03 nm.

5.4 Analysis

The neutron reflectometry data R versus Q is shown in Fig. 5.2 at various temperatures. In this paper the P1 model is compared with this neutron reflectometry data using the method suggested by Parratt[39]. For a given model, an effective refractive index profile $n(z)$ is approximated by a series of slabs of uniform refractive index. One then recursively solves Maxwell's equations for each interface, taking into account what happened at the previous interface. By this method one can approximate a profile, and the resulting reflectivity curve, as precisely as one wishes. The refractive index for neutrons within a particular slab at depth z_i is given by

$$n(z_i) \approx 1 - \frac{\Omega\lambda^2}{2\pi}[\phi(z_i)SLD_{W^*} + (1 - \phi(z_i))SLD_P], \tag{5.18}$$

where $\phi(z_i)$ is the local volume fraction of the adsorbed component (i.e. deuterated water), $\Omega = (V_{W^*}+V_P)/V_{W^*+P} \simeq 1$ is the volume change on mixing while SLD_{W^*} and SLD_P are the neutron scattering length densities of, respectively, deuterated water and 3-methylpyridine (Table 3,[40]). In this equation $\phi(z_i)$ is related to the surface scaling function $P_+(z_i)$ through Eqs. (5.1) and (5.2) with the function $P_+(z_i)$ determined by the P1 model, namely, Eqs. (5.14) and (5.15) where the five parameters c_+, c_{1+}, $P_{\infty+}$, P_{1+} and x_0 are given in Table 2. The system dependent parameters M_- and ξ_0 were determined by fitting the P1 model to ellipsometric data collected by Smith[41] for this particular liquid mixture. The best fit values, $M_- = 0.7$ and $\xi_0 = 0.508$ nm, were in fair agreement with the values quoted in[41]. In

comparing the neutron reflectometry data with the P1 model the only adjustable parameters occur in the vicinity of the surface at $z = 0$ where the P1 model must be joined in some manner onto the surface composition. Specifically, there were three adjustable parameters for each temperature, namely, the surface composition ϕ_s, the thickness of the surface layer l_s and the extrapolation length z_e (Eq. (5.2)) which joins the P1 model smoothly onto the surface composition. One expects ϕ_s, l_s and z_e to be similar for all temperatures. One also requires an additional adjustable parameter ΔQ, corresponding to a shift in Q, because in this experiment the critical wave vector Q_c is so small. We expect that ΔQ should be similar in magnitude to the instrumental resolution of ± 0.0025 nm^{-1}. Following standard non-linear least squares fitting procedures[42] the best fit to the experimental data is obtained by adjusting ϕ_s, l_s, z_e and ΔQ for a minimum in χ^2 where

$$\chi^2 = \sum_{j=1}^{N} \frac{\left[R_{P1}(Q_j) - R(Q_j)\right]^2}{{\sigma_j}^2} \tag{5.19}$$

and $R_{P1}(Q_j)$ and $R(Q_j)$ are, respectively, the reflectivity for the P1 model and experimental neutron data at wave vector Q_j. In carrying out this fitting procedure one must take particular care in selecting the weight σ_j for each data point. If the standard weight $\sigma_j = \sqrt{R(Q_j)}$ is selected then the high Q data points have insufficient impact on the overall fit, thus leading to an inaccurate picture of the profile. This difficulty arises because the reflectivity decreases by several orders of magnitude for increasing Q above Q_c. One must also be careful not to overweight the higher Q data points because then the fit becomes susceptible to the noise in the higher Q data. We examined a number of different measures for σ_j and found that

$$\sigma_j \ = R(Q_j)\sqrt{1 - Log_{10}(R(Q_j))} \tag{5.20}$$

gave results that were consistent over the entire Q range. The first term, in Eq. (5.20) $(R(Q_j))$, compensates for the differing orders of magnitude in the reflectivity between low and high Q data while the second term decreases the weighting for the noisier higher Q data.

Substance	$10^4 SLD$ (nm^{-2})	$10^7(dSLD/dT)$ (nm^{-2}K^{-1})
Crystalline quartz	4.18	
D_2O	6.37	-1.0
3-methylpyridine	1.43	-0.5
Critical mixture (at $\phi_{D_2O} = 0.691$)	4.84	

From Ref.[40].

Table 5.3: *Scattering length densities at 25 ^0C*

We modeled our system with an intermediate layer of thickness l_s and constant composition ϕ_s (the surface layer referred to above) between our quartz substrate and the Carpenter P1 decay model. The inclusion of the intermediate layer was inspired from the results in[34]. The extrapolation length z_e, which is generally chosen such that $\phi(z = 0) = 1$, was instead chosen such that the P1 decay profile would begin with a composition of ϕ_s. In our initial fits l_s was allowed to vary from 0 nm (i.e. no intermediate film) to 2 nm. The best fits for $\Delta T = 0.08, 0.25, 0.5, 1.12, 2.5°C$, consistent with the idea that l_s and ϕ_s should be independent of temperature, were obtained with a surface thickness $l_s = 0$ nm for the adsorbed film and a surface volume fraction $\phi_s \equiv \phi_{D_2O}(z = 0)$ between 0.878 and 0.896. These fits indicate that no intermediate film is necessary and the P1 model alone suffices to describe behavior within $2.5°C$ of the critical temperature. The best fit to the $5°C$ data also had an intermediate layer thickness of 0 nm, but in this case $\phi_s = 0.918$, outside the range for fits at temperatures nearer to T_c. This trend of increasing ϕ_s continues at 10 and $20°C$. In all cases where the intermediate layer is of zero thickness, the layer serves only to control the initial value of ϕ in the P1 decay profile. These results are tabulated in Table 4 and fits are displayed in Fig. 5.2 (solid line). The higher $\Delta T \geq 5°C$ data can also be equally well fitted with an alternative model where ϕ_s is held *constant* at 0.896 and l_s is varied. This alternative model possesses a similar χ^2 and cannot visually be distinguished from the previous $l_s = 0$ model with variable ϕ_s (Fig. 5.2). Undoubtedly, the $\Delta T \geq 5°C$ experimental data could equally well be fitted by some combination of these two models. This

break down of the Carpenter model further from T_c is perhaps not surprising as, in this region, a cross-over to mean field behavior is expected[36]. However it should be noted that this break down of the Carpenter model, exhibited by the neutron measurements far from T_c, does not negate the Carpenter ellipsometric results[4] which were primarily sensitive to surface structural variations within $1°C$ of T_c.

Within $2.5°C$ of T_c the Carpenter model with no intermediate layer ($l_s = 0$) and $\phi_s = 0.887 \pm 0.009$ provides a good description of the experimental data. A surprising result of this analysis is that $\phi_s \neq 1$, which would seem to indicate weak adsorption, although fits to the weak critical adsorption scaling equations in[7] provided unsatisfactory results. The likely physical reason for this partial surface saturation, with $\phi_{D_2O}(z = 0) \simeq 0.887$, is competing hydrogen bonding with the surface between deuterated water and 3-methylpyridine (3-$CH_3(C_5H_4N)$). This Carpenter model close to T_c provides a good but not perfect description of the experimental data as the results in Table 4 exhibit a small systematic trend in the wavevector shift ΔQ as one approaches T_c. This trend is *small* and falls within the wavevector uncertainty of $\pm 0.0025/nm$. The small critical wavevector $Q_c = 0.059/nm$, for our system, undoubtedly makes this small ΔQ shift visible. There are a number of potential causes for this small systematic trend in ΔQ :

(i) Our sample cell and temperature controlled environment are made of a number of disparate materials, including aluminium, stainless steel, crystalline quartz, a teflon encapsulated O-ring and nylon capped set screws each with their own differing thermal expansion coefficients. A rotation of 0.006^o would suffice to account for the apparent range in ΔQ. We cannot rule out this possibility.

(ii) In the above neutron analysis, as well as, the Carpenter ellipsometric analysis[4] it was assumed that the volume change on mixing $\Omega = (V_{W^*} + V_P)/V_{W^*+P} = 1$. This is a reasonable approximation to within 1 or 2%[43], however, a $\Omega \neq 1$ could potentially explain the small ΔQ trend exhibited in Table 4 for $\Delta T \leq 2.5°C$. Kayser[43] found that $\Omega = 0.983 \pm 0.036(-t)^{\beta}$ in the two phase region of the critical binary liquid mixture nitromethane + carbon disulfide.

As far as we are aware the temperature behavior of Ω in the one phase region has not been studied. A small deviation of Ω from 1.00 significantly influences the value of ΔQ. For example, we have examined the influence of $\Omega = 0.995$ in Table 4 for $\Delta T = 0.08°C$. This small deviation of Ω from 1.00 significantly alters the value of ΔQ while only marginally changing the value of ϕ_s. Hence, the ΔQ trend for the Carpenter model (with $l_s = 0$) at $\Delta T \lesssim 2.5°C$ could be due to this little understood parameter Ω.

In this experiment Q_c is small. One therefore needs to carefully consider the instrumental resolution and how this might influence the results. Q depends upon both λ and the incident angle θ. The beam is not perfectly monochromatic. Additionally, the finite size of the beam, sample, and detector assure that there will be a range of θ values within the beam. Thus, for a given data point, one is measuring R over a range of values $Q \pm \Delta Q/2$. Resolution depends on the ratios $\Delta\lambda/\lambda$ and $\Delta\theta/\theta$. For the NG7 reflectometer $\Delta\lambda/\lambda = 0.025$. For the geometry of our system we calculate that $\Delta\theta/\theta = 0.025$. Simulations demonstrated that even doubling the calculated value of $\Delta\theta/\theta$ had a negligible influence on the results. The relatively small size of our sample has assisted us in this regard.

5.5 Summary

In this paper we have found good agreement between critical adsorption results for a neutron reflectometry experiment on the critical mixture deuterated water plus 3-methylpyridine against a crystalline quartz substrate within $2.5°C$ of T_c and the analysis of Carpenter et. al.[4] on ellipsometric data taken on similar systems. This agreement differs from much of the previous neutron and X-ray literature on strong critical adsorption at the surfaces of critical binary mixtures, as summarized in Table 1, where in many cases there is disagreement between the various X-ray, neutron and ellipsometry experiments as well as theory. One unexpected result, which has arisen from this work, is that the surface composition ϕ_s of the preferentially adsorbed component (in this case deuterated water) is not completely saturated, as is normally assumed for strong critical adsorption. More specifically we have

Table 4 : Fitting parameters for neutron data

$\Delta T(^{\circ}C)$	ϕ_s	l_s (nm)	$10^3\Delta Q$ (nm^{-1})	χ^2	Ω
0.08	0.895	0.00	2.3±0.3	7.35	1
0.25	0.885	0.00	1.9±0.2	19.0	1
0.5	0.888	0.00	0.88±0.2	12.4	1
1.12	0.878	0.00	0.64±0.2	6.22	1
2.5	0.896	0.00	0.02	15.6	1
5	0.918	0.00 (fixed)	-0.04±0.2	20.8	1
10	0.939	0.00 (fixed)	0.34	8.85	1
20	0.998	0.00 (fixed)	0.48	24.6	1
5	0.896 (fixed)	0.482	-0.10 ±0.2	20.9	1
10	0.896 (fixed)	0.706	0.34	8.83	1
20	0.896 (fixed)	1.10	0.51	25.0	1
0.08	0.900	0	1.4	7.97	0.995

Table 5.4:

found that the surface volume fraction of deuterated water is $\phi_s \simeq 0.89$ for this particular system. We attribute this partial saturation to competing hydrogen bonding for the crystalline quartz surface between deuterated water and 3-methylpyridine.

A novelty introduced in this work, which enabled us to get much closer to the critical temperature T_c than previous X-ray or neutron studies, was the use of a crystalline quartz substrate which was closely matched to the scattering length density of the critical liquid mixture. This choice gave rise to a very small critical wave vector $Q_c \sim 0.06nm^{-1}$ which enabled us to probe very large length scales (corresponding to small reduced temperatures t) in a region where scaling is expected to hold. A limitation of the current work is that reflectivity data could only be collected out to a maximum Q of $\sim 0.25nm^{-1}$. Reflectivity data collected from our system at higher Q was dominated by bulk liquid background scattering. There is still room for improvement in our experimental design. A very thin liquid sample would allow us to collect reflectivity data at very large Q because such a cell would minimize the background scattering[44]. Such an improvement would provide superior

resolution of the small length scale interfacial features.

5.6 Acknowledgements

One of the authors (BML) acknowledges support for this work from the US Department of Energy through Grant No. DE-FG02-02ER46020 and partial support through the US National Science Foundation through Grant No. DMR-0603144. Oak Ridge National Laboratory is managed for the U.S. Department of Energy under contract DE-AC05-00OR22725 by UT-Battelle LLC. The authors acknowledge valuable discussions with Greg Smith on various neutron reflectometry related issues.

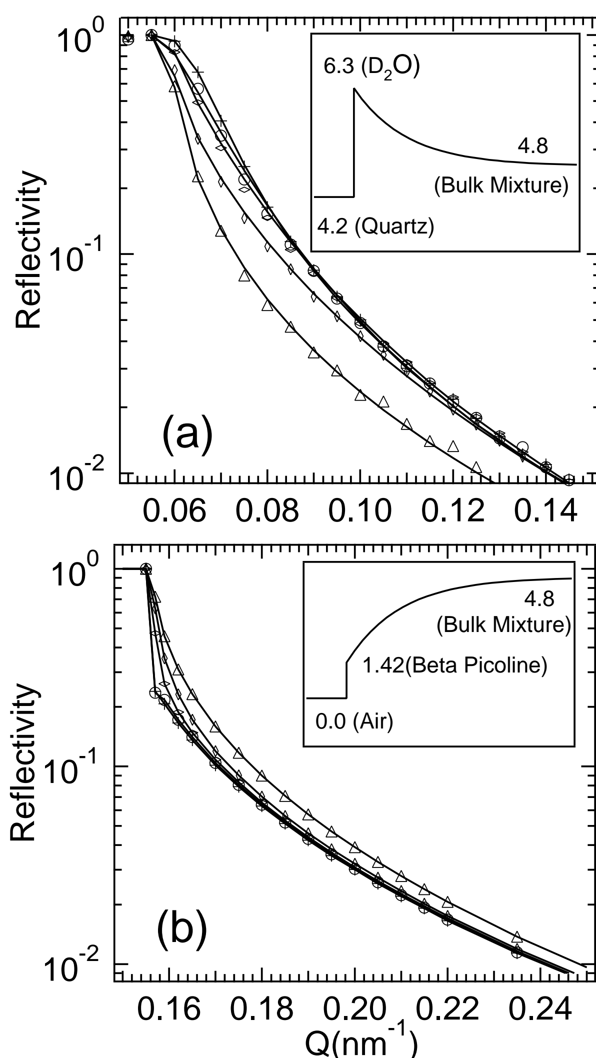

Figure 5.1: *Comparison between a critical mixture system with either a small or a large critical scattering vector, Q_c. (a) Experimental neutron data where Q_c is small for the critical mixture D_2O and 3-methylpyridine against a crystalline quartz substrate; D_2O adsorbs against the surface. The lines are fits to the data using the P1 model, as described in the text. (b) Computer calculations using the P1 model where Q_c is large for the same critical mixture against air. Here 3-methylpyridine adsorbs against the surface. For both (a) and (b), a schematic of the scattering length densities (in units of $10^{-4}/nm^2$) are shown in the insets. The differing neutron reflectivity curves possess temperature differences of $\Delta T = T_c - T =$ 0.08 (crosses), 0.25 (circles), 0.5 (wide diamonds), 1.12 (tall diamonds), and $5.0°C$ (triangles).*

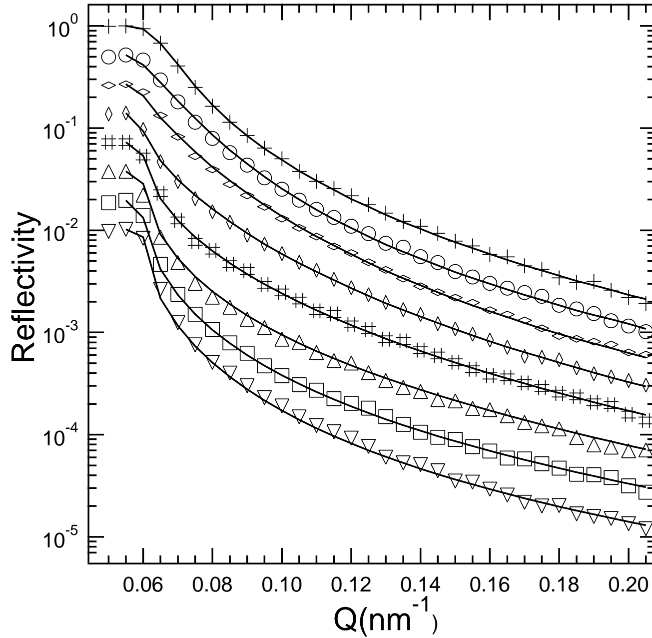

Figure 5.2: *Neutron reflectometry data taken at $\Delta T = 0.08$ (crosses), 0.25 (circles), 0.5 (wide diamonds), 1.12 (tall diamonds), 2.5 (number symbol), 5.0 (triangles), 10.0 (squares), and 20.0°C (inverted triangles) for the critical mixture D_2O and 3-methylpyridine against a crystalline quartz substrate. The solid lines represent fits where the volume fraction of D_2O in the adsorbed surface layer is allowed to vary and the thickness of the adsorbed layer is fixed at $l_s = 0$ (see Table 4). The higher $\Delta T = 5.0, 10.0$ and $20.0°C$ data can be equally well fitted for fixed $\phi_s = 0.896$ and variable l_s (Table 4) where no discernible difference in the fits can be observed (solid lines). For clarity each curve has been displaced vertically by a factor of 0.07.*

Bibliography

[1] A. W. Adamson, *Physical chemistry of surfaces* (Wiley, New York, 1982).

[2] M. E. Fisher and P.-G. de Gennes, C. R. Acad. Sci. Paris B **287**, 207 (1978).

[3] M. E. Fisher and J. -H. Chen, J. Phys. (Paris) **46**, 1645 (1985).

[4] J. H. Carpenter, B. M. Law, and D. S. P. Smith, Phys. Rev. E **59**, 5655 (1999); J. H. Carpenter, J.-H. J. Cho and B. M. Law, Phys. Rev. E **61**, 532 (2000).

[5] M. E. Fisher and H. Au-Yang, Physica **101A**, 255 (1980); H. Au-Yang and M. E. Fisher, Phys. Rev. B **21**, 3956 (1980).

[6] U. Ritschel and P. Czerner, Phys. Rev. Lett. **77**, 3645 (1996).

[7] J.-H. J. Cho and B. M. Law, Phys. Rev. Lett. **86**, 2070 (2001); Phys. Rev. E **65**, 011601 (2001).

[8] P. Frodl and S. Dietrich, Phys. Rev. E **48**, 3741 (1993).

[9] J.-H. J. Cho and B. M. Law, Phys. Rev. Lett. **89**, 146101 (2002); Phys. Rev. E **67**, 031605 (2003).

[10] A. I. Rusanov, Prog. Surf. Membr. Sci. **4**, 57 (1971).

[11] D. Beaglehole, in *Fluid Interfacial Phenomena*, edited by C. A. Croxton (Wiley, New York, 1986).

[12] D. Beaglehole, J. Chem. Phys. **73**, 3366 (1980); **75**, 1544 (1981).

[13] B. Heidel and G. H. Findenegg, J. Phys. Chem. **88**, 6575 (1984); J. Chem. Phys. **87**, 706 (1987); R. Süssmann and G. H. Findenegg, Physica A **156**, 114 (1989).

[14] J. W. Schmidt and M. R. Moldover, J. Chem. Phys. **83**, 1829 (1985).

[15] J. W. Schmidt, Phys. Rev. A **41**, 885 (1990).

[16] C. Franck and S. E. Schnatterly, Phys. Rev. Lett. **48**, 763 (1982); C. Franck, J. Chem. Phys. **82**, 5633 (1985); J. A. Dixon, M. Schlossman, X.-L. Wu and C. Franck, Phys. Rev. B **31**, 1509 (1985).

[17] M. Schlossman, X.-L. Wu and C. Franck, Phys. Rev. B **31**, 1478 (1985).

[18] D. Beysens and S. Leibler, J. Phys. (Paris) Lett. **43**, L133 (1982).

[19] S. Blümel and G. H. Findenegg, Phys. Rev. Lett. **54**, 447 (1985).

[20] D. S. P. Smith and B. M. Law, Phys. Rev. E **52**, 580 (1995); **54**, 2727 (1996).

[21] A. J. Liu and M. E. Fisher, Phys. Rev. A **40**, 7202 (1989).

[22] H. W. Diehl and M. Smock, Phys. Rev. B **47**, 5841 (1993); **48**, 6470(E) (1993).

[23] M. Smock, H. W. Diehl, and D. P. Landau, Ber. Bunsenges. Phys. Chem. **98**, 486 (1994).

[24] Z. Borjan and P. J. Upton, Phys. Rev. E **63**, 065102(R) (2001).

[25] G. Flöter and S. Dietrich, Z. Phys. B **97**, 213 (1995).

[26] D. S. P. Smith and B. M. Law, Phys. Rev. E **55**, 620 (1997).

[27] J.-H. J. Cho, B. M. Law and K. Gray, J. Chem. Phys. 116, 3058 (2002).

[28] J.-H. J. Cho and B. M. Law, Phys. Rev. E **72**, 041601 (2005).

[29] S. Dietrich and R. Schack, Phys. Rev. Lett. **58**, 140 (1987).

[30] H. Zhao, A. Penninckx-Sans, L.-T. Lee, D. Beysens and G. Jannink, Phys. Rev. Lett. **75**, 1977 (1995).

[31] J. R. Howse, J. Bowers, E. Manzanares-Papayanopoulos, I. A. McLure and R. Steitz, Phys. Rev. E **59**, 5577 (1999).

[32] J. Jestin, L.-T. Lee, M. Privat and G. Zalczer, Eur. Phys. J. B **24**, 541 (2001).

[33] J. Bowers, A. Zarbakhsh, H. K. Christenson, I. A. McLure, J. R. P. Webster and R. Steitz, Phys. Rev. E **72**, 041606 (2005).

[34] L. W. Marschand, M. Brown, L. B. Lurio, B. M. Law, S. Uran, I. Kuzmenko and T. Gog, Phys. Rev. E **72**, 011509 (2005).

[35] S. B. Kiselev, L. Lue and M. Yu. Belyakov, Phys. Lett. A **251**, 212 (1999); **260**, 168 (1999); S. B. Kiselev, J. F. Ely and M. Yu Belyakov, J. Chem. Phys. **112**, 3370 (2000).

[36] J. K. Whitmer, S. B. Kiselev and B. M. Law, J. Chem. Phys. **123**, 204720 (2005).

[37] D. S. P. Smith, unpublished.

[38] M. Brown, S. Uran, B. Law, L. Marschand, L. Lurio, I. Kuzmenko and T. Gog, Rev. Sci. Instrum. **75**, 2536 (2005).

[39] L. G. Parratt, Phys. Rev. **95**, 359 (1954).

[40] A. Munter, Scattering length density calculator. Retrieved September 10, 2005 from http://www.ncnr.nist.gov/resources/sldcalc.html.

[41] D. S. P. Smith and B. M. Law, J. Chem. Phys. **99**, 9836 (1993).

[42] R. P. Bevington and D. K. Robinson, *Data reduction and error analysis for the physical sciences* (McGraw-Hill, New York, 1992), 2nd ed.

[43] R. F. Kayser, Phys. Rev. B **34**, 3254 (1986).

[44] J. Majewski, private communication.

Chapter 6

X-ray and ellipsometric study of strong critical adsorption

6.1 Introduction

At the liquid-vapor interface of a binary liquid mixture there will usually be an adsorbed layer in which the component with the lower surface energy at that interface will dominate the composition. Over a length scale on the order of 10ξ, where ξ is the composition fluctuation correlation length, the composition profile will decay to the bulk composition. This composition differential between the bulk and the surface is dependent upon the surface field h_1[1,2], which depends upon the difference in surface energies between the two components. In 1978 Fisher and de Gennes[3] hypothesized that in the case of a binary liquid mixture which was critical with respect to the demixing phase transition, i.e. which would transition from a state of two coexisting phases of different composition (2 phase region) to a single mixed state (1 phase region) at the critical temperature T_c, this adsorption profile would exhibit interesting universal behavior near T_c. Liu and Fisher[4] were the first to attempt to describe two different experimental systems using a single universal function. Following this seminal work, Carpenter et al.[5,6] determined a single universal model, called the P1 model, which could describe the ellipsometric measurements taken over a range of temperatures for four different critical binary liquid systems.

It is important to verify the P1 model using other experimental techniques because

the functional form for this (strong) critical adsorption is expected to be widely applicable in other systems[7]. Additionally, the P1 model forms the basis for models that describe more complicated critical binary systems. For example, Cho et al.[8] studied weak critical adsoprtion, where h_1 was sufficiently small such that saturation of the adsorption layer by one component of the critical binary mixture was incomplete. They successfully described ellipsometric data for a homologous series of mixtures using a model that reduced to the P1 model in the limit when $h_1 \to \infty$. In another study, Cho and Law[9] described data from systems where one component was strongly polar using a model based upon the P1 model.

Until recently work using other experimental techniques, such as neutron or X-ray reflectometry, has in general failed to validate either the P1 model, or universality for these systems. Brown et al.[10] describe a successful attempt to use the P1 model to describe data from neutron reflectometry measurements on the adsorption profile of a critical mixture of D_2O and 3-methylpyridine against a crystalline quartz substrate. Bowers et al[11] performed a similar experiment, and reported results consistent with the P1 model. There is, however, no ellipsometry data on these systems. Here we describe simultaneous analysis of data from two experimental techniques used to study a single critical liquid mixture system. We investigate the liquid-vapor interface of the non-polar critical mixture n-dodecane + tetrabromoethane (DT) . Ellipsometry data for this system was taken by Cho, Law, and Gray[12] and used to verify the P1 model. X-ray reflectometry data was taken by Marschand et al.[13] However, their analysis was inconsistent with the P1 model. The reason for the disagreement between X-ray and ellipsometric data was not understood at the time.

6.2 Theory

Fisher and de Gennes[3] hypothesized that in the case of a critical binary liquid mixture the decay profile could be modeled with a universal (system independent) scaling function defined in terms of the surface field h_1 and the dimensionless length z/ξ, where z is the

depth into the liquid. Sufficiently near T_c the correlation length is described by

$$\xi = \xi_0 t^{-\nu}, \tag{6.1}$$

where $t \equiv |T - T_c|/T_c$ is the reduced temperature and $\nu \simeq 0.632$[14] is a universal critical exponent. As $h_1 \to \infty$, corresponding to strong critical adsorption, this surface profile loses its dependence on h_1 and simplifies to

$$m_{\pm}(z) \equiv \phi(z) - \phi_c = M_{-} t^{\beta} P_{\pm}[(z + z_e)/\xi_{\pm}], \tag{6.2}$$

where $\phi(z)$ is the relative volume fraction of the component with the lower surface energy, ϕ_c is the bulk critical composition, M_{-} is a system dependent parameter, $\beta \simeq 0.328$[14] is the universal bulk critical exponent describing the coexistence curve, and $P(x)$ is a universal critical composition scaling function. The subscript + (-) refers to the one (two) phase region.

There are constraints on the form of $P(x)$. At the critical temperature ($t = 0$), $m(x)$ must remain finite and non-zero. Therefore, the factor t^{β} in Eq. (6.2) must be cancelled by the leading order term in $P(x)$. Specifically, $P(x)$ must possess the form[3]

$$P_{\pm}(x) \sim c_{\pm} x^{-\beta/\nu} \text{ as } x \to 0. \tag{6.3}$$

It is also necessary to prevent $P(x)$ from diverging at $z = 0$; this is the purpose for the extrapolation length z_e which appears in Eq. (6.2). In past ellipsometric work, z_e has been used to define where the profile is saturated by the component possessing the lowest surface energy via the condition that $m_{\pm}(0) = 1$.

For large x, the profile is expected to exhibit exponential decay[4]. In this case, we have

$$P_{\pm}(x) \sim P_{\pm}(\infty) + P_{\infty\pm} e^{-x}. \tag{6.4}$$

The constant $P_{\pm}(\infty)$ must be chosen such that Eq. (6.2) describe the bulk composition as $z \to \infty$. For the one phase region this requires that $m_{+}(z \to \infty) \to 0$, and therefore

$$P_{+}(z \to \infty) \equiv P_{+}(\infty) = 0. \tag{6.5}$$

In the two phase region, the coexistence phase diagram is described by $\phi = \phi_c + M_- t^\beta$, thus,

$$P_-(z \to \infty) \equiv P_-(\infty) = 1. \tag{6.6}$$

The constants $c_\pm$ and $P_{\infty\pm}$ that appear in Eqs. (6.3) and (6.4) will be universal because $P_\pm(x)$ is a universal function. An extensive review of previous experimental work investigating the functional form of $P(x)$ can be found in[10] and references therein.

6.3 P1 Model

In 1999 Carpenter, Cho, Smith and Law[5,6] found a universal scaling function (the P1 model) which successfully described the ellipsometric experimental data for four different critical mixtures both above and below T_c. What follows is a description of the P1 model.

Eqs. (6.3) and (6.4) provide only the leading order terms for $P(x)$. A viable model must provide a more complete description of both the exponential and power law decay regimes where a crossover between these two regimes must occur at some intermediate value of x. For small x, Diehl and Smock[15] suggested that these higher order terms should take the form

$$P_\pm(x) = c_\pm x^{-\beta/\nu} + c_{1\pm} x^{(1-\beta)/\nu} + c_{2\pm} x^{(2-\beta)/\nu} + c_{3\pm} x^{3-\beta/\nu} ..., \tag{6.7}$$

where the coefficients $c_{i\pm}$ all represent additional universal constants. For large x, Liu and Fisher[4] suggested the form

$$P_\pm(x) = P_\pm(\infty) + P_{\infty\pm} e^{-x} + P_{1\pm} e^{-2x} + P_{2\pm} e^{-3x} + ..., \tag{6.8}$$

where $P_{i\pm}$ represent additional universal constants. Carpenter et al. used modified versions of Eqs. (6.7) and (6.8)

$$\mathrm{P1}_\pm(x) = c_\pm x^{-\beta/\nu} + c_{1\pm} x^{(1-\beta)/\nu}, x < x_0 \tag{6.9}$$

$$\mathrm{P1}_\pm(x) = P_\pm(\infty) + P_{\infty\pm} e^{-x} + P_{1\pm} e^{-2x}, x \geq x_0 \tag{6.10}$$

where x_o is a crossover point between small and large x. The name P1 refers to the fact that $c_{1\pm}$ and $P_{1\pm}$ are chosen such that $P(x)$ and its first derivative are continuous at $x = x_0$.

Model	Phase	$x_{o\pm}$	$c_{\pm}$	$c_{1\pm}$	$P_{\infty\pm}$	$P_{1\pm}$	$10^4\sigma$
P1	1	1.15	$0.788^{+0.009}_{-0.015}$	-0.245	$0.963^{+0.117}_{-0.201}$	1.437	1.3756
	2	1.15	$1.117^{+0.013}_{-0.021}$	0.169	$0.572^{+0.357}_{-0.152}$	0.533	

Table 6.1: *Critical adsorption P1 scaling function*

The additional constraint that $m(z)$ is continuous at T_c, together with three experimental constraints, leaves the crossover point, x_0, as the only adjustable parameter. The values for $c_{\pm}$, $c_{1\pm,}$ $P_{\infty\pm}$, $P_{1\pm}$ and x_o which provided the best fit to the experimental ellipsometric data are given in Table 1. It should be noted that Carpenter et al. examined another model where more terms were kept, with additional constraints of continuity for the second and third derivitives at x_0. However, this more complex 'P3' model did not describe the experimental ellipsometric results any better than the simplier P1 model[6]. The four systems analyzed by Carpenter et al. all had components that were weakly polar. Eq. (6.2) is strictly applicable to simple non-polar systems. Therefore Cho, Law and Gray[12] studied the non-polar critical mixture n-dodecane + tetrabromoethane using ellipsometry. The ellipsometric data for this system was well described by the P1 model without requiring any further modification of the model.

Numerous attempts have been made in the past to confirm the universal surface scaling behavior for strong critical adsorption using other experimental techniques, such as neutron and X-ray reflectometry. Results have been mixed, as summarized in[10]. Many experiments not only disagreed with each other but also disagreed with theory. Two recent neutron experiments, however, provided excellent confirmation of theoretical expectations. Bowers et al.[11] confirmed both the power law behavior as well as the expected magnitude of the amplitude c_+ for the critical mixture hexane-d_{14} + perfluorohexane against an octadecyl-coated silicon substrate. Brown et al.[10] found good agreement between the P1 model and a neutron reflectometry experiment for 3-methylpyridine + D_2O against a crystalline quartz substrate. A disturbing negative result was reported in[13], where, although a novel X-

Substance	ε^a	$10^6\delta^b$	$10^8\beta^b$	M_-^c	$\xi_{o+}(nm)^c$	$T_c(^oC)$
n-dodecane (D)	2.019	1.48	0.0974			
1,1,2,2-tetrabromoethane (T)	2.680	4.36	9.04			
Critical mixture (at $\phi_D = 0.45$)	2.358	3.06	5.01	0.869	0.29	37.5

Table 6.2: *X-ray and optical parameters for the DT critical mixture*

ray inversion procedure provided a consistent description of X-ray reflectometry data for the liquid-vapor surface of the critical mixture DT, the profiles found from this inversion procedure could not explain ellipsometry data from the same mixture. The profiles also failed to clearly show the expected universal scaling behavior. The purpose of this paper is to reconcile this X-ray and ellipsometry data for the DT system with the P1 model.

6.4 Experimental Methods

Sample preparation and experimental methods for the DT system are discussed in[12] and[13]. What follows is a brief summary and some additional details. The sample for X-ray reflectometry was prepared by the primary author from n-dodecane (99% purity) and 1,1,2,2 tetrabromoethane (Fluka, 98 % purity). (The companies and purities of the chemicals, as stated in[13], were erroneously reversed). A mixture of relative volume fraction of 45% n-dodecane was prepared. Ref.[13] states that this composition is within 1% of the critical volume fraction. A more careful analysis of the lever rule[16] and data indicates that in fact this composition is within 0.3 % of the critical composition. The sample for ellipsometry was prepared in the same laboratory, under similar conditions[12]. Both samples gave the same ellipsometric results within error bars. Relevant optical and X-ray parameters for the DT critical mixture are listed in Table 2.

The X-ray measurements were performed at CNC-CAT at the Advanced Photon Source of Argonne National Laboratory in July of 2003. The sample was in a temperature controlled environment with a thermal stability of better than 1 mK/h, and thermal gradients of less

than 1 mK/cm[17]. The liquid sample was contained within a 7mm deep pyrex trough within a sealed environment. Surface vibrations were dampened by a 19 mm wide by 45 mm long pyrex table at a level 0.5mm below the top of the trough. For the DT critical mixture, the n-dodecane component is expected to completely saturate the liquid-vapor surface because this component possesses the lowest surface tension. This liquid-vapor surface was maintained at $\sim$ 0.5 mm above the edges of the trough by overfilling the trough. In this manner, grazing incidence X-ray measurements could be collected while avoiding the experimental complications associated with having a very long sample trough or with passing the X-ray beam through a liquid meniscus[10]. Data was collected at temperatures ranging from 1 to 30 ^oC above $T_c (\simeq 37.5^oC)$.

The earlier ellipsometry data[12] was collected in a similar temperature controlled environment. Prior to the X-ray experiment, we confirmed that ellipsometry results collected in the X-ray oven (but with the pyrex table removed) gave identical ellipsometric results to[12] within error bars.

6.5 Analysis

As we will see shortly X-ray reflectometry and ellipsometry provide complementary measures of the local composition $\phi(z)$ (Eq. (6.2)) where X-ray reflectometry is most sensitive to the short-range structure (immediately adjacent to the surface), whereas, ellipsometry is most sensitive to the long-range structure which plays a major role at temperatures close to T_c. It is therefore advantageous, especially for interfaces that possess both short- and long-range structure, to use *both* measurement techniques where a single unique $\phi(z)$ must be found which can describe both data sets. In the following, we first briefly describe what each of these two experimental techniques measure before proceeding on to determine the composition profile $\phi(z)$.

6.5.1 Ellipsometry

In ellipsometry, we measure the ellipticity $\overline{\rho} \equiv Im(r_p/r_s)$ at the Brewster angle where r_j is the complex reflection amplitude for polarization j. This measurement is composed of two contributions: an intrinsic contribution $\overline{\rho}_i$ determined by the variation in the local composition profile $\phi(z)$ and an additive capillary wave contribution $\overline{\rho}_c$[18]. For thin films ($\xi/\lambda_v \ll 1$), $\overline{\rho}_i$ is related to the optical dielectric profile $\varepsilon(z)$ at the surface via the Drude equation[19]

$$\overline{\rho}_i = \frac{\pi}{\lambda_v}\frac{\sqrt{\varepsilon_1+\varepsilon_2}}{\varepsilon_1-\varepsilon_2}\int_{-\infty}^{+\infty}\frac{(\varepsilon(z)-\varepsilon_1)(\varepsilon(z)-\varepsilon_2)}{\varepsilon(z)}dz. \tag{6.11}$$

Here $\lambda_v(= 632.8nm)$ is the vacuum wavelength of light used in the experiment while $\varepsilon(z)$ varies between it's value in the incident air ($\varepsilon_1 = \varepsilon(-\infty) = 1$) and reflecting liquid ($\varepsilon_2 = \varepsilon(+\infty)$) media (Table 2). For *thick films,* Eq. (6.11) is no longer valid and $\overline{\rho}_i$ must be determined by numerically solving Maxwell's equations. This is in general done by decomposing $\varepsilon(z)$ into dielectric slabs of thickness Δz_i at depth z_i. The electric field boundary conditions at each of the interfaces of the slab are matched in order to numerically solve Maxwell's equations[20]. For AB liquid mixtures the local dielectric contstant $\varepsilon(z)$ is related to the local composition $\phi(z)$, discussed in Secs. 1 and 2, via the two component Clausius-Mossotti equation[21]

$$f(\epsilon(z)) = \Omega[\phi(z)f(\epsilon_{\mathrm{D}}) + (1-\phi(z))\, f(\epsilon_{\mathrm{T}})], \tag{6.12}$$

$$f(X) \equiv \frac{X-1}{X+2}, \tag{6.13}$$

where the volume change on mixing

$$\Omega = \frac{V_D+V_T}{V_{D+T}} \tag{6.14}$$

is assumed to be 1. Here subscript D (T) refers to the n-dodecane (tetrabromoethane) component. The sensitivity of ellipsometry to strong critical adsorption arises because $\phi(z)$ and, therefore, $\overline{\rho}_i$ is a strong function of the reduced temperature $t = \mid T_c - T \mid /T_c$. The additive capillary wave component is reasonably temperature independent[23] and does not provide any information about strong critical adsorption.

6.5.2 X-ray Reflectometry

X-ray reflectometry measures the fraction R of the incident beam that is reflected from a sample at a wavevector Q

$$Q = \frac{4\pi \sin\theta}{\lambda_X} \approx \frac{4\pi\theta}{\lambda_X}, \tag{6.15}$$

where θ is the incident grazing angle, $\lambda_X (= 0.113nm)$ is the X-ray wavelength while the approximate form is valid for all practical purposes because θ is small. In the first Born approximation, valid at large scattering vectors away from the critical scattering vector Q_c, the intrinsic contribution to the X-ray reflectivity from the variation in the local composition is[24]

$$R_i(Q) = R_F \left| \frac{1}{\rho(\infty)} \int \frac{d\rho(z)}{dz} e^{iQz} dz \right|^2 \tag{6.16}$$

where $\rho(z)$ is the local electron density with bulk density $\rho(\infty)$ and $R_F \sim Q^{-4}$ is the Fresnel reflectivity for an infinitely sharp and unstructured interface. In the following we therefore plot the quantity $R(Q)Q^4$ as a function of Q, in order to compensate for the strong Q dependence of R_F. Eq. (6.16) is not valid near the critical scattering vector $Q_c \equiv 4\pi\theta_c/\lambda_X$, below which the incident beam is totally reflected.

In analogy to ellipsometry, X-ray reflectometry can alternatively be analysed by treating the profile as a series of thin slabs of uniform composition, and numerically solving Maxwell's equations. This numerical solution is valid for all scattering vectors Q, unlike Eq. (6.16). The local refractive index at depth z_j is given by

$$n(z_j) \approx 1 - \phi(z_j)\left(\delta_\mathrm{D} - \mathrm{i}\beta_\mathrm{D}\right) - \left(1 - \phi(z_j)\right)\left(\delta_\mathrm{T} - \mathrm{i}\beta_\mathrm{T}\right) \tag{6.17}$$

where

$$\delta_s = \frac{\lambda_X^2}{2\pi}(SLD)_s, \beta_s = \frac{\lambda_X}{4\pi}\mu_s, \tag{6.18}$$

and $(SLD)_s$ and μ_s are, respectively, the X-ray scattering length density and absorption coefficient for component s (Table 2). Maxwell's equations can be solved either via a series of matrix calculations[20] or by using an iterative technique suggested by Parratt[24,25]. In this

work we used the Parratt method for computational efficiency. In this method the ratio of incident and reflected radiation in each layer, $X_j \equiv R_j/T_j$, is calculated as a function of this same ratio in the layer below:

$$X_j \equiv \frac{R_j}{T_j} = e^{-2ik_{z,j}z_j} \frac{r_{j,j+1} + X_{j+1}e^{2ik_{z,j+1}z_j}}{1 + r_{j,j+1}X_{j+1}e^{2ik_{z,j+1}z_j}}, \tag{6.19}$$

where

$$r_{j,j+1} \equiv \frac{k_{z,j} - k_{z,j+1}}{k_{z,j} + k_{z,j+1}} \tag{6.20}$$

is the Fresnel reflection coefficient for perpendicular polarization. Note that for X-rays, one can ignore the difference between the s and p polarization components (which were important for ellipsometry) because, to an excellent approximation, these reflectivities are identical because $n(z_j)$ for X-rays is so close to 1 [24]. The starting point for the above iteration is the last (deepest) interface at z_N, where $X_{N+1} = R_{N+1} = 0$.

Eqs. (6.19) and (6.20) assume each interface is perfectly smooth, transitioning from one medium to another over an infinitesimal length scale. In reality an interface j will have some finite thickness σ_j. We account for roughness by replacing $r_{j,j+1}$ in Eq. (6.19) with

$$\tilde{r}_{j,j+1} = r_{j,j+1} \exp(-2k_{z,j}^2 \sigma_j^2). \tag{6.21}$$

where $\exp(-2k_{z,j}^2\sigma_j^2)$ is the Beckmann-Spizzichino factor [26]. Other factors, such as the Nevot-Croce factor $\exp(-2k_{z,j}k_{z,j+1}\sigma_j^2)$ [28], may be used depending on the nature of the rough surface. Tolan [24] discusses this in more detail. In our case we need especially consider the roughness of the liquid-vapor interface, which will be due largely to Capillary wave contributions. $\sigma_{0,1}$ in table 3 refers to the roughness of the liquid vapor interface. We do not include roughness elsewhere in our model, as explained below.

6.5.3 Determination of $\phi(z)$

As mentioned earlier, the current authors have found contradictory results as to whether or not the ellipsometric P1 model could or could not describe X-ray/neutron reflectometry

$\Delta T(^{\circ}C)$	l_2 (nm)	ϕ_2	l_3 (nm)	ϕ_3	$\sigma_{0,1}$ (nm)	χ^2
1	3.37	0.788 (fixed)	0.78	0.686	0.65	15.8
2	2.72	0.788 (fixed)	0.85	0.693	0.62	17.0
3	3.03	0.788 (fixed)	0.68	0.674	0.71	8.5
5	3.13	0.788 (fixed)	0.85	0.674	0.70	33.5
15	2.63	0.788 (fixed)	0.69	0.611	0.63	35.8
uniform	3.20	0.788	0.80	0.686	0.65	N/A

Table 6.3: *Fitting parameters*

data for strong critical adsorption. In a neutron reflectometry experiment[10], for a critical mixture of D_2O + 3-methyl-pyridine against a crystalline quartz substrate, the primary authors found that the experimental results were consistent with the P1 model for strong critical adsorption, at least for temperatures close to T_c. However, this agreement required that the quartz substrate only be partially saturated by D_2O with a surface volume fraction of 0.86. The partial saturation was attributed to competing hydrogen bonding of the two liquid components for the quartz surface. For temperatures far from T_c ($\Delta T \gtrsim 5^oC$), the neutron results exhibited deviations from the P1 model, which perhaps were an indication of a cross-over to mean field behavior.

This excellent neutron reflectometry agreement with the P1 model should be contrasted with the X-ray reflectometry disagreement with the P1 model[13] found at the liquid-vapor surface of the DT mixture. In this X-ray paper an inversion procedure suggested by Sanyal et al.[27] provided composition profiles that provided an excellent description of the X-ray data. However, these composition profiles failed to describe the ellipsometric data from the same interface. These two studies[10,13] provide a clearer picture of what one must do in order to resolve this discrepancy between X-ray and ellipsometry data for the DT mixture at the liquid-vapor surface. X-ray and neutron reflectometry are most sensitive to the near surface structure which, in wavevector space, occurs at large Q far from the critical wavevector Q_c. This near surface structure is expected to be fairly *temperature independent.* The far surface

structure, that occurs near Q_c, is less well resolved by X-ray and neutron reflectometry. In fact, the value of Q_c provides a practical upper limit to the length scale of features that neutron or X-ray reflectometry can distinguish within a surface profile. This limit is due to the very low resolution for features larger than $l_{\max} = 2\pi/Q_c$. For the critical mixture studied here $Q_c = 0.277\text{nm}^{-1}$ and $l_{\max} \simeq 23nm$, hence, from the temperature dependence of the correlation length (Eq. (6.1)) X-ray reflectivity curves measured at temperature differences $\Delta T = T - T_c \leq 1^0C$ will be practically indistinguishable from each other (which is what was found experimentally). In contrast to X-ray and neutron reflectometry, single wavelength ellipsometry is best at resolving large scale temperature dependent features (far from the interface) via the strong temperature dependence of $\overline{\rho}$ near T_c. The small scale (temperature independent) features, close to the surface, just provide an additive constant background to the ellipticity $\overline{\rho}$.

In order to describe both the X-ray and ellipsometry data for the DT system the composition profile should have the following properties: (i) close to the surface it should look like the X-ray profile deduced in[13] while (ii) far from the surface it should cross-over to the P1 model, in order to reproduce the temperature dependent ellipsometric data close to T_c. Fig. 1 shows the simplest model that we have found that can quantitatively describe both the X-ray and ellipsometric data and is consistent with these short and long-range composition profile requirements. A pure dodecane monolayer at the surface ($\phi_1 = 1$, $l_1 = 0.7$nm) transitions to the P1 model over a distance of ~ 4.5 nm (about 6 monolayers) where two intermediate layers have been inserted between the surface (at $z = 0$) and the P1 model (at $z \gtrsim 4.5nm$). The first intermediate layer has a thickness of $l_2 \sim 3.0\pm\ 0.2nm$ and composition $\phi_2 \simeq 0.79$ while the second intermediate layer has a thickness $l_3 \sim 0.8\pm\ 0.1nm$ and composition $\phi_3 \simeq 0.69$. The extrapolation length z_e in Eq.(6.2) was chosen such the P1 model begins to decay from a composition of $\phi_4(z = l_1 + l_2 + l_3) = \phi_3$. The sudden drop from a $\phi_1 = 1$ (at the surface) to a $\phi_2 \simeq 0.79$ (in the first intermediate layer) agrees reasonably well with the short-range structure found via the X-ray inversion process in[13],

as indicated by the inset in Fig. 1 for $\Delta T = 1^oC$. The long-range structure in Fig. 1 is very similar to the P1 model. The dotted lines show the variation in n-dodecane composition as a function of depth z for the pure P1 model decaying from the surface dodecane monolayer at $\Delta T = 0.01, 1, 2, 3, 5$ and 15^oC, while the solid lines represent the actual large scale structure selected in the model. The pure P1 model has been offset by a distance of $l_2 + l_3$ to demonstrate the match with our surface layering model. The solid lines agree well with the dotted lines for $z > l_1 + l_2 + l_3$, with the exception of the $\Delta T = 15^oC$ data. Note that the profile plots for $\Delta T = 0.01^oC$ in Fig. 1 are for model comparison only. We do not have x-ray data for that temperature. In obtaining our best fit results we fixed $l_1 = 0.7$nm (about 1 monolayer) for the adsorbed dodecane layer and varied the thicknesses l_2 and l_3, as well as, the compositions ϕ_2 and ϕ_3 of the two intermediate layers. For most fits we found $\phi_2 \approx 0.788$; hence, to limit the parameter space to be searched we fixed ϕ_2 at this value. The best fit values for l_2, l_3, ϕ_3 and $\sigma_{0,1}$ were obtained by minimizing

$$\chi^2 = \sum_{i=1}^{N} \frac{\left[R_{\text{model}}(Q_i) - R_i\right]^2}{{w_i}^2}, \tag{6.22}$$

where R_i represents the experimental X-ray reflectivity data at wavevector Q_i while $R_{\text{model}}(Q_i)$ corresponds to the X-ray reflectivity for our model. In fitting the data one must carefully select the weight factor w_i because the reflectivity decreases by several orders of magnitude for increasing Q above Q_c. As in[10] we found that

$$w_i \ = R(Q_j)\sqrt{1 - Log_{10}(R(Q_j))} \tag{6.23}$$

provided a satisfactory weight factor over the entire Q range.

The best fit values obtained for l_2, l_3, ϕ_3 and $\sigma_{0,1}$ are listed in Table 3 where this model (solid lines) is compared with the X-ray data (symbols) in Fig. 2. We expect that the short-range structure encompassed by the parameters l_2, l_3, ϕ_3 and $\sigma_{0,1}$ should be fairly temperature independent, at least for temperatures close to T_c, where $\sigma_{0,1}$ should be similar in magnitude to the value found at the liquid-vapor surface of long n-alkane liquids[29]. This is indeed found to be approximately true from the results in Table 3. Therefore, we have

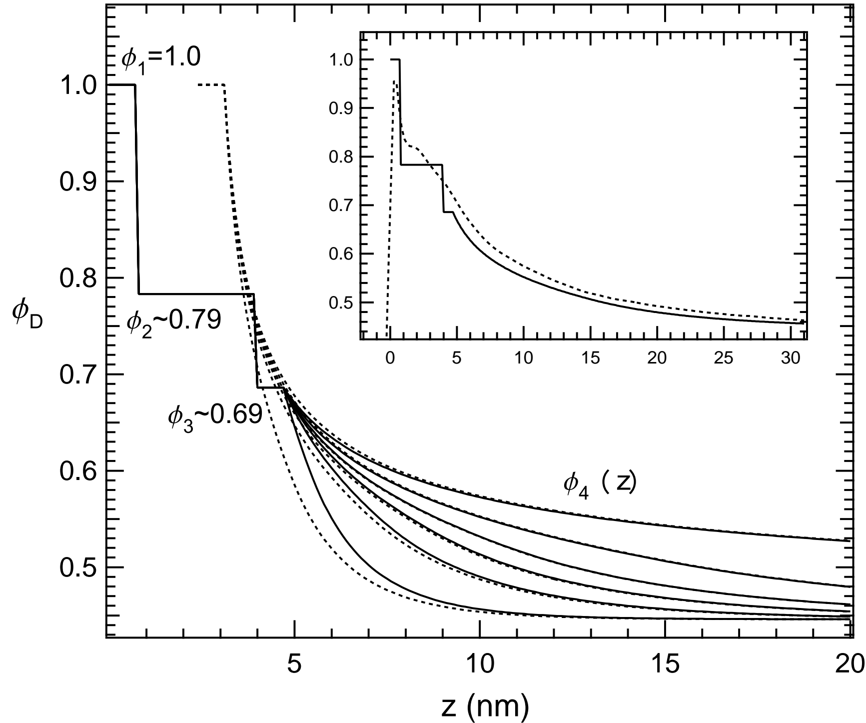

Figure 6.1: *Plot of the n-dodecane local volume fraction $\phi(z)$ (solid lines) as a function of the depth z away from the liquid-vapor interface at $z = 0$ for temperature differences of $\Delta T = 0.01, 1, 2, 3, 5$ and 15^oC from T_c. The model consists of short-range (temperature independent structure) consisting of three layers of thickness l_1, l_2 and l_3 with compositions ϕ_1, ϕ_2 and ϕ_3 which joins onto a long-range P1 model at $z = l_1 + l_2 + l_3$. The long-range structure is very similar to a displaced pure P1 model (dotted lines), at least for $\Delta T \lesssim 5^oC$. Inset: comparison of this model with the X-ray model found via inversion in[13] for $\Delta T = 1^oC$.*

also considered a model where l_2, l_3, ϕ_3 and $\sigma_{0,1}$ are fixed at the values given in the last line of Table 3. This uniform model is also compared with the X-ray data in Fig. 2 (dotted lines). With the exception of the $\Delta T = 15^oC$, the uniform model provides an excellent description of the X-ray data. The uniform model also provides a reasonable description of the ellipsometric data $\overline{\rho}$ as a function of the reduced temperature t (Fig. 3) where the dotted line is the pure P1 model while the solid line is the uniform model. As mentioned above, we explicitely include roughness at the liquid-vapor interface in the parameter $\sigma_{0,1}$. We do not, however, include rougness below either the first or second intermediate layers.

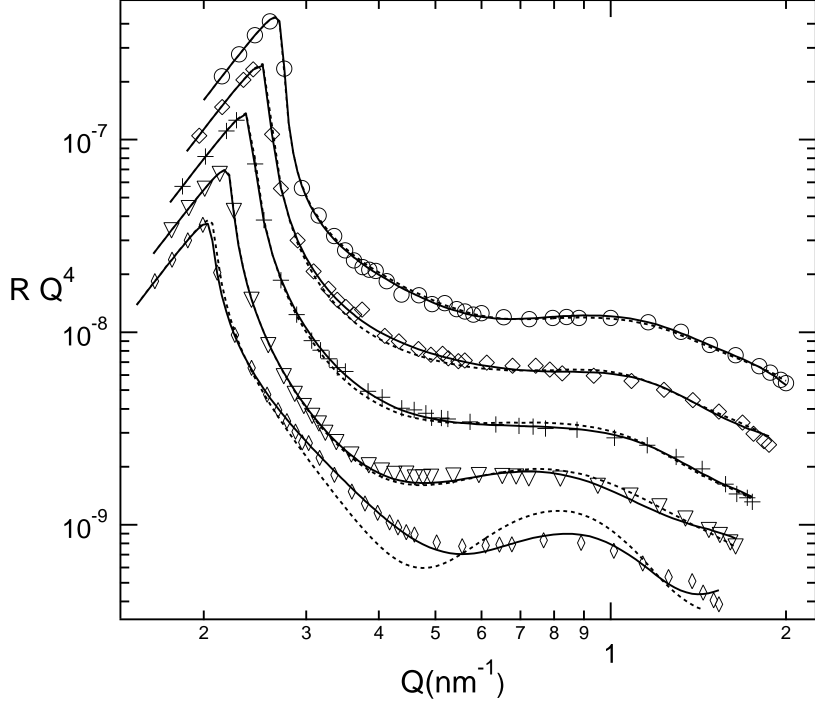

Figure 6.2: *X-ray reflectometry data taken at $\Delta T = 1$ (circles), 2 (diamonds), 3 (pluses), 5 (triangles), and 15ºC (thin diamonds) for the critical mixture n-dodecane and 1,1,2,2-tetrabromoethane at the liquid-vapor interface. The solid lines represent fits to the data, as described in the text, where the best fit values for l_2, l_3, ϕ_3 and $\sigma_{0,1}$ are listed in Table 3. The experimental data is also compared with a uniform model (dotted lines) where these parameters are fixed at the values given in the last line of Table 3. For clarity each curve has been displaced vertically by a factor of 0.07.*

Doing so would add two additional roughness parameters $\sigma_{1,2}$ and $\sigma_{2,3}$ to our model. In an attempt to include these parameters in our model, we found that various combinations of $\sigma_{0,1}$, $\sigma_{1,2}$, and $\sigma_{2,3}$, wherein $\sigma_{1,2}$ and $\sigma_{2,3}$ ranged from 0 to 0.3 nm, and $\sigma_{0,1}$ ranged from 0 to 0.15 nm smaller than the values in table 3 produced roughly equivalent fits to our x-ray data, and is not distinguishable in our ellipsometry simulations. Inclusion of these additional parameters would complicate our model without adding additional insight into the universal critical behavior we are interested in.

Our layering scheme does overstate the ellipsometric background term by 1.2×10^{-3} as

compared to the data taken by Cho, Law and Gray[12]. A more sophisticated model than the one we present here may be able to account for much of this. However, this shift is not much larger than typical differences we see between ellipsometric measurements on different samples of the same binary liquid system. For example, the ellipsometric data we took to compare our results to those of Cho, Law and Gray[12] resulted in a background term 0.39×10^{-3} higher than theirs.

The neutron experiment in[10] suggests that only ellipsometric and X-ray data at $\Delta T \lesssim 5^oC$ can be expected to be well explained by the P1 model, which incorporates Ising critical exponents where critical fluctuations play a dominant role. At $\Delta T \gtrsim 5^oC$ a cross-over to mean field behavior might be expected[30]; this is probably the explanation for the difference between the uniform model and experimental X-ray data at $\Delta T = 15^oC$ in Fig. 2.

6.6 Conclusion

In this paper we have found a model that successfully describes both the Q and temperature dependence of the X-ray reflectivity data (Fig. 2), as well as the temperature dependence of the ellipsometric data (Fig. 3) for strong critical adsorption of n-dodecane at the liquid-vapor surface of the critical mixture n-dodecane + 1,1,2,2-tetrabromoethane. This model consisted of large depth z structure described by the P1 model, used in ellipsometry, where short-range temperature independent z structure was added to this model (Fig. 1). Good agreement is found between theory and experiment at least for temperatures within 5^oC of T_c. At larger temperatures, further from T_c, this model does not describe experimental data as well – a fact that we attribute to a cross-over to mean field behavior. This study illustrates the utility of combining X-ray/neutron reflectometry (to deduce short-range interfacial structure) with ellipsometry (to study long-range interfacial structure). Such a combination of experimental techniques will be important for ascertaining the interfacial behavior of complex surfaces which possess features on many different length scales.

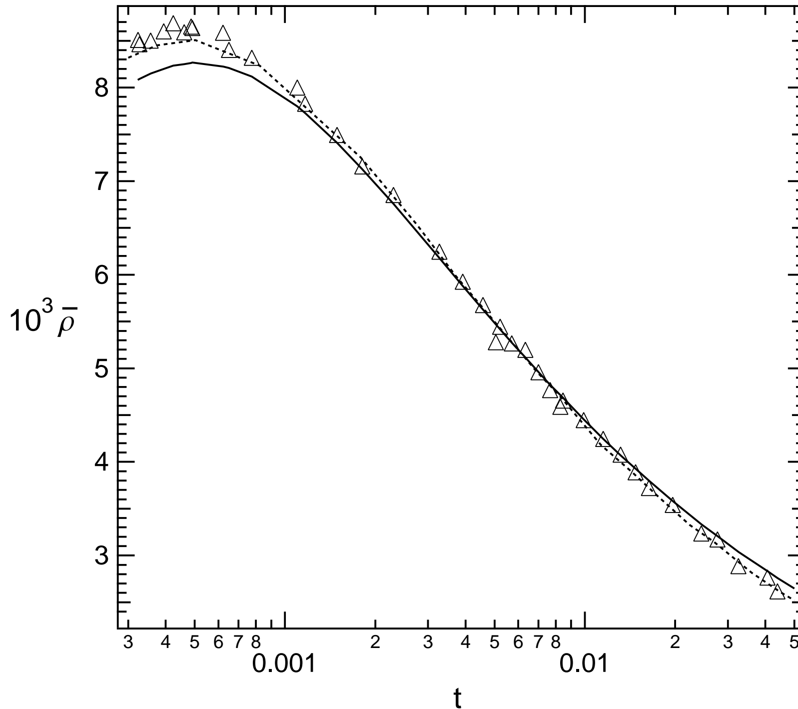

Figure 6.3: *Ellipsometric data (symbols) collected from the liquid-vapor surface of the critical mixture n-dodecane + 1,1,2,2-tetrabromoethane as a function of the reduced temperature t. Pure P1 model (dotted line). Uniform P1 model (solid line) where the values for l_2, l_3, ϕ_3 and $\sigma_{0,1}$ are listed in Table 3.*

6.7 Acknowledgements

Two of the authors (BML and LL) acknowledge support for this work from the US Department of Energy through Grant No. DE-FG02-02ER46020. BML also acknowledges partial support through National Science Foundation grant number DMR-0603144. The Advanced Photon Source at Argonne National Laboratory is supported by DOE grant W-31-109-Eng-38.

Bibliography

[1] M. E. Fisher and H. Au-Yang, Physica **101A**, 255 (1980); H. Au-Yang and M. E. Fisher, Phys. Rev. B **21**, 3956 (1980).

[2] U. Ritschel and P. Czerner, Phys. Rev. Lett. **77**, 3645 (1996).

[3] M. E. Fisher and P.-G. de Gennes, C. R. Acad. Sci. Paris B **287**, 207 (1978).

[4] A. J. Liu and M. E. Fisher, Phys. Rev. A **40**, 7202 (1989).

[5] J. H. Carpenter, B. M. Law, and D. S. P. Smith, Phys. Rev. E **59**, 5655 (1999).

[6] J. H. Carpenter, J.-H. J. Cho and B. M. Law, Phys. Rev. E **61**, 532 (2000).

[7] H. W. Diehl, Int. J. Mod. Phys. B **11**, 3503 (1997).

[8] J.-H. J. Cho and B. M. Law, Phys. Rev. Lett, ; Phys. Rev. E, **65**, 0110601, (2001).

[9] J.-H. J. Cho and B. M. Law, Phys. Rev. Lett. **89**, 146101 (2002); Phys. Rev. E **67**, 031605 (2003).

[10] M. D Brown, B. M. Law, S. Satija, W. A. Hamilton, E. Watkins, J.-H. J. Cho and J. Majewski, J. Chem. Phys, accepted for publication.

[11] J. Bowers, A. Zarbakhsh, H. K. Christenson, I. A. McLure, J. R. P. Webster and R. Steitz, Phys. Rev. E **72**, 041606 (2005).

[12] J.-H. J. Cho, B. M. Law and K. Gray, J. Chem. Phys., **116**, 3058, (2002).

[13] L. W. Marschand, M. Brown, L. B. Lurio, B. M. Law, S. Uran, I. Kuzmenko and T. Gog, Phys. Rev. E **72**, 011509 (2005).

[14] M. E. Fisher and J. -H. Chen, J. Phys. (Paris) **46**, 1645 (1985).

[15] H. W. Diehl and M. Smock, Phys. Rev. B, **47**, 5841, (1993); **48**, 6470(E) (1993).

[16] L. D. Landau and E. M. Lifshitz, *Statistical Physics* (Pergamon, Oxford, 1980), 3rd ed. Part 1.

[17] M. Brown, S. Uran, B. Law, L. Marschand, L. Lurio, I. Kuzmenko and T. Gog, Rev. Sci. Instrum. **75**, 2536 (2004).

[18] A. M. Marvin and F. Toigo, Phys. Rev. A **26**, 2927 (1982).

[19] P. K. L. Drude, *The Theory of Optics* (Dover, New York, 1959), p. 292.

[20] M. Born and E. Wolf, *Principle of Optics* (Pergamon, Oxford, 1980), Sec. 1.6.

[21] R. F. Kayser, Phys. Rev. B **34**, 3254 (1986).

[22] D. Beaglehole, Physica B **100**, 163 (1980).

[23] D. S. Smith and B. M. Law, Phys. Rev. E **54**, 2727, (1996).

[24] M. Tolan, *X-ray scattering from Soft-Matter Thin Films*, edited by G. Höhler (Springer-Verlag, New York, 1999).

[25] L. G. Parratt, Phys. Rev., **95**, 359, (1954).

[26] P. Beckmann and A. Spizzichino, *The Scattering of Electromagnetic Waves From Rough Surfaces* (Pergamon, New York, 1963).

[27] M. K. Sanyal, S. Hazra, J. K. Basu, A. Datta, *Phys. Rev. B* **58**, R4258 (1998).

[28] L. Nevot and P. Croce, Revue de Physique applique'e, **15**, 761, (1980).

[29] B. M. Ocko, X. Z. Wu, E. B. Sirota, S. K. Sinha, and M. Deutsch, Phys. Rev. Lett. **72**, 242 (1994).

[30] J. K. Whitmer, S. B. Kiselev and B. M. Law, J. Chem. Phys. **123**, 204720 (2005).

Chapter 7

Conclusion

This work has focused on verifying the scaling theory of Fisher and de Gennes[1] for strong adsorption near the critical point for the demixing phase transition of binary liquid mixtures. In particular we have concentrated on verifying that a model used by Carpenter et al.[2] and Cho et al.[3] to describe ellipsometry data could be used to describe data collected with x-ray and neutron reflectometry from critical mixtures in the mixed state, near the critical temperature. Previous attempts to verify universal critical scaling in these systems with techniques other than ellipsometry have been unsuccessful, with the sole exception of a study by Bowers et al.[4] Using the universal scaling function suggested by Carpenter et al. we succeeded in describing data collected by neutron and x-ray reflectometry once we allowed for system dependent, non critical behavior at the interface.

We introduced Fisher and de Gennes' model for critical adsorption in the context of Landau's phenomenological theory. We showed how the presence of a uniform ordering field would lead to a non zero order parameter in the paramagnetic region of an Ising magnetic phase diagram, which is analogous to the mixed region for our system. We demonstrated that the magnitude of the ordering parameter would scale with a unitless function of h/t^{Δ}. We then extrapolated that given an ordering field with a one dimensional spatial dependence the scaling function would also be a function of z/ξ, as presented in the theory of Fisher and de Gennes[1] . We also noted that for large h, $G_{\pm}(h/t^{\Delta}, z/\xi) \rightarrow P_{\pm}(z/\xi)$. Thus the order parameter, which in our case is the difference in composition at depth z from the critical

composition, should be given by

$$m_{\pm}(z,t) \equiv v - v_c = \mathrm{M_t}^{\beta} P_{\pm}\left(\frac{(z - z_{\mathrm{ex}})}{\xi}\right), \tag{7.1}$$

where z_{ex} is chosen to give the appropriate value for $z = 0$.

In chapter 5 we presented more detail of the theory of Fisher and de Gennes, who showed that $P_{\pm}(x) \cong c_{\pm}x^{-\beta/\nu}$ for small x, and $P_{\pm}(x) \cong P_{\pm}(\infty) + P_{\infty\pm}e^{-x}$ for large x. We also overviewed the work that was done leading up to the development of the P1 model which was used successfully to describe ellipsometry data for various critical binary liquid systems. This model provides for power law behavior for small x, exponential decay for large x, and a simple cross over at some point x_0:

$$P_{\pm}(x) = c_{\pm}x^{-\beta/\nu} + c_{1\pm}x^{(1-\beta)/\nu}, x < x_0, \tag{7.2}$$

$$P_{\pm}(x) = P_{\pm}(\infty) + P_{\infty\pm}e^{-x} + P_{1\pm}e^{-2x}, x \geq x_0.$$

Other than the need to account for a background shift in ellipsometry, the only variable parameter in Carpenter's analysis was x_0. Values for x_0, the various exponents, and the coefficients for the mixed regime are given in chapter 5.

In chapter 5 we described the data and analysis of a neutron reflectometry study done on a critical mixture of deuterated water + beta picoline against a quartz substrate. This was the first successful attempt to verify the Carpenter P1 model with a technique other than ellipsometry, and to our knowledge the second successful attempt to show universality in critical adsorption with a technique other than ellipsometry. Our result is also important in that we were able to distinguish between reflectivity curves as close as 0.08 and 0.25 degrees from the critical temperature. This was possible because of the low neutron contrast between the substrate and the bulk mixture. Another important finding of this experiment was what appeared to be incomplete saturation of the adsorption layer with a profile that none the less seems to be better described with a model for strong critical adsorption than with a model used to describe ellipsometry data for weak critical adsorption in Cho and Law[5]. This led us to suggest a new definition for strong critical adsorption: the case where the

surface field becomes sufficiently large that the degree of saturation of the surface layer looses dependence on the surface field. This allowed for the possibility that items other than relative surface free energies could determine the precise composition of the adsorption layer.

The data analyzed in chapter 6 was originally taken in the experiment discussed in chapter 4. The initial analysis done in chapter 4 was unsuccessful at producing a mathematical model or demonstrating universality. Instead of a mathematical model, the data was used to directly calculate profiles that were consistent with the reflectometry curves. This was done using an iterative approach suggested by Sanyal et al.[6] While the results did not conform to our expectations, and were in a form ill suited to use in simulating ellipsometry to compare with the ellipsometry data by Cho et al.[3] on the same system, the shape of the profiles did suggest allowing for layering against the interface, which might then cross over to critical scaling behavior at some point. Our results in chapter 5 contributed to our ultimate success in developing a model to describe the x-ray data by suggesting allowing for system dependent, non critical behavior at the interface. In revisiting the x-ray data in chapter 6, we found a mathematical model which combined surface layering with the Carpenter P1 model. This included a single monolayer of dodecane, an intermediate layer 4 to 5 monolayers thick at a relative composition of ~ 0.80 dodecane, and a final monolayer of composition ~ 0.69 transitioning to the P1 decay profile. This surface layering didn't vary in any systematic way with temperature for measurements within 5^0C of the critical temperature. The results were in excellent agreement with the x-ray data taken within 5^0C of T_c. The fits clearly began to break down within 15 degrees of T_c, which one might expect as the total expected length scale of the decay profile becomes comparable to that of the layering. We were also able to use the mathematical model to simulate ellipsometry measurements, which we could then compare to data taken by Cho et al[3]. Our simulation was in reasonable agreement with the experimental ellipsometry data. A better model of the transition region may improve the agreement.

Our study of critical binary liquid systems has focused on system independent behavior. This is also true of much of the work that has proceeded ours. The expected universal nature of the behavior being investigated allows experimentalists a wide array of choices in conducting an experiment. We were able to choose mixtures that suited the needs of specific experimental design considerations. In the experiment discussed in chapter 5 our mixture was chosen based on its low neutron contrast with the quartz substrate, the high contrast between components, a critical temperature which made the mixture convenient to work with, and relatively low vapor pressures of the components in the desired temperature range. The mixture tetrabromoethane + dodecane was likewise chosen for experimental convenience. The analysis of ellipsometry data done in[2] and[3] did not consider any system dependent values other than M_{-} and ξ_0 and a non critical background shift for the ellipsometry data. Ironically it may well be that the very insensitivity of ellipsometry to the nature of non critical aspects of surface structure (producing a fairly constant offset) which contributed to the success of analyzing ellipsometry data. We have seen a good deal of sensitivity to system dependent surface structure for x-ray and neutron reflectometry. Only by allowing for such non critical contributions were we able to succeed in describing our data. We believe that Bowers et al.[4] did so likewise, perhaps without realizing it. They did a neutron reflectometry study of a liquid mixture against a solid substrate. In their analysis they allowed z_{ex} to vary as a fitting parameter. As the effect of the extrapolation length is to determine the cutoff value of the decay profile at $z = 0$, the effect is identical to what we did in varying the composition of the surface adsorption layer in chapter 5.

The need to account for system dependent aspects of a given mixture leads to two important considerations. First, the failure of most previous work to verify universality, as well as differing results for various critical parameter values may well be due to system dependent behavior that was not accounted for, although insufficient thermal stability likely also played a role. Second, one must also consider that certain physical behaviors may even vary between samples of the same type of system. An example which does not affect

our analysis is that T_c will typically vary somewhat between samples of the same system. A more pertinent example is that the background contribution to ellipsometry data also tends to vary somewhat between samples. Given the nature of monochromatic ellipsometry, distinguishing the precise structure which contributes to this background is not possible. The low temperature dependence of the background fortunately made this unnecessary for analyzing the ellipsometry data as well. Structural differences in surface layers between samples can have a much more dramatic effect in reflectometry experiments.

The understanding of scaling in critical adsorption arising from analysis of ellipsometry by Carpenter et al.[2] opened a door to other research, leading to successful explanations of ellipsometry data gathered in weak critical adsorption systems[5] and systems involving orientational order[7] . As the P1 model has now been verified, and better understood with x-ray and neutron reflectometry, these techniques are now also available to investigate more complicated types of critical adsorption in binary mixtures. We have also seen the need to account for certain non critical, system dependent behavior in any such experiments. In this light data from previous reflectometry studies of critical adsorption systems should perhaps be revisited. One of particular interest is that done by Jetsin et al.,[8], which may in fact be more appropriately considered as a case of weak critical adsorption.

The layering in our model was particularly interesting, but understanding is somewhat hampered by the non systematic variations of layer thickness, particularly of the thicker intermediate layer. In this particular experiment the sample had to be disturbed between each measurement in order to replace damaged sample at the surface and to keep the height of the liquid above the trough height. As a result sample height, and likely other parameters were varied between measurements in a fairly non systematic way. We believe that this could account for the non systematic variations of some of the parameters describing the layering. This layering could be investigated under conditions which do not require such disruptions of the sample for the tetrabromoethane + dodecane critical systems, and perhaps other systems with a liquid vapor interface as well.

Bibliography

[1] M. E. Fisher and P. G. de Gennes, C.R. Acad. Sci. Paris B, **287**, 207, (1978).

[2] J. H. Carpenter, J. H. J. Cho and B. M. Law, Phys. Rev. E, **61**, 532, (2000).

[3] J. J. Cho, B. M. Law and K. Grey, J. Chem. Phys., **116**, 3058, (2002).

[4] J. Bowers, et al., Phys. Rev. E, **72**, 041606, (2005).

[5] J. J. Cho and B. M. Law, Phys. Rev. E, **65**, 0110601, (2001).

[6] M. K. Sanyal, S. Hazra, J. K. Basu and A. Datta, Phys. Rev. B, **58**, R4258, (1998).

[7] J. J. Cho and B. M. Law, Phys. Rev. E, **67**, 031605, (2003).

[8] J. Jestin, L.-T. Lee, M. Privat and G. Zalczer, Eur. Phys. J. B **24**, 541 (2001).